

University of Kentucky

UKnowledge

Theses and Dissertations--Physics and
Astronomy

Physics and Astronomy

2023

The Radial Quenching Progression of Nearby Galaxies

Chenyu Zhao

University of Kentucky, czh276@uky.edu

Author ORCID Identifier:

<https://orcid.org/0009-0000-8710-1696>

Digital Object Identifier: <https://doi.org/10.13023/etd.2023.335>

[Right click to open a feedback form in a new tab to let us know how this document benefits you.](#)

Recommended Citation

Zhao, Chenyu, "The Radial Quenching Progression of Nearby Galaxies" (2023). *Theses and Dissertations--Physics and Astronomy*. 114.

https://uknowledge.uky.edu/physastron_etds/114

This Doctoral Dissertation is brought to you for free and open access by the Physics and Astronomy at UKnowledge. It has been accepted for inclusion in Theses and Dissertations--Physics and Astronomy by an authorized administrator of UKnowledge. For more information, please contact UKnowledge@lsv.uky.edu.

STUDENT AGREEMENT:

I represent that my thesis or dissertation and abstract are my original work. Proper attribution has been given to all outside sources. I understand that I am solely responsible for obtaining any needed copyright permissions. I have obtained needed written permission statement(s) from the owner(s) of each third-party copyrighted matter to be included in my work, allowing electronic distribution (if such use is not permitted by the fair use doctrine) which will be submitted to UKnowledge as Additional File.

I hereby grant to The University of Kentucky and its agents the irrevocable, non-exclusive, and royalty-free license to archive and make accessible my work in whole or in part in all forms of media, now or hereafter known. I agree that the document mentioned above may be made available immediately for worldwide access unless an embargo applies.

I retain all other ownership rights to the copyright of my work. I also retain the right to use in future works (such as articles or books) all or part of my work. I understand that I am free to register the copyright to my work.

REVIEW, APPROVAL AND ACCEPTANCE

The document mentioned above has been reviewed and accepted by the student's advisor, on behalf of the advisory committee, and by the Director of Graduate Studies (DGS), on behalf of the program; we verify that this is the final, approved version of the student's thesis including all changes required by the advisory committee. The undersigned agree to abide by the statements above.

Chenyu Zhao, Student

Dr. Renbin Yan, Major Professor

Dr. Christopher Crawford, Director of Graduate Studies

The Radial Quenching Progression of Nearby Galaxies

DISSERTATION

A dissertation submitted in partial
fulfillment of the requirements for
the degree of Doctor of Philosophy
in the College of Arts and Sciences
at the University of Kentucky

By
Chenyu Zhao
Lexington, Kentucky

Director: Dr. Renbin Yan, Professor of Physics
Lexington, Kentucky
2023

Copyright© Chenyu Zhao 2023
<https://orcid.org/0009-0000-8710-1696>

ABSTRACT OF DISSERTATION

The Radial Quenching Progression of Nearby Galaxies

In this dissertation, we explore the spatial distribution of quiescent regions within galaxies using data from the Sloan Digital Sky Survey IV Mapping Nearby Galaxies at Apache Point Observatory (SDSS-IV MaNGA). Our analysis focuses on a radial range spanning from $0.3 R_e$ to $1.2 R_e$ and involves the development of innovative data selection and processing methods. Through this investigation, we identify two prominent types of transition galaxies: central-star-forming galaxies (C-SF galaxies) and central-quiescent galaxies (C-Q galaxies). Notably, we observe a correlation between galaxy mass and the predominant type of transition, with more massive galaxies tending to be C-Q galaxies and less massive galaxies leaning towards C-SF galaxies. To explain the formation of C-Q galaxies, we propose a duty cycle hypothesis, suggesting intermittent quenching processes. Additionally, we speculate that the rejuvenation of quiescent galaxies could be responsible for the presence of C-SF galaxies. Moving beyond the study of transition galaxies, we also examine the connection between active galactic nuclei (AGN) activity and star formation. Our findings reveal that AGN activities are associated with both the enhancement and cessation of star formation, depending on the star formation status in the outskirts of the galaxy. We present a hypothesis to explain this observation, shedding light on the intricate interplay between AGN and star formation in galaxy evolution. Through our comprehensive analysis, this dissertation expands our understanding of the spatial progression of quenching mechanisms, the distinct roles of transition galaxies, and the complex relationship between AGN and star formation.

KEYWORDS: galaxies, galaxy evolution, quenching, spatial distribution, nearby galaxies, Seyfert galaxies

Chenyu Zhao

August 2, 2023

The Radial Quenching Progression of Nearby Galaxies

By
Chenyu Zhao

Dr. Renbin Yan
Director of Dissertation

Dr. Christopher Crawford
Director of Graduate Studies

August 2, 2023
Date

To my beloved parents, whose unwavering love and guidance are the foundation of
all my achievements.

ACKNOWLEDGMENTS

I would like to express my heartfelt gratitude to all those who have contributed to the advancement of this field and have played a role in shaping this dissertation. My deepest appreciation goes to the researchers and scholars whose work I have cited throughout this study. Their pioneering efforts have laid the foundation upon which this research is built.

I am immensely grateful to my advisor, Renbin Yan, and all the committee members for their guidance, expertise, and unwavering support throughout my Ph.D. journey. Their mentorship has been invaluable, and I am grateful for the opportunities they provided me to grow and excel in my research.

I would also like to extend my gratitude to my parents and friends who have stood by me during this challenging academic pursuit. Their encouragement, understanding, and patience have been instrumental in my success. Their unwavering belief in my abilities has motivated me to persevere and complete this work.

Lastly, I would like to express my appreciation to all those who will read and engage with this dissertation. Your interest and feedback breathe life into this research, and I am grateful for the opportunity to contribute to the scholarly community. May this work endure and inspire future generations of researchers in their pursuit of knowledge and understanding.

We acknowledge support by NSF. Funding for the Sloan Digital Sky Survey IV has been provided by the Alfred P. Sloan Foundation, the U.S. Department of Energy Office of Science, and the Participating Institutions. SDSS acknowledges support and resources from the Center for High-Performance Computing at the University of Utah. The SDSS web site is www.sdss.org. SDSS is managed by the Astrophysical Research Consortium for the Participating Institutions of the SDSS Collaboration including

the Brazilian Participation Group, the Carnegie Institution for Science, Carnegie Mellon University, the Chilean Participation Group, the French Participation Group, Harvard-Smithsonian Center for Astrophysics, Instituto de Astrofísica de Canarias, The Johns Hopkins University, Kavli Institute for the Physics and Mathematics of the Universe (IPMU) / University of Tokyo, the Korean Participation Group, Lawrence Berkeley National Laboratory, Leibniz Institut für Astrophysik Potsdam (AIP), Max-Planck-Institut für Astronomie (MPIA Heidelberg), Max-Planck-Institut für Astrophysik (MPA Garching), Max-Planck-Institut für Extraterrestrische Physik (MPE), National Astronomical Observatories of China, New Mexico State University, New York University, University of Notre Dame, Observatório Nacional / MCTI, The Ohio State University, Pennsylvania State University, Shanghai Astronomical Observatory, United Kingdom Participation Group, Universidad Nacional Autónoma de México, University of Arizona, University of Colorado Boulder, University of Oxford, University of Portsmouth, University of Utah, University of Virginia, University of Washington, University of Wisconsin, Vanderbilt University, and Yale University.

This dissertation is dedicated to all those who have played a part, big or small, in making this endeavor possible.

TABLE OF CONTENTS

Acknowledgments	iii
List of Tables	vii
List of Figures	viii
Chapter 1 Introduction	1
1.1 Galaxies	1
1.2 Observation of Galaxies	1
1.3 Supermassive black holes and Active Galactic Nucleus(AGNs)	2
1.4 Classification of galaxies: Star-forming, quiescent, and the bimodality of galactic distribution	3
1.5 Galaxy evolution and quenching	6
Chapter 2 Data	9
2.1 Introduction to SDSS and MaNGA	9
2.2 MaNGA: IFU technique and DAP	9
2.2.1 Integral Field Unit, IFU	9
2.2.2 Data Analysis Pipeline, DAP	11
Chapter 3 Method	13
3.1 Classification of spaxels	13
3.1.1 Using $H\alpha$ and $[O II]$ equivalent width to separate star-forming and quiescent regions	14
3.1.2 Generalization to all spaxels	15
3.1.3 Seyfert regions of galaxies: modified BPT diagram	17
3.1.4 Summury of our method	18
3.2 The radial quenching profile of galaxies	19
3.3 Sample definition and incompleteness correction	19
3.3.1 Volume limitation of the MaNGA sample	20
3.3.2 Coverage and resolution limitations	20
3.3.3 Correction for those excluded galaxies	20
3.4 Classification of galaxies	21
3.4.1 Normal galaxies	21
3.4.2 AGN galaxies and weak-AGN galaxies	22
3.4.3 Excluded galaxies	22
Chapter 4 Properties of galaxies of different types	27
4.1 Properties of normal galaxies	27
4.1.1 Color-magnitude distribution and color mass distribution of different types	27

4.2	Properties of AGN and weak-AGN galaxies	27
4.3	Properties of excluded galaxies	29
4.4	Statics of types of galaxies	30
Chapter 5	Monotonic-transition galaxies	32
5.1	The transition radius	32
5.1.1	R_t versus stellar mass, $g-r$ color, and concentration	32
5.2	Stellar mass dependence of the distribution of C-Q and C-SF galaxies	33
5.3	Σ_1 comparisons	33
5.4	z -band concentration comparisons	37
5.5	Full spectrum fitting: pPXF with MaSTAR	41
5.5.1	Central regions of C-Q galaxies	43
5.5.2	Central regions of C-SF galaxies	43
5.5.3	Supplements: pPXF in the outskirts of MTGs	43
Chapter 6	Possibilities of AGN influence on quenching	49
6.1	AGN statistics	49
6.1.1	Statistics of weak-AGN	49
6.1.2	Statistics of AGN	49
6.2	Possible AGN influence on quenching	50
6.2.1	$H\alpha$ equivalent width approach	52
6.2.2	$H\alpha$ surface brightness profile	53
Chapter 7	Discussion	58
7.1	Non-AGN galaxies	58
7.1.1	Short-term features and long-term features	58
7.1.2	Central-Quiescent galaxies	58
7.1.3	Central-Star-Forming galaxies	59
7.2	AGN impact of star formation in galaxies	60
Chapter 8	Summary	62
Appendices	64
Appendix A:	Calculation of statistical values in a weighted sample.	64
Appendix B:	$H\alpha$ strength in different regions of galaxies	64
Appendix C:	Beam-smearing effect in Figures 5.5, 5.6	66
Appendix D:	Stellar population results from pPXF for different mass bins	67
	C-SF galaxies	67
	C-Q galaxies	75
Appendix E:	Demonstration of $H\alpha$ surface brightness	81
Bibliography	88
Vita	100

LIST OF TABLES

4.1	Frequencies of different sub-types include AGN and excluded galaxies. . .	31
4.2	Frequencies of different sub-types in non-AGN and weak-AGN galaxies. .	31
6.1	Frequencies of types of galaxies in AGN sample	52

LIST OF FIGURES

1.1	Hubble’s tuning fork diagram	4
1.2	Bimodality demonstration on color-mass diagram	5
2.1	A schematic diagram of MaNGA IFU	10
3.1	Display of the $H\alpha$ vs. $[O II]$ equivalent width histogram for galaxies with different colors and magnitudes.	24
3.2	Distribution of quiescent and star-forming regions in galaxies on traditional and reprojected BPT diagrams	25
3.3	Examples of six different subtypes of galaxies.	26
4.1	Relative density of six different subtypes on a color-mass diagram.	28
4.2	Effect of Seyfert-AGN selection on our sample.	29
4.3	Effect of coverage and resolution selection	30
5.1	Relationship between the transition radius and various properties of galaxies	34
5.2	Relationship between the transition radius and the specific star-forming rate	35
5.3	Relative fraction of central-quiescent and central-star-forming galaxies in different mass bins	36
5.4	Differences in Σ_1 between monotonic-transition galaxies and comparison samples	38
5.5	Illustration the average Σ_1 values of C-Q galaxies in a series of mass bins	39
5.6	Illustration the average Σ_1 values of C-SF galaxies in a series of mass bins	40
5.7	Difference in concentration between monotonic-transition galaxies and comparison samples	42
5.8	Comparison of the star formation history between the central regions of C-Q galaxies and the control sample	44
5.9	Comparison of the star formation history between the central regions of C-SF galaxies and the control sample	45
5.10	Comparison of the star formation history between the outskirts of C-Q galaxies and the control sample	46
5.11	Comparison of the star formation history between the outskirts of C-SF galaxies and the control sample	47
6.1	Demostration of AGNs	51
6.2	Comparison of the $H\alpha$ equivalent width of AGNs with quiescent outskirts	54
6.3	Comparison of the $H\alpha$ equivalent width of AGNs with star-forming outskirts	55
6.4	Illustration of the bi-peak feature of the $H\alpha$ surface brightness profile . .	57

Chapter 1 Introduction

1.1 Galaxies

Galaxies, the magnificent building blocks of the universe, are awe-inspiring structures that have captivated astronomers and space enthusiasts for centuries. These vast cosmic assemblages are home to billions, and possibly trillions, of stars and many other celestial objects. Galaxies provide us with a glimpse into the vastness of the cosmos and offer insights into the fundamental workings of the universe itself.

A galaxy can be defined as a gravitationally bound system consisting of stars, stellar remnants, interstellar gas, dust, and dark matter. These celestial entities come together to form a cohesive structure that can span immense distances and sizes, ranging from a few thousand light-years to several hundred thousand light-years in diameter. Within this vast expanse, galaxies exhibit a remarkable diversity in their shapes, sizes, and characteristics.

The study of galaxies, known as galactic astronomy, has significantly contributed to our understanding of the universe's origins, evolution, and structure. By observing and analyzing galaxies, scientists have unraveled key aspects of cosmology, such as the universe's expansion, matter distribution, and galaxies' formation.

1.2 Observation of Galaxies

The history of astronomy is rich with breakthroughs and milestones, and the observation of galaxies has played a pivotal role in expanding our knowledge of the universe. Over the years, advancements in technology and observational techniques have revolutionized our understanding of galaxies and their properties. Sky survey programs and integral field unit (IFU) techniques have been instrumental in unlocking the secrets of these cosmic entities.

Early observations of galaxies were limited due to the lack of powerful telescopes and the inability to discern individual stars within galaxies. Galaxies were often mistaken for nebulous objects or considered as parts of our own Milky Way galaxy. It was not until the early 20th century that astronomers, such as Edwin Hubble, made groundbreaking discoveries that revolutionized our understanding of galaxies.

In the 1920s, Edwin Hubble studied galaxies using the 100-inch Hooker Telescope at Mount Wilson Observatory. Through his observations, he made the groundbreaking discovery that some of the nebulae were separate galaxies outside our Milky Way. Hubble also established a correlation between the distances to galaxies and their red-shifts, demonstrating the expansion of the universe. This discovery became the foundation for the development of the concept of an expanding universe and led to the formulation of Hubble's Law.

As telescopes and observational techniques continued to advance, the need for systematic sky surveys became apparent. Sky survey programs, such as the Palomar Observatory Sky Survey (POSS) ([52]) and the Sloan Digital Sky Survey (SDSS) ([35]),

played a crucial role in mapping the distribution and properties of galaxies on a large scale.

In the late 20th century and into the 21st century, the advent of digital imaging and spectroscopy revolutionized sky surveys. The Sloan Digital Sky Survey (SDSS), initiated in 2000, employed advanced digital cameras and spectrographs to capture detailed images and spectra of millions of galaxies. The SDSS has become one of the most influential astronomical surveys, encompassing multiple phases and extensions. It has provided an unprecedented amount of data and has made substantial contributions to our understanding of galaxies and the universe’s large-scale structure.

The SDSS mapped the sky and created comprehensive catalogs of galaxies, stars, quasars, and other celestial objects. It played a significant role in characterizing the properties of galaxies, such as their luminosity, color, morphology, and redshift. The SDSS data has been extensively used in studying galaxies’ large-scale distribution, galaxy populations’ evolution, and the identification of rare objects.

In recent years, the SDSS has expanded its capabilities to include more detailed observations of galaxies through the Mapping Nearby Galaxies at Apache Point Observatory (MaNGA) program([17]). MaNGA utilizes an integral field unit (IFU) technique to obtain spatially resolved spectroscopy of thousands of nearby galaxies([27, 73, 48]). With MaNGA, astronomers can study the internal structures, gas dynamics, and chemical compositions of galaxies in unprecedented detail.

The MaNGA program provides high-quality spectra for each individual spacial element (or ‘spaxel’) within a galaxy, allowing for the construction of detailed maps of various properties, such as star formation rates, stellar populations, and gas velocities. This wealth of information enables researchers to investigate the connections between galaxy morphology, internal dynamics, and the underlying physical processes that shape galaxies.

MaNGA has significantly contributed to our understanding of galactic evolution, the interplay between galaxies and their environments, and the diversity of properties within different regions of galaxies. The IFU observations from MaNGA, combined with other SDSS data, have fueled numerous studies on galaxy formation and evolution, galactic archaeology, and the relationships between star formation, black hole activity, and the overall structure of galaxies.

1.3 Supermassive black holes and Active Galactic Nucleus(AGNs)

The study of galaxies has led to the realization that most galaxies host supermassive black holes at their centers([45, 33, 29]). These enigmatic objects, millions or even billions of times more massive than our Sun, play a crucial role in galaxy evolution, shaping the surrounding environment and influencing the growth and behavior of the galaxy itself.

Supermassive black holes are believed to form through various mechanisms. One proposed scenario is the rapid accretion of mass onto a smaller, stellar-mass black hole during galactic mergers or interactions([46, 54]). Over time, as matter accretes onto the black hole, its mass grows exponentially, ultimately reaching the supermassive scale. Another possibility is the direct collapse of enormous clouds of gas during the

early stages of galaxy formation, leading to the formation of massive black holes from the outset([7]).

AGNs are powerful engines fueled by supermassive black holes([50, 64]). These active and luminous regions at the centers of galaxies emit copious amounts of radiation across the electromagnetic spectrum, from radio waves to X-rays and gamma rays. AGNs are characterized by their incredibly high luminosities, often exceeding the combined output of billions of stars in their host galaxies.

The intense radiation emitted by AGNs arises from the process of accretion—the gravitational capture and consumption of surrounding matter by the supermassive black hole. As matter falls into the black hole’s gravitational well, it forms a swirling disk known as an accretion disk. The friction and collisions within the disk generate enormous amounts of energy, producing intense radiation and launching powerful jets of particles and radiation outward from the black hole’s vicinity.

AGNs come in various forms, each exhibiting distinct observational characteristics. Quasars are the most luminous type of AGN, visible from vast distances, while Seyfert galaxies are lower-luminosity counterparts found in closer galactic neighborhoods. Blazars are a subclass of AGNs characterized by their highly variable and polarized emission, often associated with relativistic jets pointed directly toward Earth.

The study of AGNs and supermassive black holes has significantly advanced our understanding of fundamental astrophysical processes. They provide insights into the mechanisms of mass accretion, the interplay between black holes and their surrounding environments, and the impact of AGN feedback on galaxy evolution. AGNs can profoundly influence their host galaxies by regulating star formation, expelling gas, and shaping the galactic environment.

Observational techniques such as spectroscopy, interferometry, and multi-wavelength surveys have played a crucial role in the study of supermassive black holes and AGNs. Ground-based telescopes and space observatories equipped with advanced instruments, such as the Hubble Space Telescope, Chandra X-ray Observatory, and the Atacama Large Millimeter Array (ALMA), have provided detailed observations and measurements, enabling scientists to unravel the mysteries of these extreme cosmic phenomena.

1.4 Classification of galaxies: Star-forming, quiescent, and the bimodality of galactic distribution

Galaxies are classified into different types based on their visual appearance, which provides valuable insights into their formation and dynamics. The most common classification scheme, proposed by Edwin Hubble in the 1920s, categorizes galaxies into three main types: spiral, elliptical, and irregular([39, 40]). Figure 1.1 demonstrates this classification scheme. Spiral galaxies, characterized by their distinct spiral arms, are often seen as majestic whirlpools of stars, gas, and dust. Elliptical galaxies, on the other hand, appear as smooth, featureless ellipsoids and lack the spiral arms seen in their counterparts. Irregular galaxies encompass a variety of shapes, often resulting from gravitational interactions or disturbances within their environments. Beyond these three primary types, astronomers have discovered other unique variations, such

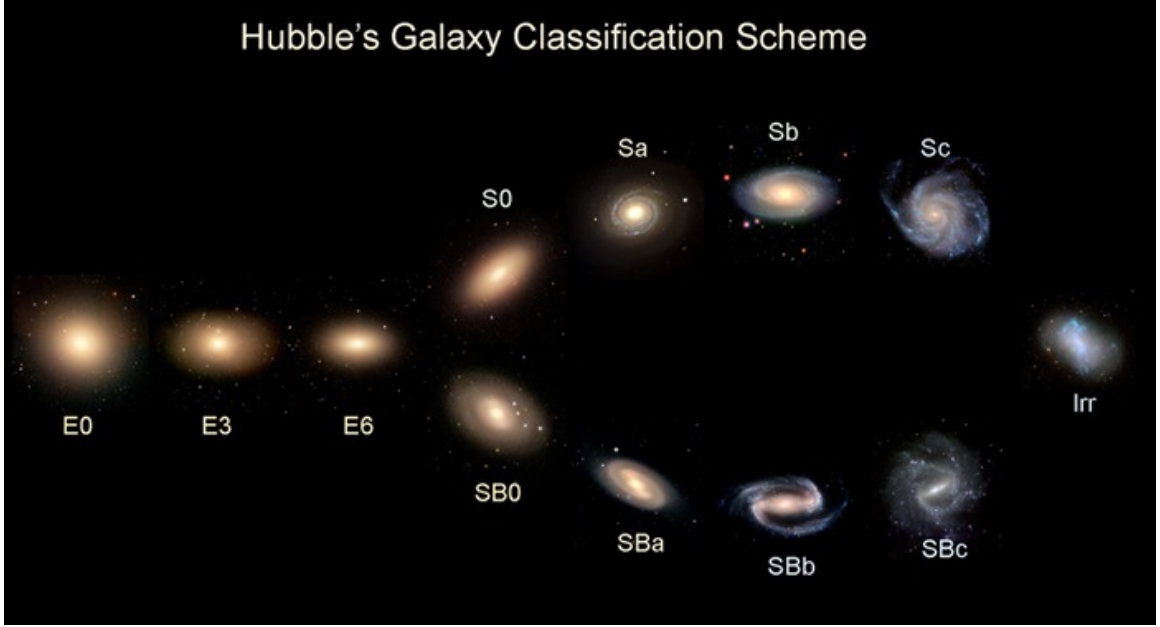


Figure 1.1: This figure displays the iconic ‘Hubble’s tuning fork’ diagram, which showcases various types of galaxies. The left-hand side exhibits elliptical galaxies, followed by spiral galaxies, with or without bars. On the right-hand side, irregular galaxies are presented. This diagram has been adapted from [53].

as barred spiral galaxies, lenticular galaxies, and dwarf galaxies. Each category holds valuable clues about the underlying physical processes that shape and govern galaxy formation and evolution.

We can also classify galaxies based on whether they still have new stars forming([14]). Galaxies can be broadly categorized into two main types based on their star formation activity: star-forming galaxies and quiescent galaxies. These classifications reveal distinct characteristics and provide insights into the processes that shape galactic evolution. Additionally, the distribution of galaxies displays a bimodal pattern, indicating two dominant populations with differing properties. Figure 1.2 demonstrate this bimodal pattern on a color-mass diagram.

Star-forming galaxies are dynamic cosmic entities where active star-formation processes occur. These galaxies contain regions within them where clouds of gas and dust collapse under gravity, giving rise to the birth of new stars. Intense star formation rates are often observed in these galaxies, resulting in a significant population of young, massive, and hot stars. These stars’ ultraviolet radiation ionizes the surrounding gas, creating emission nebulae known as HII regions. Star-forming galaxies typically exhibit a blue color due to the presence of young, hot stars.

In contrast, quiescent galaxies experience a substantial decline or cessation of star formation activity. These galaxies are characterized by a predominantly older stellar population and a lack of ongoing star formation. The star formation quenching can be attributed to various mechanisms, including the depletion or removal of interstellar gas required for star formation. Quiescent galaxies often have a more spheroidal or

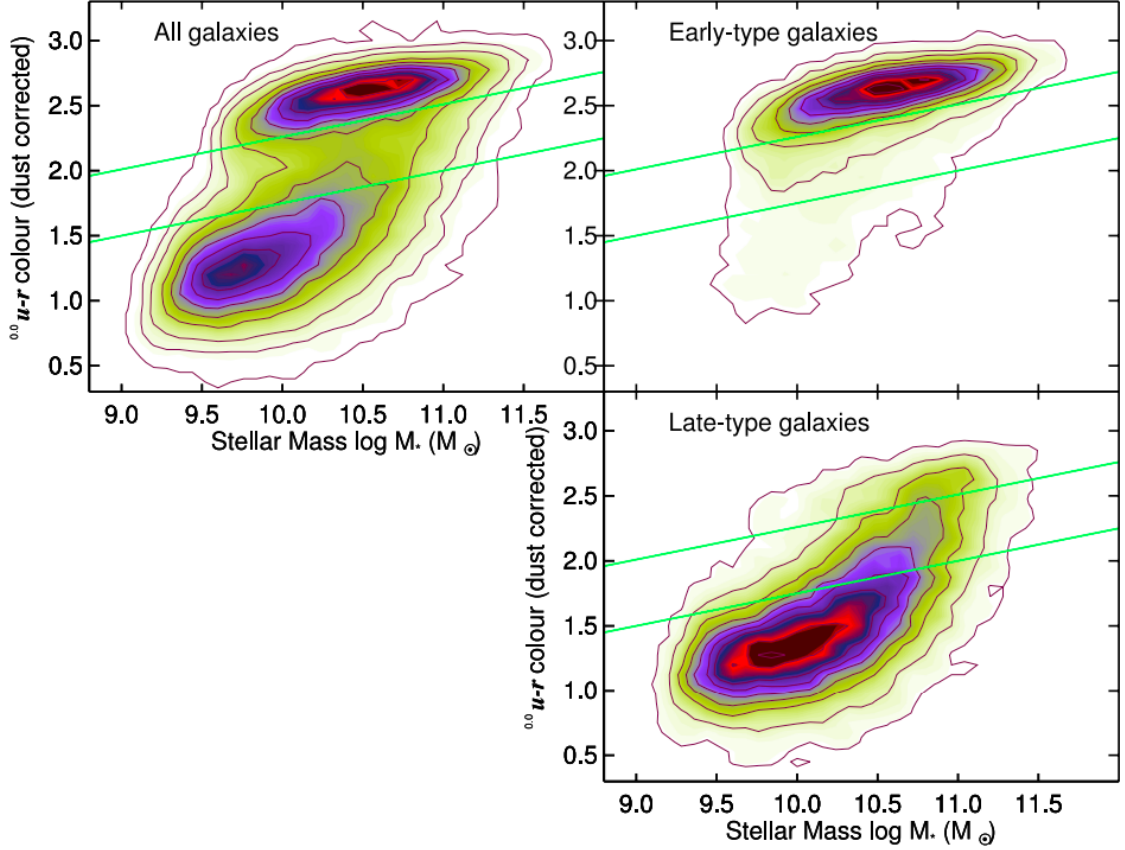


Figure 1.2: This figure showcases the bimodal distribution of galaxies on the color-mass diagram. The x-axis represents the total stellar mass, while the y-axis signifies the $u-r$ color, corrected for dust. As evident in the upper-right panel, there is a distinct bimodal distribution of galaxies. The panels on the right demonstrate that the observed bimodality aligns well with galaxy types. This figure is adapted from [62].

elliptical shape and display redder colors due to the dominance of older, cooler stars.

The distribution of galaxies across the universe exhibits a bimodal pattern known as the bimodality of galaxy distribution. This bimodality refers to the presence of two dominant populations of galaxies with distinct properties. One peak represents the population of star-forming galaxies, while the other corresponds to the population of quiescent galaxies. Using large imaging and spectroscopy galaxy surveys, the bimodalities of galaxies in many observational properties are well established ([67, 37, 3, 5, 26], and references therein). Based on optical colors, most galaxies can be classified into blue and red galaxies. This color bimodality is a reflection of the star formation activity in galaxies: blue galaxies correspond largely to actively star-forming ones, and red galaxies correspond largely to those that have little or no ongoing star formation but a relatively old stellar population. We refer to these non-star-forming galaxies as quiescent galaxies.

The bimodality of galactic distribution is closely linked to environmental factors and galaxy interactions([2]). In regions where galaxy clusters and groups are prevalent, processes such as gas stripping, gravitational interactions, and mergers between galaxies can influence their evolution. Interactions between galaxies can trigger intense star formation episodes, leading to the formation of star-forming galaxies. Conversely, these interactions can also deplete or remove interstellar gas, resulting in the transformation of star-forming galaxies into quiescent ones.

Understanding the transition from star-forming to quiescent galaxies and the factors that drive the bimodal distribution is a significant area of research. It provides valuable insights into the mechanisms that regulate and quench star formation in galaxies, the evolution of galactic morphology, and the interplay between galaxies and their environments. By studying the properties and distribution of galaxies, astronomers gain a deeper understanding of the fundamental processes that shape the cosmos we inhabit.

1.5 Galaxy evolution and quenching

Observations have revealed that the volume density of red galaxies is not constant throughout cosmic time. Studies have shown that it has at least doubled from $z \sim 1$ to $z \sim 0$ ([12, 16, 30]). Conversely, research has demonstrated a decline in the volume density of star-forming galaxies for the range $z < 1$ ([24, 32, 57]). These findings indicate that many galaxies undergo a transition from star-forming to quiescent states over time.

Galaxies often transform from a spiral to an elliptical structure through mergers. However, the observed rate of galaxy mergers alone cannot fully account for the transition of all galaxies from the ‘blue cloud’ to the ‘red sequence’ or the cessation of star formation within galaxies. Therefore, theories of galaxy evolution must address the mechanisms responsible for the suppression of star formation, commonly known as galaxy ‘quenching.’ However, the precise mechanism driving this transition remains unclear.

The process of quenching, which describes the halt of star formation in previously active galaxies, is not well understood ([11, 42, 3]). Several mechanisms have been proposed, including AGN feedback ([66, 38]), morphology quenching ([51]), ram pressure stripping ([34]), and strangulation ([55]), among others. Some of these mechanisms suggest an inside-out progression, while others propose an outside-in progression.

Understanding the specific mechanisms responsible for quenching and the factors that drive the transition of galaxies is a topic of active research in astrophysics. Various observational techniques and theoretical models are employed to study transition galaxies, including multi-wavelength observations, spectroscopy, and simulations. These investigations aim to identify the physical processes, such as gas stripping, mergers, or internal secular evolution, that contribute to the transformation of galaxies from star-forming to quiescent states.

Studying transition galaxies and the quenching process provides valuable insights into the evolution of galaxies and the broader context of cosmic structure formation.

It helps us understand the factors that regulate star formation, the role of the environment in shaping galactic properties, and the connections between the growth of supermassive black holes and galaxy quenching. Furthermore, transition galaxies bridge the gap between actively star-forming galaxies and quiescent systems, shedding light on the diverse pathways of galactic evolution and the intricate interplay between internal and external influences on a galactic scale.

However, one complication of this is that the transition from star-forming galaxies to quiescent galaxies is not necessarily a one-way process. Quiescent galaxies may also restart star formation again, which is usually referred to as rejuvenation. This could account for the recent starburst activity observed in a significant fraction of quiescent galaxies ([61, 31, 22]).

One promising approach to distinguish between them is to study the radial distribution of quiescent regions and star-forming regions in galaxies to help infer the radial progression of quenching. Although it may not be possible to identify the correct mechanism definitively, this approach can help narrow down the possibilities.

There have been many works in the past using spatial gradients in color or stellar population properties to investigate the temporal sequence for the quenching of star formation. For example, [49] studied the $\text{NUV}-u$ and $u-i$ color gradients in a sample of nearby galaxies. Based on the assumption that most galaxies follow the same kind of parametric star formation history, they concluded that the gradient distributions are more consistent with an inside-out growth model in which the inner regions of galaxies have a faster formation timescale than the outer regions.

[70] studied the spatial gradients in $Dn(4000)$, $\text{H}\delta$ absorption equivalent width(EW), and $\text{H}\alpha$ emission equivalent width(EW) in a sample of MaNGA galaxies. They found that there is a critical mass threshold above which star-forming galaxies or partly star-forming galaxies present significant gradients, implying star formation in them is shut down from the inside out. Below that mass threshold, galaxies tend to show no or very weak gradients in those diagnostics, implying galaxies evolve synchronously across all radii.

[8] studied quenching of star formation in MaNGA galaxies by looking at the specific star formation rate (sSFR) profile in star-forming galaxies and green-valley galaxies. They also found that the suppression of star formation is happening synchronously across all radii in a galaxy rather than in an expanding central-quiescent region.([28])

Different from these works, we are going to investigate this issue using a more robust way to distinguish star-forming regions from quiescent regions and define a sample with uniform spatial resolution in physical scales. We will pay closer attention to the distribution and sizes of quiescent regions and star-forming regions to see how they depend on galaxy properties.

The MaNGA (Mapping Nearby Galaxies at Apache Point) project provides integral field unit (IFU) data for 10,010 unique nearby galaxies ([17]). With these data, we can study galaxies as a whole and examine the spatial distribution of star-forming regions and quiescent regions in galaxies. In contrast to the traditional classification of galaxies as star-forming, quiescent, or Seyfert, galaxies can exhibit hybrid characteristics. While Seyfert-like galaxies exist in our sample, they are relatively rare

compared to star-forming and quiescent galaxies. Therefore, in this paper, we will focus on the star-forming and quiescent populations and not delve into the details of Seyfert galaxies. We assign a quiescent possibility to each spaxel in our data and calculate the weighted quiescent possibility inside each radial bin. By plotting these fractions over radius, we can construct a radial profile of galaxies. This approach enables us to classify galaxies into more subtypes than just quiescent and star-forming and examine the features of these subtypes individually.

In Chapter 2, we provide a brief introduction to the data used in this study. Chapter 3 discusses the selection of subtypes and presents the distribution of these subtypes in a volume-limited sample. In Chapter 4, we focus on two subtypes of transition galaxies that we find particularly interesting, and Chapter 5 explores possible explanations for the formation of these galaxies. Chapter 6 demonstrates several possible AGN impact on the star formation in the host galaxies. Then in Chapter 7, we discuss several possible explanations for our findings. Finally, in Chapter 8, we summarize our findings. Throughout this work, we adopt a flat Λ CDM model with $H_0 = 70 \text{ km s}^{-1} \text{ Mpc}^{-1}$, $\Omega_m = 0.3$, and $\Omega_\Lambda = 0.7$.

Chapter 2 Data

2.1 Introduction to SDSS and MaNGA

The Sloan Digital Sky Survey (SDSS) is a pioneering astronomical survey that has greatly contributed to our understanding of the universe([76]). Initiated in 2000, the SDSS has been instrumental in mapping and cataloging a vast number of celestial objects, including galaxies, stars, quasars, and asteroids.

The SDSS utilizes a dedicated 2.5-meter telescope located at Apache Point Observatory in New Mexico, USA. Equipped with a suite of advanced instruments, including large-format digital cameras and spectrographs, it is capable of capturing detailed images and spectra of celestial objects across a wide range of wavelengths.

The SDSS has undergone several phases and extensions, each pushing the boundaries of astronomical research. The original SDSS-I, completed in 2005, surveyed a significant portion of the sky, providing data for over 800,000 galaxies and 120,000 quasars. SDSS-II, carried out from 2005 to 2008, focused on obtaining spectra for a large number of stars and galaxies, further expanding our knowledge of these objects.

One of the most notable achievements of the SDSS is the creation of the most extensive and detailed three-dimensional maps of the universe to date. SDSS-III, conducted from 2008 to 2014, undertook the ambitious Baryon Oscillation Spectroscopic Survey (BOSS)([25]), which mapped the distribution of galaxies and traced the imprint of cosmic sound waves from the early universe. This survey has provided invaluable insights into the large-scale structure of the universe and the nature of dark energy.

In recent years, the SDSS-IV project has continued to advance our understanding of the cosmos. Among its notable programs is the Mapping Nearby Galaxies at Apache Point Observatory (MaNGA). MaNGA employs an integral field unit (IFU) technique to obtain spatially resolved spectroscopy for a large sample of nearby galaxies. This allows for detailed mapping of the composition, kinematics, and stellar populations across the galaxies.

MaNGA aims to provide comprehensive understanding of the processes driving galaxy evolution by studying the connections between a galaxy’s internal structure and its formation history. The survey has generated an unprecedented wealth of data, including spectral information for over 10,000 galaxies, making it one of the most extensive IFU surveys to date.

2.2 MaNGA: IFU technique and DAP

2.2.1 Integral Field Unit, IFU

MaNGA employs the integral field unit (IFU) technique, which allows for spatially resolved spectroscopy of galaxies([17, 73]). Traditional spectroscopic observations obtain spectra from a single point or a small aperture within a galaxy, limiting our

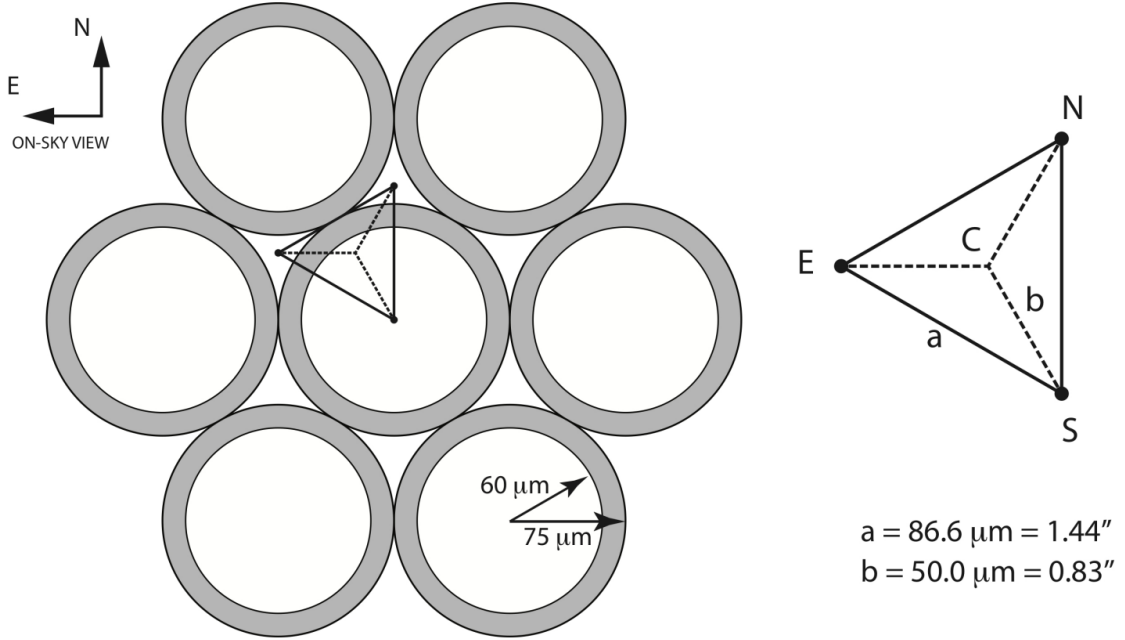


Figure 2.1: Schematic diagram of the 7 central fibers within a hexagonally-packed MaNGA IFU, showing the 120 micron diameter fiber core and surrounding cladding plus buffer. The triangular figure shows the relative positions of the three dither positions; the fiber bundle is located at position ‘S’. The central (C) ‘home’ position is labeled, along with the north (N), south (S), and east (E) dither positions. The nominal plate scale of the SDSS telescope is 217.7358 mm/degree, or 60.48 microns/arcsec. This plot is from [48]

understanding of the complex dynamics and composition across the entire galaxy. In contrast, the IFU technique simultaneously collects spectra from multiple points across the galaxy, creating a detailed two-dimensional map of the galaxy’s properties.

The MaNGA IFU system consists of bundles of optical fibers that are densely packed into a hexagonal array. Each fiber is assigned to a specific spatial location on the sky, allowing for the collection of spectra at precise locations across the target galaxy. The number of fibers and their sizes determine the spatial resolution and coverage of the observations. A schematic demonstration of MaNGA IFU is demonstrate in figure 2.1

The IFU observations performed by MaNGA cover a broad wavelength range, typically from the ultraviolet to the near-infrared. The collected spectra provide information about various physical properties, such as gas velocities, chemical abundances, stellar populations, and ionization states.

The spatially resolved spectra obtained by MaNGA enable the construction of detailed maps of key parameters within galaxies. For example, velocity maps reveal the rotation and motion patterns of stars and gas, allowing astronomers to study the internal dynamics and gravitational interactions within galaxies. Stellar population maps provide insights into the age and metallicity distribution of stars, shedding light

on the galaxy’s formation history. Ionization maps help to identify regions of active star formation, the presence of active galactic nuclei, and other energetic processes occurring within galaxies.

The MaNGA survey has been an invaluable resource for studying the diversity of galaxies and the physical processes that drive their evolution. The large sample size, consisting of over 10,000 galaxies, has allowed for statistically robust analyses of galactic properties, their relationships to the large-scale structure of the universe, and the connections between internal galaxy structures and their formation histories.

The data are initially processed by the MaNGA data reduction pipeline (DRP, [47, 73]) to create sky-subtracted and flux-calibrated three-dimensional data cubes. They are subsequently analyzed using the MaNGA data analysis pipeline (DAP, [71, 10]), which produces a broad range of physical property maps, including stellar and gas kinematics, emission line flux, equivalent width, spectral indices, and other features.

2.2.2 Data Analysis Pipeline, DAP

The Data Analysis Pipeline (DAP, [71, 10]) is an essential component of the MaNGA project, providing a systematic and automated process for extracting valuable scientific information from the massive amount of data collected by MaNGA’s integral field unit (IFU) spectrographs.

The DAP is designed to perform a comprehensive analysis of the MaNGA data, allowing researchers to extract and interpret the physical properties of galaxies, such as stellar populations, gas kinematics, and emission line strengths, across the large sample of observed galaxies. The pipeline ensures uniform and consistent analysis of the diverse MaNGA dataset, enabling reliable comparisons and statistical studies.

The DAP follows a series of steps to process the MaNGA data and extract the desired scientific quantities. These steps include data reduction, spectral fitting, and the generation of a suite of derived quantities for each target galaxy.

The data reduction process involves calibrating the raw IFU data, correcting for instrumental effects, removing sky background contributions, and handling various observational artifacts. This step ensures that the data is in a suitable form for subsequent analysis.

Spectral fitting is a crucial component of the DAP, where the pipeline models the observed spectra to extract physical properties. The pipeline utilizes sophisticated algorithms and spectral synthesis techniques to fit the observed spectra with stellar population models, emission line models, and other relevant models. This process allows for the determination of parameters such as stellar ages, metallicities, star formation rates, gas kinematics, and other key properties of the target galaxies.

The DAP generates a comprehensive suite of derived quantities, including maps, spectra, and other diagnostic plots, that provide insights into the internal structures and physical processes occurring within galaxies. These derived quantities are essential for studying the relationships between different properties, exploring spatial variations within galaxies, and conducting comparative analyses across the MaNGA sample.

The DAP also incorporates extensive quality control measures to ensure the reliability and accuracy of the derived results. This includes automated assessments of the goodness-of-fit, data quality, and other metrics to identify any potential issues or outliers in the analysis.

The outputs of the DAP are made publicly available, allowing the broader astronomical community to access and utilize the derived data for their own research. This open data policy encourages collaboration, fosters reproducibility, and maximizes the scientific impact of the MaNGA survey.

The DAP has enabled a wide range of scientific investigations using the MaNGA data. It has facilitated studies on galaxy evolution, the connections between galactic structure and stellar populations, the relationships between gas and stars, and the role of internal and environmental factors in shaping galaxies.

In this study, we use data from MaNGA Product Launch 11(MPL-11), which is identical to the data released in the SDSS Data Release 17(DR17, [1]). The data analysis pipeline products vary according to different templates and binning schemes, known as DAPTYPEs. Our analysis employs the HYB10-MILESHC-MASTARHC2 DAPTYPE, which utilizes Voronoi binning([19]) in the stellar kinematics analysis with MILESHC templates. The emission-line fitting, however, is carried out on individual spaxels utilizing the MASTARHC templates to model the stellar continuum. For details of this and for the explanation of the acronyms, see [71]. The approach used in this study is ideally suited for the current investigation.

To supplement the DAP products, we also use the stellar mass surface density maps created by the PIPE3D pipeline([58]), which is an independent analysis pipeline from DAP. Pipe3D stands for ‘Pipelines for the Analysis of 3D data,’ and it serves as a comprehensive pipeline specifically tailored for processing MaNGA IFU data. It offers a suite of advanced algorithms and techniques to extract valuable information about the physical properties, kinematics, and structures of galaxies from the observed spectra. We obtain the overall properties of galaxies, such as total stellar mass, absolute magnitude in different bands, and the effective radius, from the NASA Sloan Atlas catalog(NSA catalog, [15]). This catalog determines the effective radii, axis ratios, and position angles from the SDSS r-band images using an elliptical Petrosian approach. Specifically, the effective radius corresponds to the semi-major axis of the ellipse containing 50% of the flux within the elliptical Petrosian aperture, which extends the original Petrosian definition([56]).

Chapter 3 Method

The primary objective of this study is to investigate the spatial evolution of quenching in galaxies. To achieve this aim, it is necessary to determine the spatial distribution of both quiescent and star-forming regions within galaxies. This necessitates the development of appropriate methodologies to distinguish between quiescent and star-forming spaxels, as well as to ascertain their relative spatial locations within galaxies. The subsequent sections provide an overview of the methodologies employed in this study.

3.1 Classification of spaxels

There are several methods to classify the spaxels of galaxies into star-forming and quiescent ones, each with its own advantages and limitations. One commonly used method is to adopt the star-forming rate of spaxels/galaxies and plot them against mass or luminosity ([68, 59]). However, this approach relies on obtaining a reliable star formation rate indicator, which may not be trivial to achieve. For instance, using the flux of the $H\alpha$ emission line to measure the star formation rate requires correcting for dust attenuation, which can be very uncertain when the emission lines are weak.

Another method involves using the Baldwin, Phillips, and Terlevich (BPT) diagram ([4]), which uses emission-line ratios to differentiate between star-forming regions and other ionization mechanisms, such as active galactic nuclei (AGN) or low-ionization emission-line regions (LIERs). While the BPT diagram provides a good separation between star formation and other mechanisms, it requires several emission lines to be significantly detected, some of which may be relatively weak. Consequently, this method may not be effective for spaxels with low signal-to-noise ratios, especially in the outskirt regions of galaxies where emission lines are generally weak.

A third method, proposed by [75] (hereafter Y06), uses the equivalent width of two emission lines, $H\alpha$ and $[O II]$, which are usually strong in both star-forming and quiescent galaxies. As this method requires only the two strongest lines, it can include nearly all spaxels in its implementation, thereby minimizing spaxel loss, even when an S/N cut is applied. It is based on a demarcation in a plot of $[O II]$ equivalent width versus $H\alpha$ equivalent width to separate star-forming regions from quiescent regions, with LIERs included in the latter. Equivalent width, rather than flux, is used to minimize the effect of dust attenuation. However, the performance of this method may not be guaranteed when dealing with AGN, which can be identified using the BPT diagram as a supplement.

It is important to note that LIERs, which have the same line ratios as low-ionization nuclear emission-line regions (LINERs), are not limited to the nuclear region of galaxies ([60, 72, 65, 9]). Therefore, LIER is a more appropriate and general term for regions with LINER-like line ratios. This work considers regions/galaxies with LIER emission as quiescent since they have no star formation. The origin of

LIER emission is still under debate and remains largely unclear. However, this topic will not be discussed further in this work.

3.1.1 Using $H\alpha$ and [O II] $\lambda\lambda 3726, 3729$ equivalent width to separate star-forming and quiescent regions

Y06 showed that in a plot of [O II] $\lambda\lambda 3726, 3729$ equivalent width (EW) versus $H\alpha$ equivalent width (EW), galaxies appear to concentrate in two regions that correspond to the quiescent and star-forming categories. A demarcation line was drawn to separate the two regions, with galaxies to the left of the line including both LINER-like galaxies, with high [O II] EW and low $H\alpha$ EW, and galaxies with no detectable emission lines. These galaxies were found to distribute exclusively on the red sequence in the color-magnitude diagram, indicating quiescence. While galaxies to the right of the demarcation line are found to have line ratios consistent with star formation, most of which are on the blue cloud with a small fraction on the red sequence. Those that appear red are likely due to dust attenuation. Thus, this method is superior to color-based methods as dusty star-forming galaxies may appear red but would fall to the right of the demarcation lines and can thus be accurately classified using this method. However, the original tests of this method were only performed on the single fiber SDSS data, which only covers the central part of galaxies. To ensure the efficacy of this method in the outskirts of galaxies, further testing on MaNGA data is required. In this study, we utilize the $H\alpha$ and [O II] $\lambda\lambda 3726, 3729$ emission line data from MPL11 DRP data to distinguish between star-forming and quiescent regions in galaxies. In Figure 3.1, we illustrate the correspondence between the optical colors of galaxies and the distribution of their spaxels in $H\alpha$ vs. [O II] EW plot. We select four groups of galaxies according to their color and magnitude, as shown in the left panels: starting from the red sequence in the top panel and going to bluer colors in the following rows. For each group of galaxies, a contour plot is generated for all the spaxels of those galaxies in the $H\alpha$ and [O II] EW plot and shown on the right. As expected, the spaxels are observed to cluster in two distinct regions separated by the demarcation line provided by Y06. It can be seen that the red sequence galaxies are dominated by spaxels distributed to the left of the demarcation, blue galaxies are dominated by spaxels distributed to the right, while green-valley galaxies have both kinds of spaxels.

To confirm the nature of spaxels classified using this demarcation, we select those spaxels among them that have all major emission lines detected above 3σ , and show their distributions in line ratio diagnostic diagrams in Figure 3.2. The top panels show their distributions in one traditional BPT diagram, [O III]/ $H\beta$ vs. [S II]/ $H\alpha$. The spaxels to the left of the Y06 demarcation in [O II]- $H\alpha$ EW plot are found in the AGN/LINER region of the BPT diagram (upper-left panel) while spaxels to the right of the Y06 demarcation are found in the star-forming region of the BPT diagram (upper-right panel).

In the bottom panels of Figure 3.2, we further show the separation using a re-projected BPT diagram proposed by [41]. This BPT diagram is a reprojection of the 3D line ratio space composed of [N II] $\lambda 6583/H\alpha$, [S II] $\lambda\lambda 6716, 6731/H\alpha$, and

[O III] $\lambda 5007/H\beta$. It has several advantages. It minimizes projection effects that plagued the traditional BPT diagrams by placing the model grid surfaces in edge-on perspectives; it removes ambiguity in classification by considering all three line ratios; and it enables definitions of demarcations with certain contamination fractions. In this diagram, the star-forming locus distributes on the left, while the AGN/LIER spaxels distribute on the right. The red demarcation curve corresponds to a combination of 90% SF and 10% AGN to the $H\alpha$ flux, while the blue demarcation corresponds to a combination of 10% SF and 90% AGN, and the green curve in the middle corresponds to a 50-50 split between SF and AGN for $H\alpha$. It can be seen that the Y06 demarcation could lead to a wide separation of spaxels in this diagram as well. All those star-forming spaxels, according to Y06, are on the star-forming locus in this diagram, while all those quiescent spaxels, according to Y06, are on the AGN/LIER region of this diagram. However, the 50-50 split curve seems inappropriate here, which is likely caused by the LIERs not having exactly the same intrinsic line ratio as AGNs. This does not affect the proof that the Y06 demarcation is effective at separating star-forming spaxels from LIER spaxels.

The concentration to the upper-left of the demarcation corresponds to regions with LIER emissions and regions with no detectable emission lines, while the lower-right region corresponds to star-forming emissions. As discussed in Section 3.1, we classify LIER regions as quiescent. As expected, the relative number of quiescent spaxels is higher among redder galaxies, and the relative number of star-forming spaxels is higher among bluer galaxies.

This confirms that the upper-left region corresponds to quiescent spaxels, while the lower-right region corresponds to star-forming spaxels. We verify that the demarcation line from [75] still works on MaNGA data and can distinguish between the two populations of star-forming and quiescent spaxels. This finding is further supported by the BPT diagram presented in Section 3.1.1, where we plot the star-forming and quiescent regions separated by the demarcation line and verify that they correspond to star-forming and non-star-forming regions in the BPT diagram. The combined evidence assures us that the method in [75] works effectively on MaNGA data.

3.1.2 Generalization to all spaxels

In the MaNGA data, each spaxel is associated with a corresponding noise level, resulting in a signal-to-noise (S/N) ratio. For spaxels with a low S/N ratio, it can be difficult to confidently classify them as belonging to either side of the Y06 demarcation line. To avoid excluding a significant fraction of spaxels and introducing bias to the sample, we refrain from using an S/N ratio cutoff in the selection process. Instead, we adopt a Bayesian inference approach to evaluate the probability of each spaxel belonging to either side of the demarcation line. In general terms, Bayesian inference involves updating the probability of a hypothesis based on new evidence by computing the conditional probability of the hypothesis given the evidence, using Bayes' theorem.

As a general statement, we can state Bayesian inference as follows:

$$P(\mathbf{H}|\mathbf{E}) = \frac{P(\mathbf{E}|\mathbf{H})P(\mathbf{H})}{P(\mathbf{E})}$$

Bayesian inference is a statistical method that allows us to update our beliefs (represented by a hypothesis, \mathbf{H}) based on the observed data (represented by evidence, \mathbf{E}). The resulting updated belief is the posterior probability, $P(\mathbf{H}|\mathbf{E})$, which is the probability of \mathbf{H} given \mathbf{E} . The likelihood, $P(\mathbf{E}|\mathbf{H})$, is the probability of observing the evidence \mathbf{E} given the hypothesis \mathbf{H} . The prior probability, $P(\mathbf{H})$, represents our initial belief about \mathbf{H} before observing \mathbf{E} , and the marginal likelihood, $P(\mathbf{E})$, is the probability of observing \mathbf{H} regardless of any hypothesis.

To apply Bayesian inference to our sample, we use the hypothesis that a certain observed spaxel belongs to the quiescent side (upper-left side) of the demarcation line, and the evidence is the observed data. To estimate the likelihood, we assume that the error distributions of the $\text{H}\alpha$ and $[\text{O II}]$ equivalent widths are Gaussian and that the reported uncertainties represent the corresponding sigma. We can then construct a two-dimensional Gaussian distribution for each data point with a specific combination of $\text{H}\alpha$ and $[\text{O II}]$ equivalent widths and their uncertainties.

In addition, we approximate the prior probability distribution by the overall distribution of our data points, assuming equal weight for each data point. Therefore, the likelihood for a particular data point i multiplied with the prior, $P(\mathbf{E}_i|\mathbf{H})P(\mathbf{H})$, can be expressed as a summation over all the hypothetical origins, \mathbf{H}_j , for generating that data point, which then can be approximated as a summation of all data points corresponding to some model space.

$$P(\mathbf{E}_i|\mathbf{H})P(\mathbf{H}) = \sum_{j \in \mathbf{H}} P(\mathbf{E}_i|\mathbf{H}_j)P(\mathbf{H}_j) = \sum_{j \in \mathbf{H}} P(\mathbf{E}_i|\mathbf{E}_j)$$

Since we use the data to approximate the hypothesis, the summation range controls the hypothesis. If we only do the summation over quiescent spaxels, we estimate the probability that \mathbf{E}_i is generated by the quiescent model; if we do the summation over all data points, we estimate the probability that \mathbf{E}_i is generated by all models, which is the marginal likelihood, $P(\mathbf{E})$, and the normalization factor. Thus, the probability of a spaxel belonging to the quiescent side of the demarcation line is:

$$p_i^{\text{quiescent}} = P(\mathbf{H}|\mathbf{E}_i) = \frac{\sum_{j \in \text{Quiescent}} P(\mathbf{E}_i|\mathbf{E}_j)}{\sum_{j \in \text{All}} P(\mathbf{E}_i|\mathbf{E}_j)}$$

The marginal likelihood, $P(\mathbf{E})$, is used to ensure that the posterior probability, $P(\mathbf{E}|\mathbf{H})$, is normalized. By using Bayesian inference, we can evaluate the probability of each spaxel belonging to one side of the demarcation line, regardless of its signal-to-noise ratio.

Unfortunately, not all spaxels in the MaNGA data can be analyzed using the method described above. Only spaxels with valid $\text{H}\alpha$ and $[\text{O II}]$ equivalent width measurements can be used. To address this limitation, we created a mask based on $\text{H}\alpha$ and $[\text{O II}]$ measurements, which includes only those spaxels with both valid measurements. We refer to this mask as the ‘valid mask.’ The valid mask covers 91.88% of the area within the ellipse with a semi-major axis of $0.5 R_e$ and 89.90% of the area within $1.0 R_e$, which represents the maximum coverage achievable with

this method. We will refer to this mask and utilize its calculations in our subsequent analysis.

A significant limitation of this method lies in its inability to handle Seyfert-like spaxels effectively. The emission characteristic of Seyferts often results in spaxels positioning directly on the demarcation line. Furthermore, the nature of Seyfert-like emission is somewhat ambiguous. It is generally accepted that some degree of star formation is associated with Seyfert-like emission; however, the exact amount of star formation concealed beneath the Seyfert emission remains uncertain. This ambiguity complicates our ability to accurately estimate the star formation status of a spaxel undergoing Seyfert emissions. Thankfully, Seyferts are relatively rare within our sample. As such, they can be identified and considered as a distinct category of galaxies, separate from the conventional star-forming and quiescent binary classifications.

3.1.3 Seyfert regions of galaxies: modified BPT diagram

To identify Serferts, the usual method is to utilize multiple line ratios which require significant S/N on these lines. The S/N cuts would inevitably lead to the exclusion of those spaxels with weak lines. Although the WHAN diagram method proposed by [23] could be used to select Seyferts, and it only requires two strong lines, [N II] and $H\alpha$, it suffers from significant contamination. Thus, we only use the WHAN diagram method on those weak-line spaxels. For spaxels with strong enough lines, we utilize multiple line ratios for more clean identification of Seyferts.

The study by [41] proposes a new method to separate Seyfert regions and star-forming regions in galaxies, which improves upon traditional BPT diagrams. This new method involves projecting a three-dimensional line ratio space composed of [NII]/ $H\alpha$ [SII]/ $H\alpha$ and [OIII]/ $H\beta$ onto a two-dimensional surface. This projection provides a better separation of star-forming and AGN/LIER regions, as the model surfaces are viewed roughly in the edge-on direction. This enables a more precise evaluation of data points consistent with the models in all three line ratios. Moreover, the projection allows for clearer identification of composite objects.

Additionally, demarcation curves corresponding to a constant mixing ratio between star formation and AGN/LIER can be defined in this projection, which is an advantage over demarcation lines in traditional BPT diagrams. It is important to note that this method is not applicable to Seyfert regions, as they lie near the demarcation line, and therefore, require a separate classification.

For spaxels with all of $H\alpha$, $H\beta$, [N II] $\lambda 6583$, [S II] $\lambda\lambda 6716, 6731$, and [O III] $\lambda 5007$ detected above 3σ , we use the reprojected BPT diagram proposed by [41], and show them in the bottom panels of Figure 3.2. Using the same definition for P_1 and P_2 variables and the same method as in [41], we derived the 50-50 split demarcation line which is given by the equation below.

$$P_1 = -1.51P_2^2 - 0.355P_2 + 0.002 \quad (3.1)$$

where

$$P_1 = 0.63 \text{ N2} + 0.51 \text{ S2} + 0.59 \text{ R3} \quad (3.2)$$

$$P_2 = -0.63 \text{ N2} + 0.78 \text{ S2} \quad (3.3)$$

and

$$\text{N2} \equiv \log [\text{N II}] \lambda 6583 / \text{H}\alpha \quad (3.4)$$

$$\text{S2} \equiv \log [\text{S II}] \lambda \lambda 6716, 6731 / \text{H}\alpha \quad (3.5)$$

$$\text{R3} \equiv \log [\text{O III}] \lambda 5007 / \text{H}\alpha \quad (3.6)$$

This demarcation marks the surface in the line ratio space where AGN and SF contribute equally to $\text{H}\alpha$ flux. Just using this demarcation is not enough for Seyfert selection because some LIERs also distribute to the right of the demarcation. Thus, we further require the $\text{H}\alpha$ EW to be larger than 3\AA to select only Seyferts spaxels. Because most LIERs have $\text{H}\alpha$ EW lower than 3\AA , we can use this EW cut to select those that are more likely due to AGN. This is also the same threshold applied by [23] in the WHAN diagram to select Seyferts.

The modified BPT diagram relies on robust measurements of five emission lines: $\text{H}\alpha$, $[\text{N II}]$, $[\text{O III}]$, $\text{H}\beta$, and $[\text{S II}]$. However, some of these lines are relatively weak among galaxies, making it difficult to achieve satisfactory signal-to-noise (S/N) ratios. We can only apply this method on 67.7% of the spaxels. To complement the selection, we use the WHAN plot on the remaining spaxels since it only requires measurements of $\text{H}\alpha$ and $[\text{N II}]$. By selecting only spaxels with a signal-to-noise ratio greater than 3 for $\text{H}\alpha$ ew, we can retrieve an additional 12.3% of the spaxels, resulting in a total of 80.0% of the spaxels being considered. Any spaxels with $\text{H}\alpha$ and $[\text{N II}]$ having S/N ratios worse than 3 are not considered as potential AGN spaxels.

3.1.4 Summuray of our method

The process of identifying Seyfert galaxies is as follows: We first apply the modified BPT method to all applicable spaxels with the WHAN plot as a backup. Initially, the search for Seyfert AGN spaxels is limited to those within a $0.5 R_e$ aperture. Next, we divide the galaxy into three elliptical bins with semi-major axes within $0.3 R_e$, between $0.3 R_e$ and $0.4 R_e$, and between $0.4 R_e$ and $0.5 R_e$. We then calculate the fraction of Seyfert spaxels within these bins (or ellipse for the central bin). If any bin has a Seyfert fraction larger than 20%, we classify the galaxy as an ‘AGN’ galaxy. If the Seyfert fractions in all three bins are smaller than 20% but the largest fraction among them is greater than 5%, we classify the galaxy as a ‘weak-AGN’ galaxy. If all three bins have a Seyfert fraction lower than 5%, we classify the galaxy as a non-AGN galaxy. For both ‘AGN’ and ‘weak-AGN’ galaxies, we will extend the search for Seyfert spaxels beyond $0.5 R_e$ to the whole galaxy. We search for any Seyfert spaxels within a galaxy regardless of the relative position from the center once we identify the galaxy as ‘AGN’ or ‘weak-AGN’.

3.2 The radial quenching profile of galaxies

To study the radial profile of galaxies, we divide each galaxy into a series of concentric elliptical annuli based on its axis ratio (b/a) and effective radius (R_e). We draw ten concentric ellipses with a semi-major axis ranging from $0.3 R_e$ to $1.2 R_e$, spaced by $0.1 R_e$ between adjacent ones. This generates ten elliptical rings, including the central ellipse. The effective semi-major axis of these rings is determined by the formula $\theta = \sqrt{((r_{out}^2 + r_{in}^2)/2)}$, where r_{out} represents the length of the semi-major axis of the outer ellipse and r_{in} represents the length of the semi-major axis of the inner ellipse. This approach allows us to examine the properties and variations of galaxies across these concentric regions.

However, since our analysis is based on the ‘valid mask,’ which does not have 100% coverage, we make an exclusion criterion for rings with less than 50% of the spaxels being labeled as ‘valid.’ In order to be included in our direct measurements, galaxies must have both the innermost and outermost rings with over 50% of ‘valid’ spaxels. Any galaxies failing to meet this criterion are classified as ‘invalid’ and excluded from our direct analysis. However, we still aim to gain insight into these excluded galaxies through indirect means, which will be discussed in subsequent sections.

For galaxies that meet our criterion, we apply the method described in Section 3.1.4 and calculate a weighted average quiescent probability for each ring. The weight of each spaxel is based on the fraction of the spaxel area inside the corresponding ring since some spaxels have partial overlaps with a ring. We refer to each ring’s weighted average quiescent probability as its ‘quiescent fraction,’ which we plot against the radius of the ring, and then we have a profile. We name this profile after the ‘radial quiescent profile’ of a galaxy. Our study of galaxies will depend heavily on the behavior of this radial quiescent profile.

For weak-AGN galaxies we mentioned in Section 3.1.4, we exclude all Seyfert-like spaxels from the quiescent fraction calculation for weak-Seyfert galaxies; for AGN galaxies, we assume the Seyfert-like spaxels as star formation or quiescent, and calculate a quiescent profile independently, based on the assumptions above. Thus, we obtain a quiescent profile under the SF assumption and another quiescent profile under the quiescent assumption. We study the behavior of both these profiles and try to have a good understanding of AGN galaxies.

3.3 Sample definition and incompleteness correction

Before proceeding with our analysis of the radial quenching profile, it is crucial to ensure that our sample is always ‘valid’ and maintains volume completeness to the greatest extent possible. As discussed earlier, we ensure that our sample galaxies meet certain criteria, such as having their first and last ring being ‘valid’ and the innermost bins being well-resolved. However, applying these criteria results in the exclusion of a significant number of galaxies (1427 out of 4621) from the MaNGA primary sample, which is 33.7% of the sample. This exclusion could potentially introduce systematic bias into our analysis, and therefore, we need to make appropriate corrections to

recover the volume-limited sample as much as possible, accounting for the excluded galaxies and their weights.

3.3.1 Volume limitation of the MaNGA sample

The MaNGA survey selects galaxies based on their mass and redshift, using different criteria for Primary, Secondary, and Color-Enhanced samples. The parent catalog of MaNGA galaxies is an enhanced version of the NSA catalog ([13]), which is estimated to be 98.6% complete with $13 < r_{ab} < 17$. In this study, we only consider the galaxies in the Primary sample. For each galaxy, the MaNGA sample catalog provides a volume weight that should be applied to correct the sample to a volume-limited sample ([69]). We use this weight to correct the statistics in the rest of the paper to that in a volume-limited sample. However, due to the exclusion criteria described above, we still need to make corrections for the excluded galaxies to minimize any potential systematic bias in our conclusions.

3.3.2 Coverage and resolution limitations

In the selection of galaxies from our sample, we prioritized the capacity to resolve the central region and cover the outer region simultaneously. This principle has led to the establishment of certain selection criteria, corresponding to both a lower limit based on the effective radius (R_e) and an upper limit based on the coverage.

The lower limit corresponds to the ability to resolve the central region. Given that the average full-width at half maximum (FWHM) for MaNGA is approximately 2.5 arc seconds, it's crucial that our central bin ($0.3 R_e$) exceeds this value. Thus, for galaxies with an effective radius smaller than 4.17 arc seconds, our innermost bin already falls below the average FWHM. Such galaxies are excluded from our sample due to potential resolution limitations, preventing accurate analysis of their central regions.

Simultaneously, we aimed to ensure sufficient coverage of the outer region of the galaxies. This led us to establish an upper limit criterion. We require that at least 50% of our outermost bin (falling within $1.1 R_e$ to $1.2 R_e$) is covered. Galaxies that do not meet this criterion, meaning those with less than 50% coverage in the outermost bin, are likewise excluded from our sample.

This careful selection process, taking into account both the central resolution and outer coverage of the galaxies, allows us to achieve a sample that can provide a robust and comprehensive analysis of the phenomena we wish to explore.

3.3.3 Correction for those excluded galaxies

To correct for the galaxies excluded from our sample, we assume that their quiescent fraction profiles are statistically similar to galaxies with similar effective radii, colors, and i -band absolute magnitudes that are included in our sample. We search for galaxies with similar properties by requiring the differences in their $g-r$ colors and i -band absolute magnitudes to be less than 0.1 mags and their effective radii to have a fractional difference less than 10% if larger than 5 kpcs, or less than 0.5 kpcs if

smaller. We then increase the volume weights of the included galaxies to account for the excluded galaxies. Specifically, for each excluded galaxy, we search for N included galaxies with similar properties and increase their volume weights by p/N , where p is the volume weight of the excluded galaxy. This correction ensures that the sum of volume weights between the original Primary sample and the sample we consider remains conserved. For excluded galaxies with no similar neighbors, we cannot correct them. After making these weight corrections, we consider 4267 galaxies out of the 4621 Primary sample galaxies and achieve a volume-limited completeness of 90.1%.

3.4 Classification of galaxies

3.4.1 Normal galaxies

Normal galaxies are defined as those that satisfy both our selection criteria and the AGN test, indicating that they are non-Seyfert galaxies with sufficient coverage and resolution. For these galaxies, we can apply the method described in Section 3.2 without encountering any issues.

With our method established, we can now delve into our analysis of the radial quenching profiles of the galaxies under examination. These profiles provide valuable insights into the processes governing the cessation of star formation in galaxies and allow us to explore how the probability of a galaxy being quiescent changes with increasing distance from the center. By setting a threshold value of 50%, we can classify normal galaxies into three different types based on the behavior of their quiescent profile. This classification scheme can be further refined into six distinct subtypes, allowing us to investigate the variations in the transition from active star formation to quiescence among galaxies with different properties.

Uniform galaxies, UGs

We define ‘uniform galaxies’ as those with a uniform classification throughout the evaluation range ($0.3 R_e$ - $1.2 R_e$), i.e., they are either star-forming or quiescent throughout.

- Uniformly star-forming galaxies, abbreviated as ‘SF,’ are those galaxies with a quiescent fraction below 50% in all radial bins.
- Uniformly quiescent galaxies, abbreviated as ‘Q,’ are those galaxies with a quiescent fraction above 50% in all radial bins.

Monotonic-transition galaxies, MTGs

We define a galaxy as a ‘monotonic-transition galaxy’ if its quiescent fraction profile crosses the 50% threshold once and only once between $0.3 R_e$ and $1.2 R_e$.

- Central-quiescent galaxies, abbreviated as ‘C-Q,’ are defined to be those with a quiescent center and a star-forming outskirt. For those galaxies, there is a

downward intersection. The quiescent fraction starts above 50% at $0.3 R_e$ and ends below 50% at $1.2 R_e$.

- Central-star-forming galaxies, abbreviated as ‘C-SF’, are defined to be those galaxies with a star-forming center and a quiescent outskirts. For those galaxies, there is an upward intersection. They have a star-forming core and quiescent outskirts. The plot of these galaxies would be below 50% in the center and then rise above 50% in a larger radius.

Non-monotonic-transition galaxies, non-MTGs

The spatial transition between star-forming regions and quiescent regions is not always monotonic. There could be two or more transitions in different directions at a few different radii within a galaxy. These cases are listed as ‘non-monotonic-transition galaxies,’ which exist but rarely in our sample. We are only able to make some empirical guesses on this sub-type.

- Quiescent-ring galaxies, abbreviated as ‘Q-Ring,’ are galaxies with upward and downward intersections. If a galaxy has a downward intersection at a smaller radius than its upward intersection, it has a quiescent core, a star-forming ring, and a quiescent outskirts.
- Star-forming ring galaxies, abbreviated as ‘SF-Ring,’ are galaxies with a star-forming core, a quiescent ring, and then a star-forming outskirts, meaning they have an upward followed by a downward intersection. The curve on the plot for this kind of galaxy will increase from below 50% to above 50% and then drop below 50%.

3.4.2 AGN galaxies and weak-AGN galaxies

Seyfert galaxies, which are defined as AGNs or weak-AGNs in our sample, offer valuable opportunities to study AGN feedback. However, due to their distinct nature, we have chosen to discuss them separately from the normal galaxies. For weak-AGN galaxies, we can mask off the AGN spaxels and treat them as normal galaxies, enabling us to analyze them using the same methods as the normal galaxy sample. On the other hand, for AGN galaxies, we follow the procedures outlined in Section 3.1.4 and study their quiescent profiles under both the SF assumption and the Q assumption. This allows us to explore the impact of the AGN on the star formation and quiescence within these galaxies.

3.4.3 Excluded galaxies

While the methodology described above allows us to recover a significant number of galaxies, there is a subset of galaxies that cannot be effectively analyzed due to their small physical size, low mass, and red color. These galaxies form a distinct category

that necessitates separate consideration. While we are unable to apply our method directly to these galaxies, we can still examine their fundamental properties to gain insights into their nature. In the following sections, we will provide an overview of the available information and discuss the implications for these galaxies.

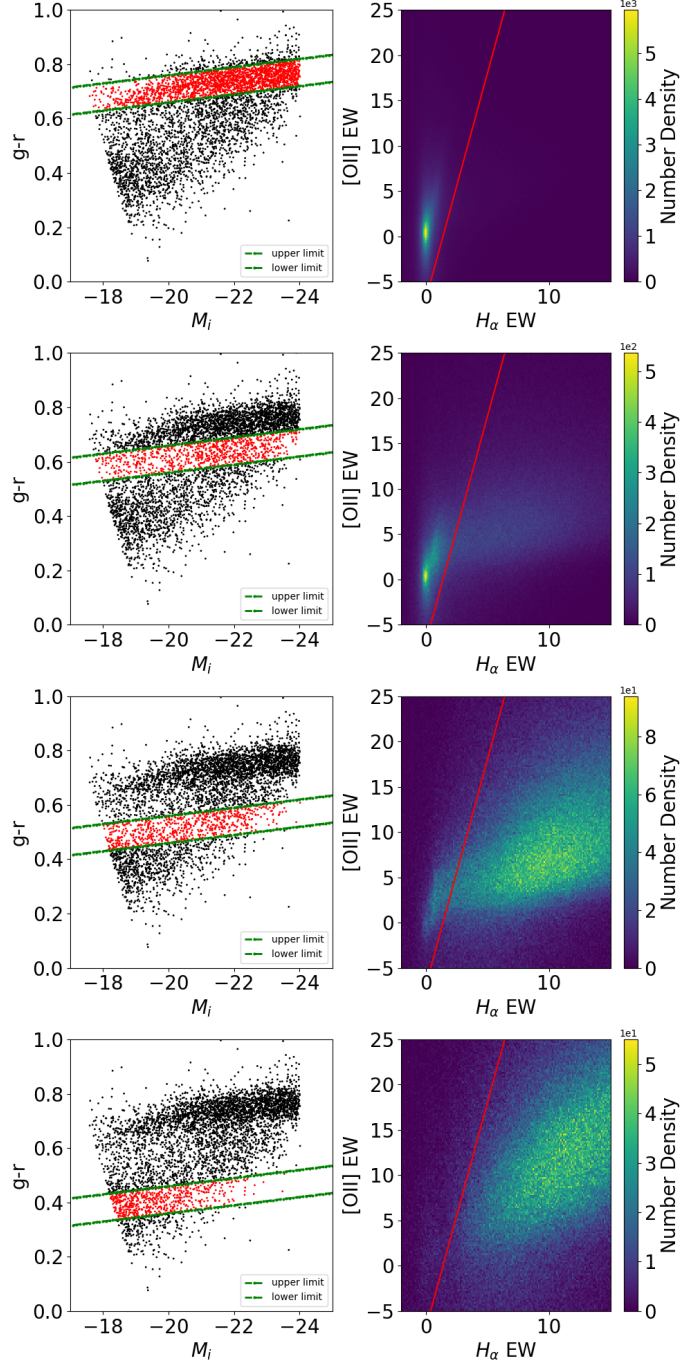


Figure 3.1: This figure displays the H_α vs. $[O II]$ equivalent width histogram for galaxies with different colors and magnitudes. The left panels depict the color-magnitude plot with $g-r$ color and i -band absolute magnitude for the overall galaxy, while the right panels show the H_α vs. $[O II]$ equivalent width histogram of spaxels that belong to the red highlighted galaxies on the left panels. The blue galaxies contain more star-forming regions, while the red galaxies contain fewer star-forming regions. The red demarcation line proposed by Y06 works appropriately in separating quiescent and star-forming regions.

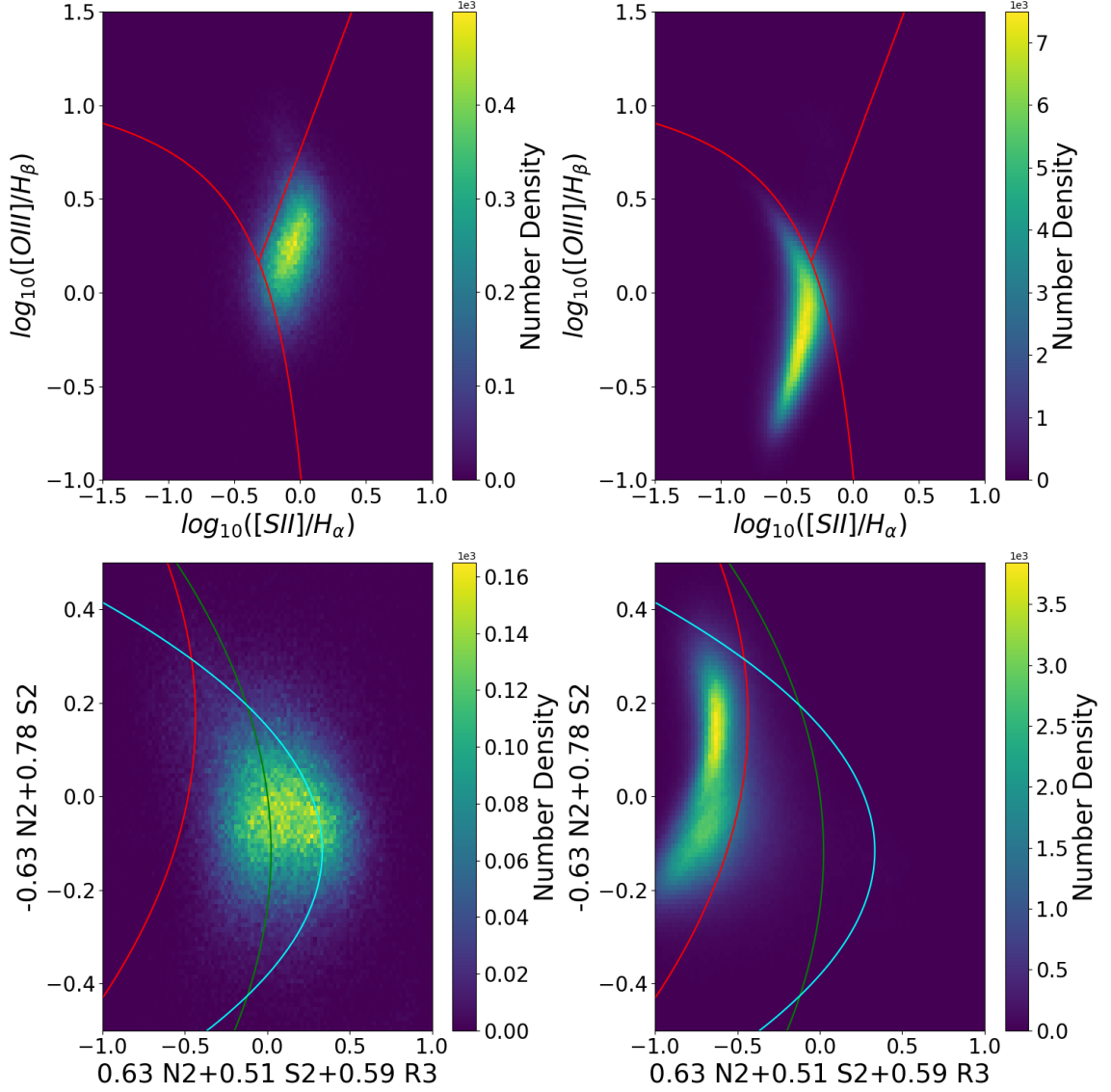


Figure 3.2: This figure displays the spatial distribution of quiescent and star-forming regions in galaxies, determined by their $H\alpha$ and $[O II]$ equivalent widths on both traditional and re-projected BPT diagrams ([41]). The left two panels illustrate the quiescent regions, while the right two panels depict the star-forming regions. The upper panels show the traditional BPT diagrams, with red demarcation lines, while the lower panels exhibit the re-projected BPT diagram, with the red, green, and blue lines indicating a 10%, 50%, and 90% star-forming composition model grid, respectively. The data correspond to all MaNGA galaxies with a signal-to-noise ratio greater than 3 for all the emission lines used in this study.

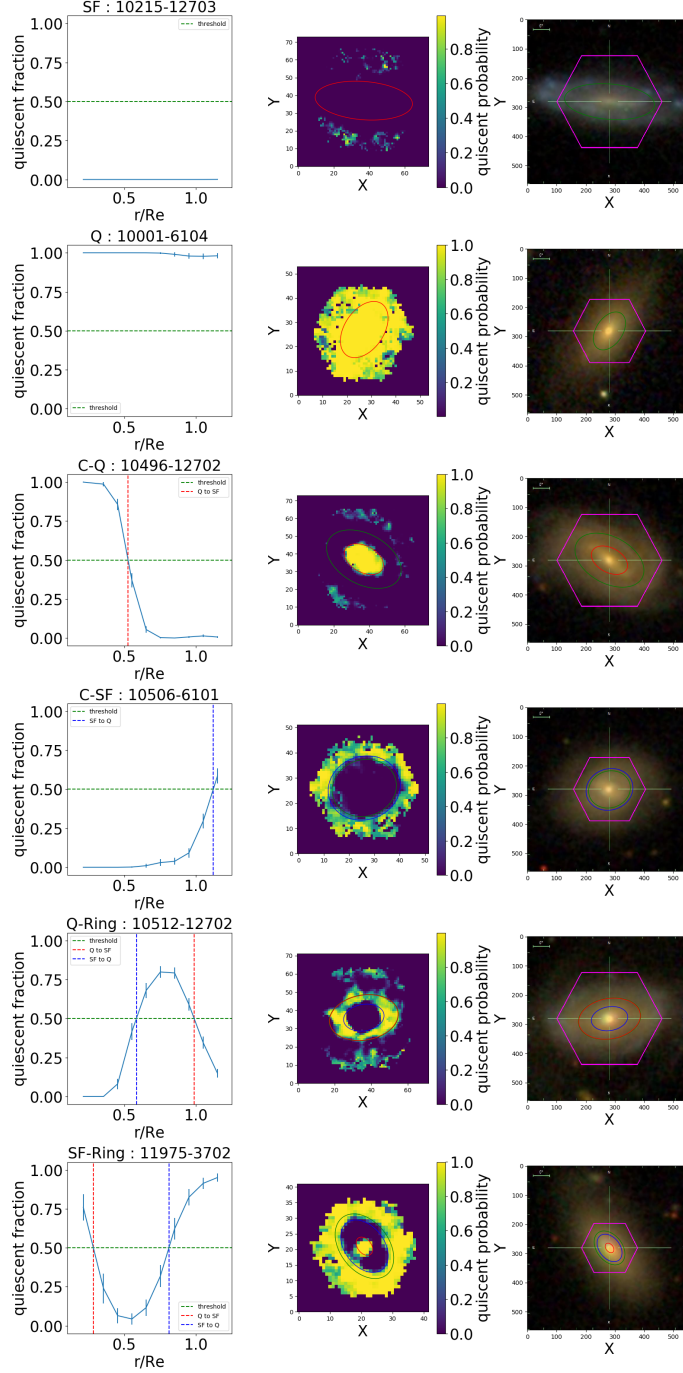


Figure 3.3: This plot displays examples of six different subtypes of galaxies. The left panels show the quiescent radial profile, the middle panels depict the quiescent probability distribution, and the right panel shows an optical image of the galaxy with indicators for the effective radius (R_e), star-forming regions (SF), and transition radius (if applicable). Each subtype is represented by one galaxy selected as a representative example. The plate-IFU number for each galaxy are indicated in the plot. The six subtypes shown, from top to bottom, are: quiescent (Q), star-forming (SF), composite quiescent (C-Q), composite star-forming (C-SF), quiescent with a ring (Q-Ring), and star-forming with a ring (SF-Ring).

Chapter 4 Properties of galaxies of different types

In Section 3.3, we described how we make a selection of galaxies in the MaNGA primary sample. Despite our effort, we must exclude galaxies with improper coverage/resolution. In this section, we will discuss in detail all the galaxies, including the ones we have to exclude.

4.1 Properties of normal galaxies

The term ‘selected galaxies’ stands for galaxies that meet our selection criteria and are not defined as a ‘Seyfert’ AGN. Those galaxies have proper sizes and redshifts and presumably weak black-hole activities. We can apply our analysis method to these galaxies, thus assigning a ‘type’ for them. We can see the general behavior, such as the C-M diagram of galaxies of different types. These methods and the types generated are described in Section 3.4.

4.1.1 Color-magnitude distribution and color mass distribution of different types

We made a color-magnitude diagram of selected galaxies and plotted the galaxies as a relative number to the total sample. From Figure 4.1, we can see that the quiescent sequence is quite tight. The star-forming sequence is more spread than the quiescent sequence, and some lie in the red sequence. We consider those galaxies dusty star-forming galaxies; thus, they are red. That is a good thing to see. We can tell that our method of separating star-forming and quiescent is effective.

Non-monotonic-transition galaxies are rare compared to uniform galaxies (SF and Q galaxies). Most of them are found in the ‘green valley,’ which indicates that they may be served as a transition phase between SF and Q galaxies. The central-quiescent galaxies have a higher stellar mass, while central-star-forming galaxies are relatively less massive. This uneven distribution is an interesting phenomenon, which worth some further investigation.

4.2 Properties of AGN and weak-AGN galaxies

To ensure that we could accurately classify spaxels in our analysis, we decide to study AGNs separately. This was because when an AGN dominates a pixel, it becomes difficult to determine whether there is underlying star formation or not. Figure 4.2 displays the distribution of AGNs overlaid on non-AGN galaxies. We observed that AGNs occur more frequently in the green valley and have an intermediate mass. This finding is consistent with previous studies such as [61] and [63]. The information provided by this figure is crucial for understanding the role of AGNs in galaxy evolution and the potential impact they may have on the star formation process in galaxies.

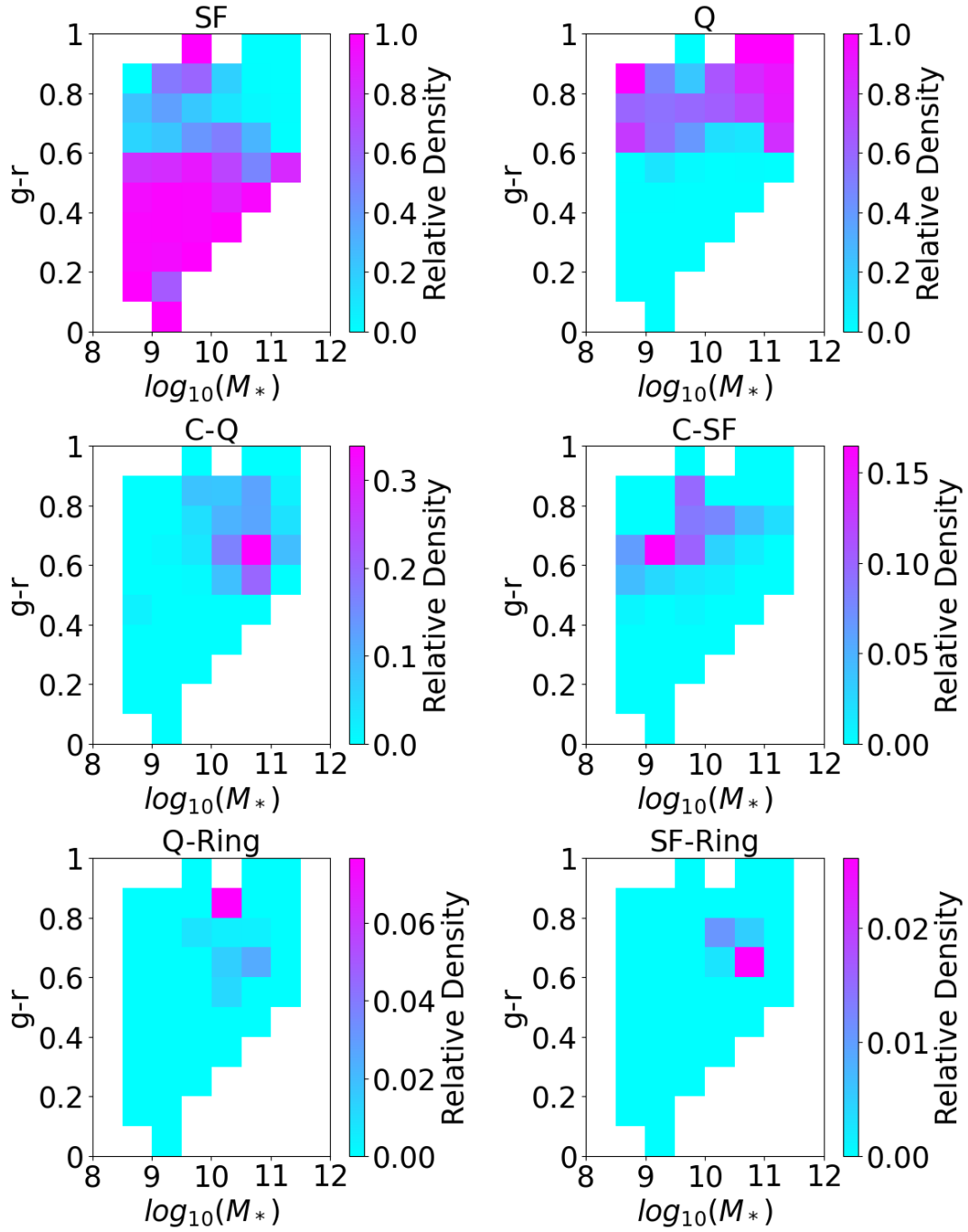


Figure 4.1: This figure illustrates the relative density of six different subtypes on a color-mass diagram. Each subplot is labeled with the corresponding subtype, and the axes are labeled accordingly. The color bar indicates the relative density, which is calculated by dividing the number of galaxies of a particular subtype by the total number of galaxies within a specific area.

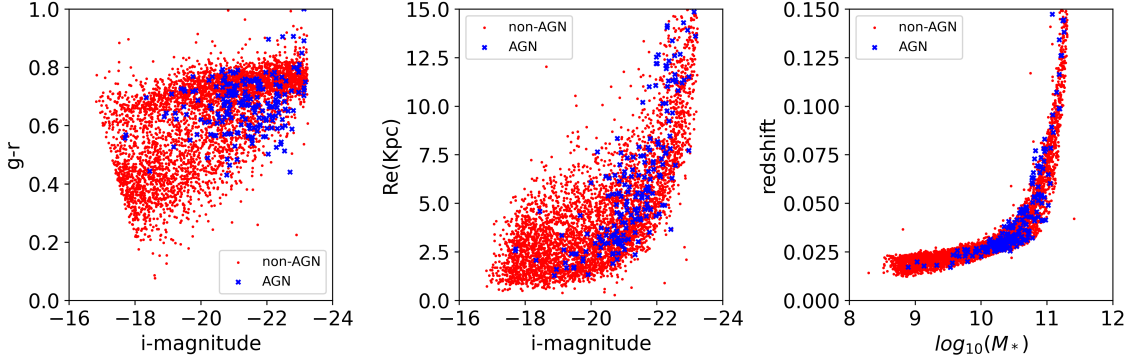


Figure 4.2: This figure illustrates the effect of Seyfert-AGN selection on our sample. The dots on the panels are color-coded as red and blue, representing non-AGN and AGN, respectively. The left panel shows the $g-r$ color versus the SDSS i -band magnitude, the central panel shows the effective physical radius versus the i -band magnitude, and the right panel shows the redshift versus the total stellar mass. The AGNs in our sample appear to occur within a relatively narrow range in the parameter space. Most of the AGNs have a mass between $10^{9.5}$ and 10^{11} solar masses and a $g-r$ color between 0.5 and 0.8, suggesting intermediate mass green-valley galaxies. This information is crucial for understanding the role of AGNs in galaxy evolution and the potential impact they may have on the star formation process in galaxies.

4.3 Properties of excluded galaxies

Despite our efforts to maintain mass completeness in our analysis, not all galaxies in the MaNGA MPL-11 sample satisfied the selection criteria of our method. As a result, we had to exclude a certain number of galaxies from our analysis due to a coverage/resolution problem. These galaxies were either too large to be fully covered or too small to be properly resolved. In our analysis, we set a minimum effective radius of 1.25 arc-seconds to ensure that we could resolve the galaxies. We also aimed to ensure that we had at least 50% of the spaxels in the outermost bin. However, despite these efforts, there were still some galaxies that were excluded due to coverage or resolution limitations. While these exclusions reduce the overall sample size, they are necessary to ensure the validity of our analysis and the accuracy of our results.

Figure 4.3 provides information about the galaxies that were excluded from our analysis due to resolution and coverage limits. The excluded galaxies, represented as red and blue dots in the figure, form two sets due to different exclusion reasons. Red dots correspond to galaxies with a red color, small physical effective radius, and low mass that were excluded due to the resolution limit (labeled as exclusion 2 in the panels). These galaxies typically lie on the red sequence in the left panel, the lower sequence in the middle panel, and the low-mass end in the third panel. Their red color, small physical size, and medium-to-low stellar mass suggest a compact core. Thus, we infer that these galaxies are likely to be compact, low-mass quiescent galaxies.

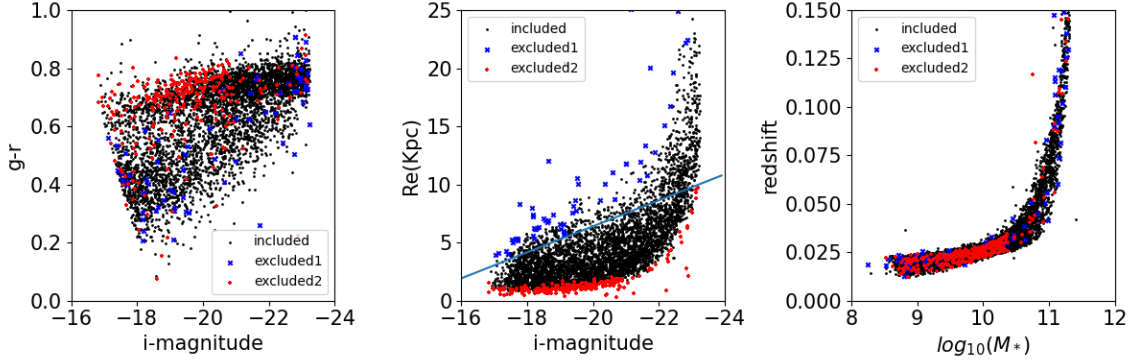


Figure 4.3: This figure demonstrates the effect of coverage and resolution selection on the data. The dots on the panels are color-coded as black, blue, and red, representing the ‘included’ galaxies, exclusion 1, and exclusion 2, respectively. Exclusion 1 is due to incomplete coverage, while exclusion 2 is due to insufficient resolution. The left panel shows the $g-r$ color versus the SDSS i -band magnitude, the central panel shows the effective physical radius versus the i -band magnitude, and the right panel shows the redshift versus the total stellar mass. The primary reason for exclusion is the physical size of the galaxies. Some galaxies are too large to be fully covered, while others are too small to be resolved. Exclusion 2 galaxies make up $8.3\% \pm 0.4\%$ of the sample, while exclusion 1 galaxies make up $1.7\% \pm 0.2\%$.

The other set of galaxies are blue, large in physical size, and massive and were excluded due to the coverage limit (labeled as exclusion 1 in the panels). They are located on the blue cloud in the left panel, an upper boundary in the middle panel, and a high-mass end in the right panel. Their blue color, large physical size, and medium-to-low stellar mass suggest a less-compact core. Therefore, we infer that these galaxies are likely to be diffused star-forming galaxies.

However, due to the lack of sufficient information on either exclusion 1 or exclusion 2 galaxies, we can only make basic inferences about their properties.

4.4 Statics of types of galaxies

Our statistical analysis of different types of galaxies in a volume-limited sample is presented in three tables. Table 4.1 provides an overview of all galaxies in the sample, including excluded galaxies and AGN. We observed that star-forming (SF) galaxies dominate the sample, accounting for the majority of the total weight. Quiescent galaxies make up approximately 20% of the total weight, while monotonic-transition galaxies (C-Q and C-SF) take up approximately 8%. AGN galaxies make up 2% of the total weight, while excluded galaxies account for 10%. The majority of the excluded galaxies are low-mass red galaxies. Non-monotonic-transition galaxies are rare and account for less than 1% of the total weight.

Table 4.2 shows a significant difference in the distribution of types between non-AGN and weak-AGN galaxies. For weak-AGN galaxies, we masked off the AGN

Table 4.1: This table provides information on the frequencies of different sub-types in a volume-limited sample that includes AGN and excluded galaxies. The values and errors are presented as percentages, and the errors are derived by assuming a Poisson distribution.

SF	60.85 ± 0.96
Q	19.01 ± 0.55
C-SF	3.89 ± 0.27
C-Q	3.56 ± 0.26
SF-Ring	0.14 ± 0.05
Q-Ring	0.36 ± 0.08
Seyfert	2.28 ± 0.23
Exclusion1	1.65 ± 0.18
Exclusion2	8.24 ± 0.39

Table 4.2: This table compares the frequencies of different sub-types in a volume-limited sample between non-AGN and weak-AGN galaxies. The values and errors are presented as percentages, and the errors are derived by assuming a binomial distribution.

	SF	Q	C-SF	C-Q	SF-Ring	Q-Ring
non-AGN	67.5 ± 1.0	21.1 ± 0.6	4.3 ± 0.3	4.0 ± 0.3	0.2 ± 0.1	0.4 ± 0.1
weak-AGN	64.7 ± 4.0	1.1 ± 1.0	21.5 ± 3.5	9.4 ± 2.5	0.0 ± 0.0	3.3 ± 1.5

spaxels and performed calculations based on the remaining spaxels to define a ‘type’ for them. We observed that monotonic-transition galaxies account for a much larger fraction of weight among weak-AGN galaxies than they do among non-AGN galaxies. This suggests a connection between AGN activity and the change in star formation status.

These tables provide valuable insights into the types of galaxies in our sample, highlighting the dominance of SF galaxies and the importance of excluding AGN to ensure accurate classification. The significant difference in type distribution between non-AGN and weak-AGN galaxies also suggests a potential link between AGN activity and star formation status.

Chapter 5 Monotonic-transition galaxies

The group of monotonic-transition galaxies is of particular interest to us, as they exhibit a mixture of both star-forming and quiescent characteristics. These galaxies could potentially represent a transition phase between star-forming and quiescent galaxies, and we aim to study this group in detail to gain a better understanding of their role in galaxy evolution. To uncover clues about their properties and behavior, we will compare monotonic-transition galaxies with uniform galaxies in our analysis.

5.1 The transition radius

5.1.1 R_t versus stellar mass, $g-r$ color, and concentration

We defined the transition radius for monotonic-transition galaxies as the point where the quiescent profile crossed the 50% threshold. To understand the implications of the transition radius, we compared it to various overall measurements and derived properties of galaxies. Figure 5.1 illustrates our findings.

Our analysis revealed that there was little correlation between the transition radius and i -band absolute magnitude, total stellar mass, and the Sersic index. These properties did not exhibit any significant trends or patterns with respect to the transition radius.

However, we did observe a notable relationship between the $g-r$ color and the transition radius. For central-quiescent (C-Q) galaxies, a larger transition radius was associated with a redder color. Conversely, for central-star-forming (C-SF) galaxies, a larger transition radius was linked to a bluer color. This observation aligns with our expectations, as star-forming regions tend to exhibit bluer colors. Therefore, galaxies with a larger star-forming region tend to have a bluer overall color.

To further investigate the nature of the central and outer regions of monotonic-transition galaxies, we calculated the specific star formation rate (sSFR) for three different regions of galaxies: the core (region within $0.3 R_e$), intermediate ring (the region between $0.6 R_e$ and $0.7 R_e$), and the outskirts (the region between $1.0 R_e$ and $1.2 R_e$). We calculated the star formation rate from $H\alpha$ emission using the formula provided by [43] (Kennicutt formula hereafter). and obtained the stellar mass estimates from PIPE 3D. However, it is worth noting that the Kennicutt formula only applies to star-forming regions, which are present in the center of C-SF galaxies and the outskirts of C-Q galaxies.

Figure 5.2 presents the sSFR in these regions. From this figure, the trend between sSFR and the transition radius is quite apparent. The right panel shows the relationship between the transition radius and sSFR of the central part of central-star-forming galaxies; there is a positive correlation between the sSFR and the transition radius. That is, the larger the center star-forming area is, the stronger the central star formation is. The inverse trend can be observed in the left panel, which means that the larger the quiescent center area is, the weaker the outer star formation is.

For quiescent regions, this measurement of ‘sSFR’ should not be interpreted as star formation, but it is still meaningful as it is based on the $H\alpha$ strength, which must reflect the strength of some physical process. Please refer to the appendix for more information on this measurement in other regions of the galaxies.

5.2 Stellar mass dependence of the distribution of C-Q and C-SF galaxies

The distribution of the total stellar mass of central-quiescent and central-star-forming galaxies in Figure 4.1 reveals a significant difference between the two types. Central-star-forming galaxies have a smaller total stellar mass, while central-quiescent galaxies have a larger total stellar mass. This difference is also evident in the i -band magnitude, which is closely related to stellar mass. The transition point is around $\log_{10}(M_*/M_\odot) = 10.2$. Above this mass, the transition galaxies are dominated by central-quiescent galaxies, while below this mass, the transition galaxies are dominated by central-star-forming galaxies.

Figure 5.3 provides a more detailed analysis of this phenomenon by binning all monotonic-transition galaxies into four mass bins and showing the fractions of the two categories out of all monotonic-transition galaxies. The results show that monotonic-transition galaxies are predominantly central-star-forming at low masses and central-quiescent at high masses. This finding suggests that galaxies with different masses follow different transition paths.

5.3 Σ_1 comparisons

To investigate the potential connection between monotonic-transition galaxies (MTGs) and uniform galaxies (UGs), we examine their Σ_1 values. The Σ_1 value represents the average mass surface density within the central 1 kpc radius of a galaxy. Previous studies have shown that the Σ_1 values of star-forming and quiescent galaxies exhibit significant differences ([31]). By comparing the Σ_1 values of MTGs with those of star-forming and quiescent galaxies, we aim to gain insights into the relationship between MTGs and UGs.

To analyze the distribution of Σ_1 , we construct comparison samples of star-forming and quiescent galaxies that are representative of the central-star-forming (C-SF) or central-quiescent (C-Q) galaxies, respectively. Rather than selecting specific subsamples, we assign weights to each galaxy during the statistical analysis. The weighting procedure ensures that the stellar mass distribution of the comparison samples matches that of the corresponding MTG sample.

The weight assignment process involves binning both the MTG sample and the comparison sample by stellar mass. As the number of star-forming galaxies typically exceeds the number of C-SF galaxies within each bin, we apply weights to the star-forming galaxies to achieve a matching distribution. In each stellar mass bin, we calculate the ratio of the number of C-SF galaxies to the number of star-forming galaxies and assign this ratio as weights to the star-forming galaxies. These weights are then used to construct the Σ_1 distribution for the star-forming galaxies. The process

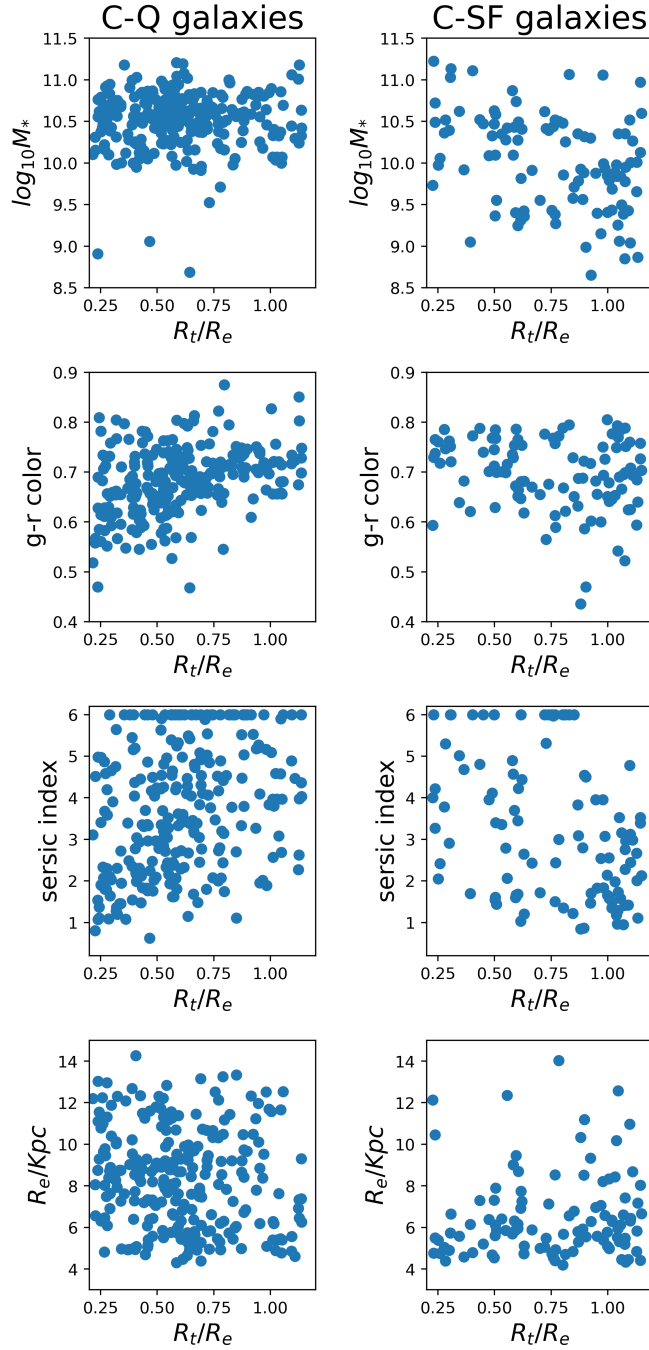


Figure 5.1: The left panels display the results for C-Q galaxies, while the right panels correspond to C-SF galaxies. The x-axis represents the transition radius, measured in units of R_e , while the y-axis corresponds to different galaxy properties. The first row of panels depicts the total stellar mass, the second row shows the $g-r$ color, the third row displays the Sersic index obtained from the NSA catalog, and the fourth row represents R_e in kiloparsecs (kpc). No significant correlation is observed in any of these panels.

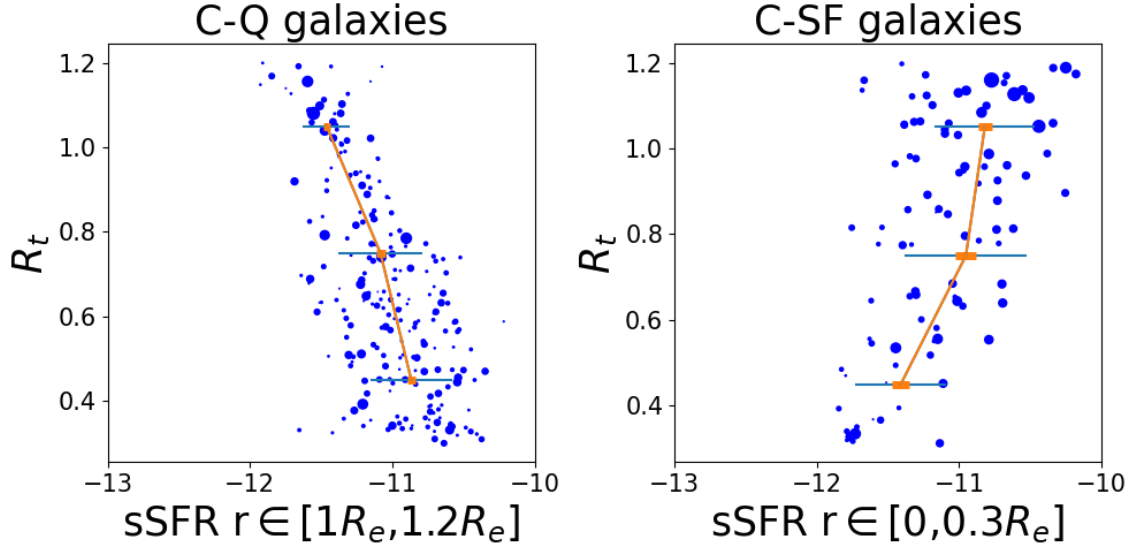


Figure 5.2: This figure shows the relationship between the transition radius and the specific star-forming rate at different relative radii. The left panel displays data for the outskirts (regions between $1.0 R_e$ and $1.2 R_e$) of central-quiescent galaxies, while the right panels display data for the central regions (regions within $0.3 R_e$) of central-star-forming galaxies. The data is binned into three bins based on the transition radius, allowing for an evaluation of the difference between galaxies. The central value of each bin is represented by the weighted median value, the long thin blue bar shows the scatter of this median, and the short thick orange bar represents the standard error of this median. For more information on the specific method of calculating these values, please see the appendix.

is repeated for the comparison of three samples, with the stellar mass distributions of the larger samples (usually star-forming and quiescent galaxies) being matched to the sample with the smallest number of galaxies (one of the transition galaxy types). By using these weights, we compute the weighted averages of the Σ_1 values for each sample, enabling direct comparisons. This approach allows us to examine the similarities and differences in the Σ_1 distributions among MTGs, star-forming galaxies, and quiescent galaxies.

In Figure 5.4, we present a comparison of Σ_1 between monotonically transitioning galaxies and stellar-mass-matched representations of star-forming galaxies and quiescent galaxies. We name these representations after ‘the comparison samples.’ The top-left panel illustrates the distribution of Σ_1 for central-star-forming galaxies and the comparison sample. The right panel compares the mean values of the distributions along with their uncertainties.

The analysis reveals a significant difference in mean central mass densities between central-star-forming galaxies and the star-forming galaxies in the control sample, with a 4.4σ level of significance. The K-S test yields a p value of 0.003, indicating a mere 0.3% probability of observing such a significant difference if the two samples

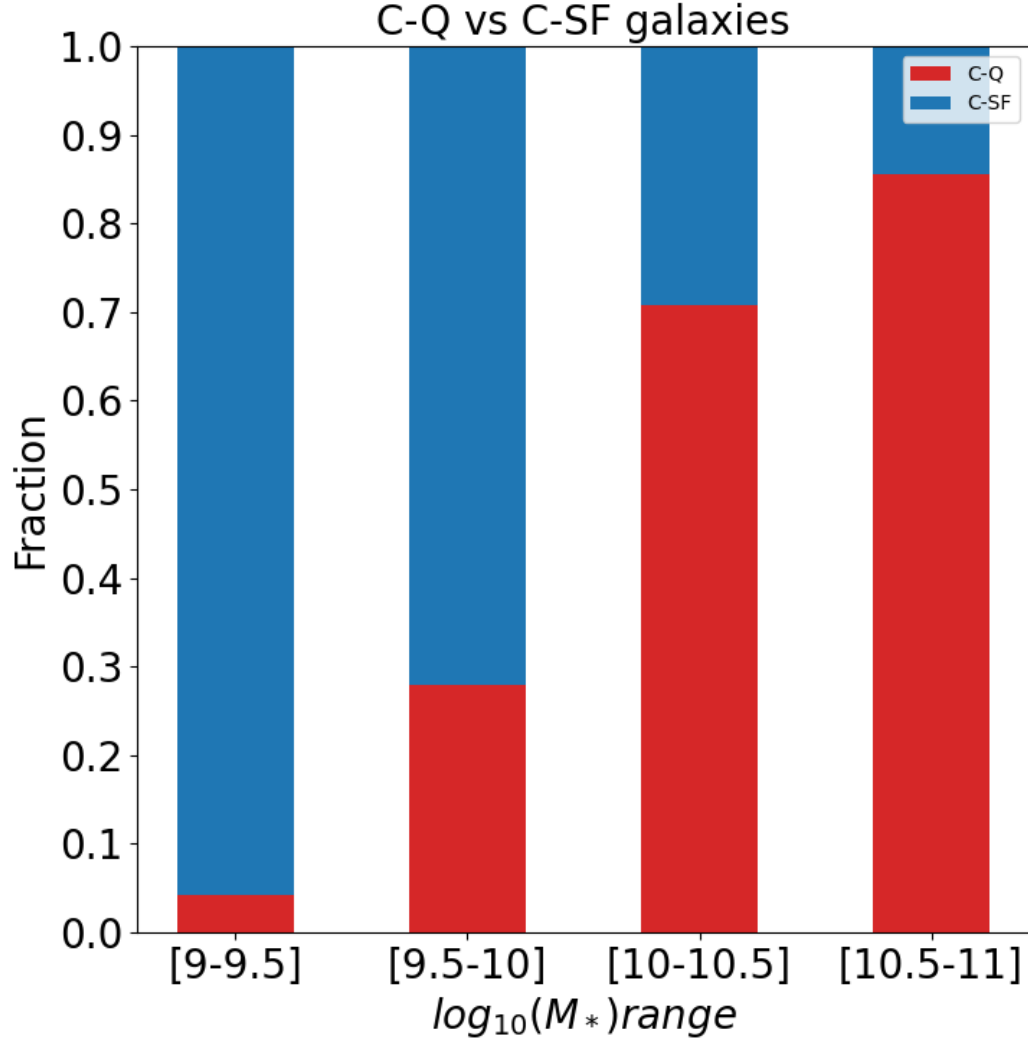


Figure 5.3: This figure shows the relative fraction of central-quiescent(C-Q) and central-star-forming(C-SF) galaxies in four different mass bins. The mass bins are marked on the x-axis in units of $\log_{10}(M_*/M_\odot)$. The y-axis represents the fraction of each type of galaxy within each mass bin. We observe that the fraction of central-quiescent galaxies increases with mass, while the fraction of central-star-forming galaxies decreases with mass. This phenomenon indicates that galaxies with different masses follow different transition paths.

originated from the same parent population. In other words, the K-S test rejects the null hypothesis that star-forming galaxies and central-star-forming galaxies share the same parent population.

When comparing the central-star-forming (C-SF) galaxies to quiescent (Q) galaxies, we observe a smaller difference in Σ_1 with a significance level of only about 1.6σ . The K-S test results in a p value of 0.557, suggesting that there is no significant evidence to reject the null hypothesis. These findings indicate that star-forming galaxies are unlikely to be the parent population of central-star-forming galaxies, but quiescent galaxies would be a potential parent population.

In contrast to central-star-forming galaxies, central-quiescent galaxies exhibit significantly different average Σ_1 values compared to both star-forming and quiescent galaxies. The mean Σ_1 value of C-Q galaxies differ from star-forming galaxies by 5.1σ and from quiescent galaxies by 3.6σ . The K-S tests for both comparisons reject the null hypothesis, indicating that C-Q galaxies have a distinct central stellar mass density distribution from the other two populations.

In addition to the overall mean value difference, we examined the distribution of Σ_1 as a function of stellar mass for different populations, as shown in Figures 5.5 and 5.6. We found that the difference in Σ_1 between star-forming galaxies and quiescent galaxies is not significant until the total stellar mass reaches above 9.2 in $\log_{10}(M_*/M_\odot)$. The value of Σ_1 then plateaus when the total stellar mass reaches around 10.7 due to the spatial resolution limit, which is demonstrated below. The difference between C-SF and Q galaxies is relatively small at all masses. However, the difference between C-SF and SF galaxies is significant at all masses above 9.2. For C-Q galaxies, their central mass density is intermediate between quiescent and star-forming galaxies at all masses where there are sufficient statistics. However, it seems to shift from being more similar to quiescent at low masses ($\log_{10}(M_*/M_\odot) \sim 9.8$) to more similar to star-forming galaxies at high masses ($\log_{10}(M_*/M_\odot) \sim 10.7$). The difference between C-Q galaxies and the two uniform populations is significant.

In our study, we have observed that the Σ_1 of C-Q galaxies exhibits a threshold at approximately 9.5 in our sample, which coincides with the Σ_1 where C-Q galaxies leave the quiescent sequence. This observation suggests an upper limit of Σ_1 . Beyond this threshold, galaxies will quench their center and cannot further increase their Σ_1 through star formation.

Our findings suggest that the central stellar mass density of C-SF galaxies is very similar to that of quiescent galaxies but differs significantly from that of star-forming galaxies. In contrast, the Σ_1 of C-Q galaxies lies between that of quiescent and star-forming galaxies. Overall, these results provide compelling evidence that central-star-forming and quiescent galaxies have different Σ_1 distributions, which highlights the importance of considering central mass density when studying galaxy evolution.

5.4 z -band concentration comparisons

Concentration, quantified by the ratio of the radii containing 90% and 50% of a galaxy's light (R_{90}/R_{50}), provides insights into the distribution of brightness in the central and outer regions of a galaxy. Higher concentration values indicate a denser

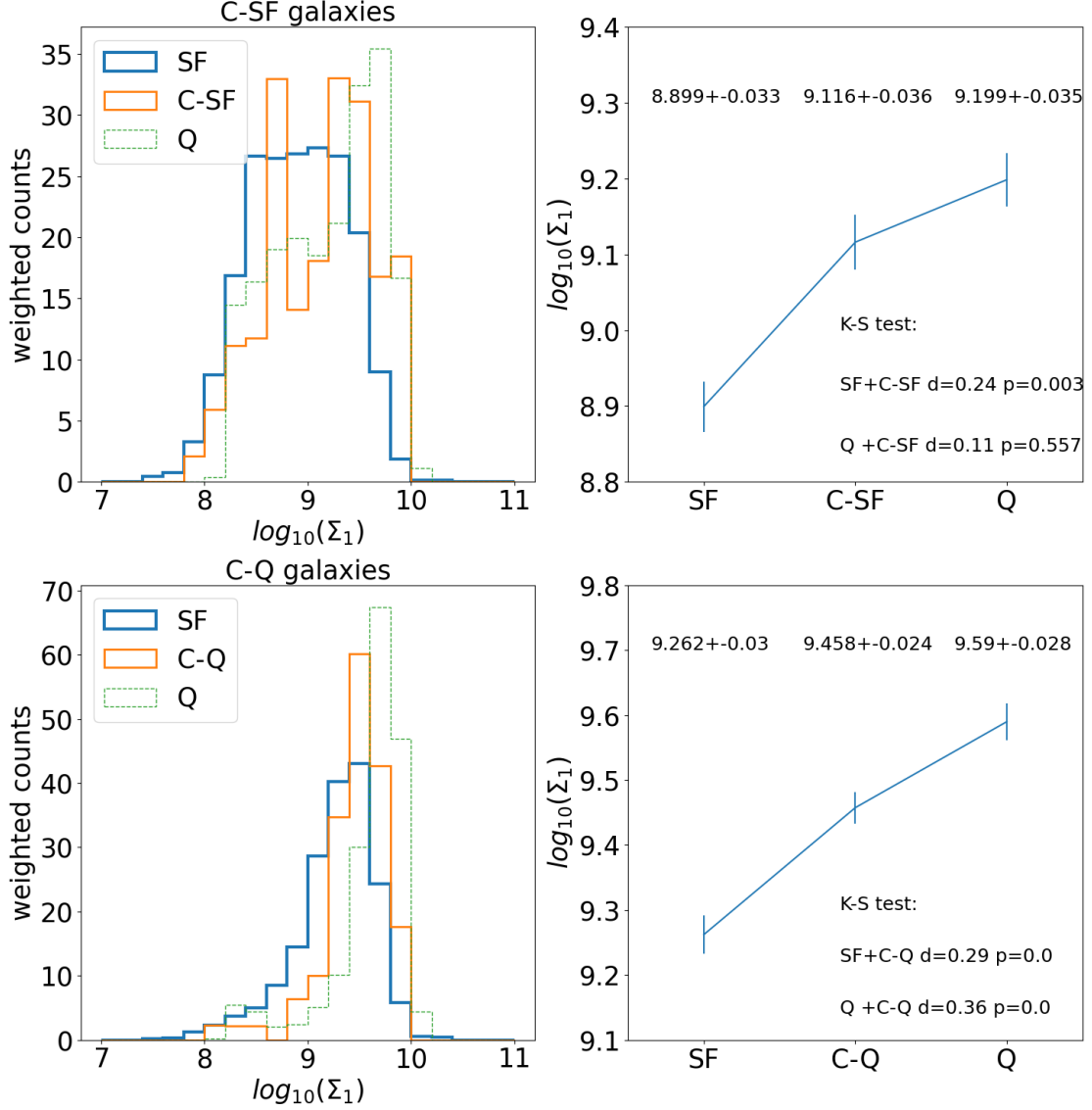


Figure 5.4: This figure illustrates the differences in Σ_1 between monotonic-transition galaxies and comparison samples. The top-left panel displays the histogram of $\log_{10} \Sigma_1$, while the top-right panel displays the mean value with corresponding error bars, along with the K-S test results between C-SF galaxies and star-forming/quiescent galaxies. The comparison samples were created by selecting star-forming and quiescent galaxies with the same mass distribution as C-SF/C-Q galaxies and weighting them to ensure their total stellar mass distribution is identical. The upper panels correspond to C-SF galaxies, and the lower panels correspond to C-Q galaxies, with the same setup as for C-SF galaxies.

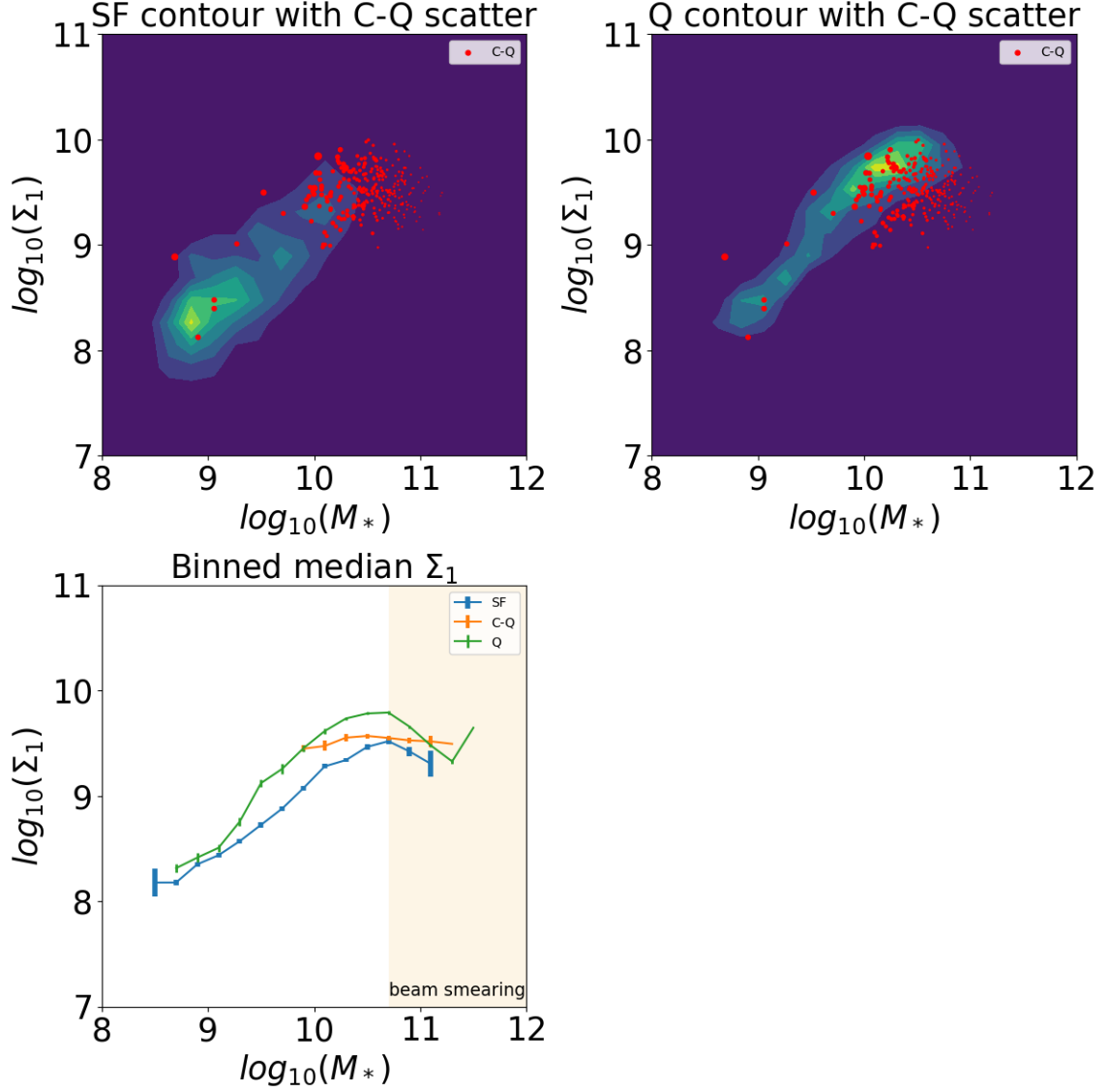


Figure 5.5: This figure illustrates the average Σ_1 values in a series of mass bins. The upper left panel shows the distribution of star-forming galaxies on a $\log_{10} M_*$ versus the Σ_1 map, with contours and scatters. The location of C-Q galaxies is indicated by dots, with dot size representing the weight of each galaxy. The upper right panel has the same layout as the upper left panel, with quiescent galaxies replacing star-forming galaxies. In the lower panel, the binned data is presented as a dot of the average and a bar of the error. The bin edges range from 8.0 to 12.0, increased by 0.2. The dot representing the bin has a mass value equal to the average of the two edges. Three polygonal lines are shown, representing the type of galaxies. The method of calculating the average and the error is provided in the appendix.

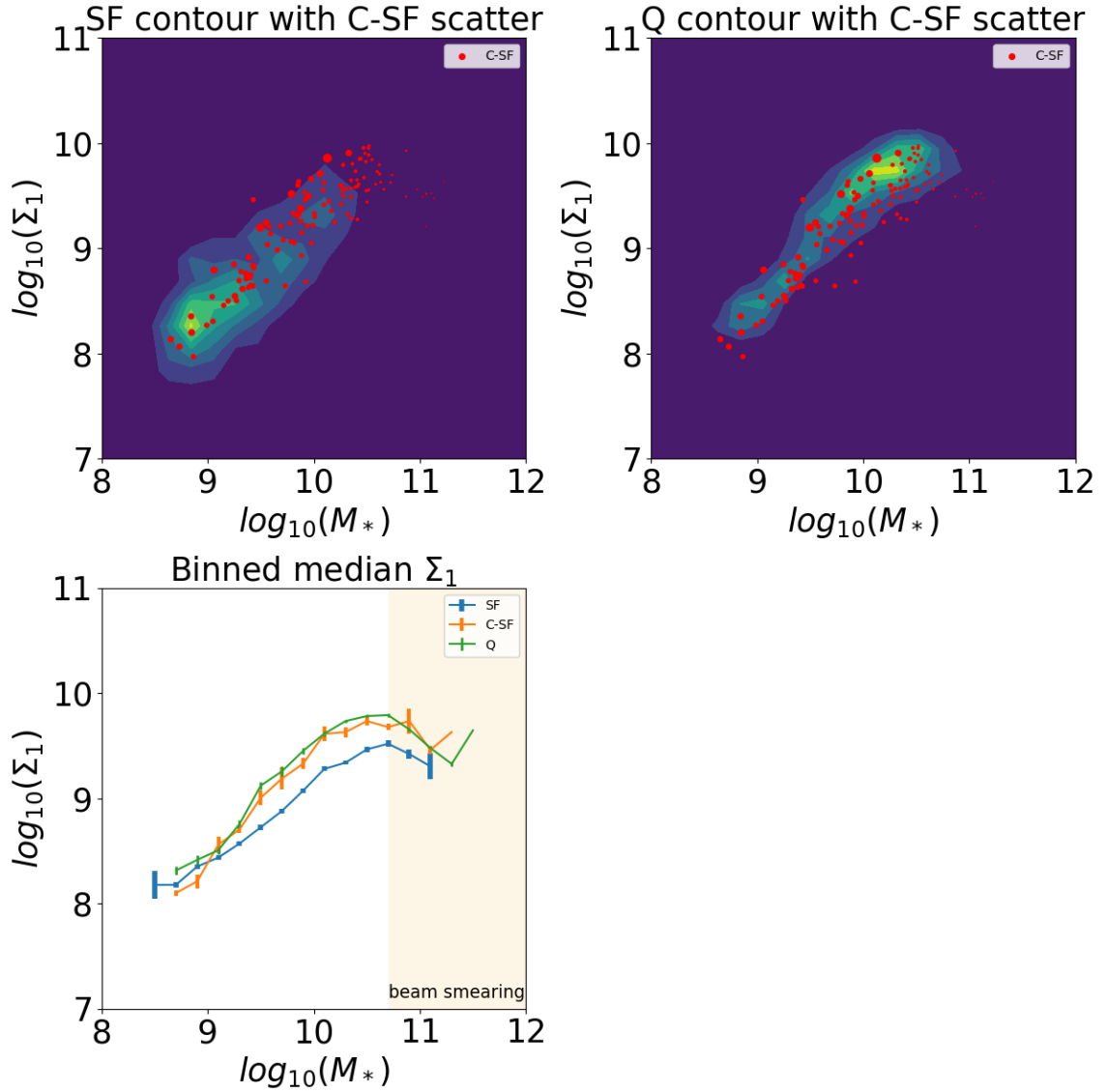


Figure 5.6: This figure has the same layout as Figure 5.5, but with C-Q galaxies replaced by C-SF galaxies. The upper left and right panels show the distribution of star-forming and quiescent galaxies on a $\log_{10} M_*$ versus Σ_1 map, respectively, with C-SF galaxies overlaid as weighted dots. The lower panel displays the binned data with the mean value and error bar, as well as three polygonal lines representing the different types of galaxies. The edges of the bins range from 8.0 to 12.0 and increase by 0.2. The mass value of the dot representing the bin is the average of the two edges.

central region and a fainter but more extended outer region, while lower concentration values suggest a less dense center. Since the light profiles of star-forming (SF) and quiescent (Q) galaxies exhibit distinct characteristics, their concentration values also differ. In our analysis, we focus on the z -band concentration (referred to as z -concentration) as it corresponds to the reddest band in the Sloan Digital Sky Survey (SDSS) and is less sensitive to ongoing star formation. By examining the z -concentration values, we gain insights into the structural properties of galaxies, specifically the relative brightness distribution within the central and outer regions.

In the case of central-quiescent (C-Q) galaxies, the z -band concentration value falls between those of SF and Q galaxies, displaying significant differences from both. The difference in mean concentration values between C-Q and SF galaxies is approximately 4.7σ , with the K-S test rejecting the null hypothesis at a significance level of $p < 0.01$. Similarly, the difference between C-Q and Q galaxies is around 8.4σ , leading to the rejection of the null hypothesis at $p < 0.01$.

For central-star-forming (C-SF) galaxies, the z -band concentration value also lies between SF and Q galaxies and differs significantly from both. The mean concentration difference between C-SF and SF galaxies is approximately 11.5σ , with the K-S test rejecting the null hypothesis at $p < 0.01$. The difference between C-SF and Q galaxies is approximately 2.1σ , resulting in the rejection of the null hypothesis at a significance level of $p = 0.04$, which is consistent with the observed 2.1σ difference.

These findings align with the observations of Σ_1 , supporting the notion that C-Q galaxies possess distinct characteristics compared to both SF and Q galaxies. Meanwhile, C-SF galaxies exhibit some similarities to Q galaxies but significantly differ from SF galaxies. Collectively, these results provide additional evidence that C-Q galaxies form a unique population separate from SF and Q galaxies, while C-SF galaxies may originate from Q galaxies but display notable deviations from typical SF galaxies.

5.5 Full spectrum fitting: pPXF with MaSTAR

We decide to fit the spectrum in the central part ($<0.3 R_e$) since, under our definition, the central parts of monotonical-transition galaxies are either uniformly quiescent or star-forming. If we only perform full spectrum fitting within the central region, we can prevent mixing the star-forming and quiescent regions. We also performed full spectrum fitting on the outskirts region ($1.0 R_e$ - $1.2 R_e$) of monotonic-transition galaxies (MTGs). Within these regions, the spaxels are not guaranteed to be uniform, but most belong to the quiescent or star-forming category. The SFH on the outskirts can provide additional information, thus helping us better understand how MTGs form.

For the full spectrum fitting, we select pPXF as our fitting method ([20, 18]), and the template from MaSTAR ([74]). pPXF is a well-known fitting mechanism, and it is powerful, general, and robust. With the advanced spectrum from MaSTAR, we believe this combination is optimal.

To avoid mixing the star-forming and quiescent regions, we chose to fit the spectrum within the central part of MTGs, which is defined as $<0.3 R_e$. Here, we can

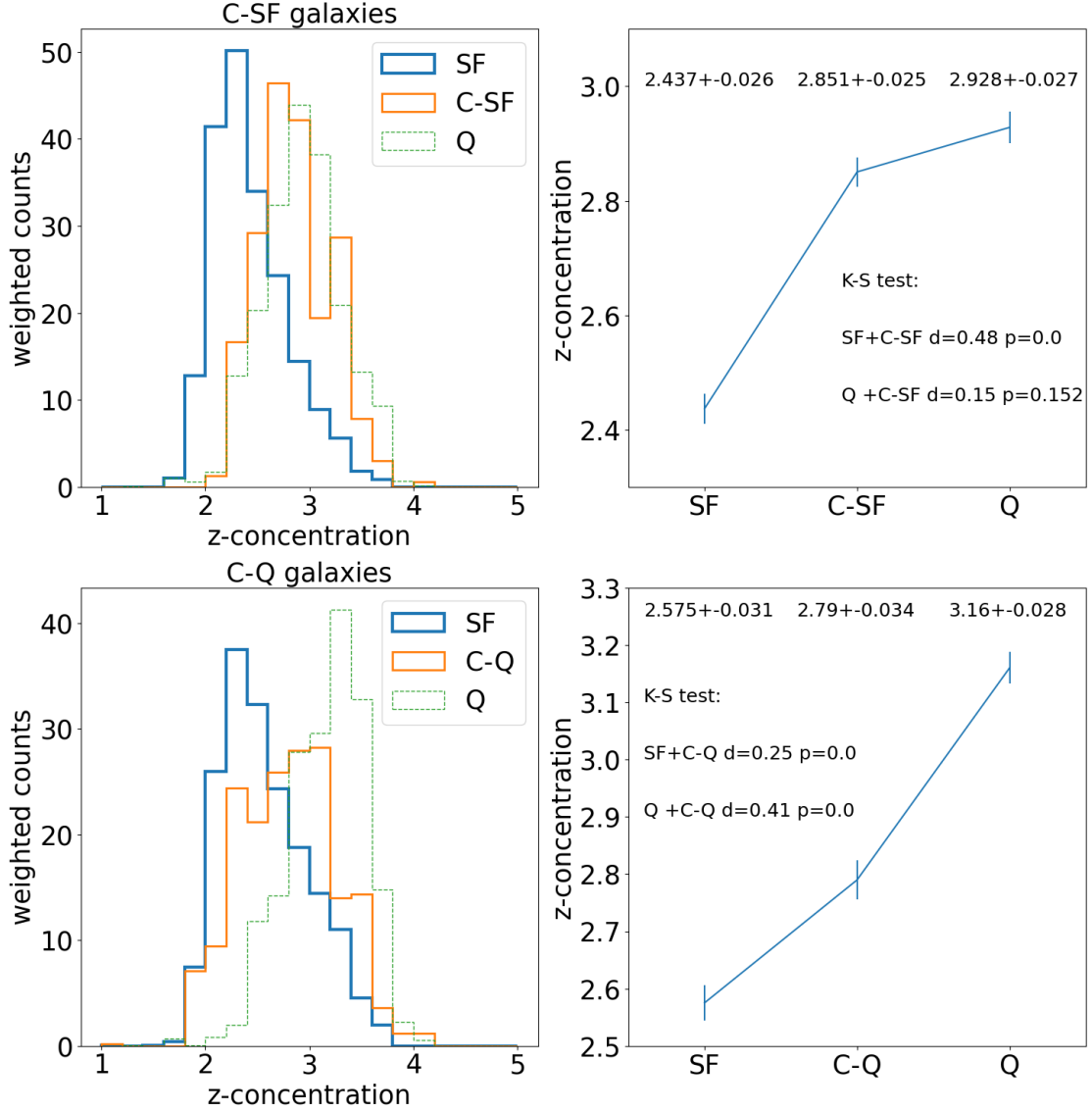


Figure 5.7: This figure presents the difference in concentration between monotonic-transition galaxies and comparison samples. The comparison samples consist of star-forming and quiescent galaxies, matched to the mass distribution of C-SF and C-Q galaxies, respectively. The upper panels display the z -band concentration values of C-SF and C-Q galaxies, with the corresponding comparison samples. The upper left panel shows the histogram of z -concentration, while the upper right panel displays the mean value and the corresponding error bar, as well as the results of the K-S tests between C-SF galaxies and star-forming galaxies, and between C-SF galaxies and quiescent galaxies. The lower panels have the same layout, with C-Q galaxies replacing C-SF galaxies.

capture the uniform star-forming or quiescent regions. Additionally, we also fit the spectrum on the outskirts region of MTGs ($1.0 R_e$ - $1.2 R_e$) to obtain further information on the SFH. Though the spaxels in the outskirts region are not necessarily uniform, most belong to the quiescent or star-forming category.

5.5.1 Central regions of C-Q galaxies

We used pPXF to analyze the spectrum of the central region ($<0.3 R_e$) of C-Q galaxies, and adopted the primary weight to obtain the weighted average SFH. We also performed pPXF on the spectrum of quiescent galaxies in the same regions and then matched the stellar mass of quiescent galaxies to C-Q galaxies by applying an additional weight. This additional weight ensured that the stellar mass distribution of C-Q and quiescent galaxies matched, thereby minimizing the bias in the comparison. By comparing the SFH of quiescent galaxies and C-Q galaxies, we can gain insight into the formation of MTGs. Figure 5.8 illustrates this comparison.

Figure 5.8 shows that the majority of the stellar populations in the central region of central-quiescent galaxies belong to an old, metal-poor population located in the upper left corner of the plot. This finding is consistent with the star formation history of quiescent galaxies. However, younger populations with a relatively rich metallicity and an age of about 1 Gyr are also present in the central region of C-Q galaxies, indicating that star formation occurred in the past 1 Gyr.

The significant difference between the star formation history of the central region of C-Q galaxies and star-forming galaxies is expected since the central region of C-Q galaxies is ‘quiescent’ by our definition. This plot also indicates that there is no ongoing star formation in the central regions of central-quiescent galaxies.

5.5.2 Central regions of C-SF galaxies

The procedure we employed for C-SF galaxies is similar to that used for C-Q galaxies. We performed pPXF on the central region and matched the stellar mass. The results are presented in Figure 5.9.

Figure 5.9 reveals that the star-forming history of the central regions of C-SF galaxies still contains some ongoing star formation, but is markedly different from that of typical star-forming galaxies. The old population of stars is also present in the central region of C-SF galaxies, indicating that the long-term star-forming history of these galaxies may be similar to that of quiescent galaxies. These findings suggest that rejuvenation could play a role in the formation of these galaxies.

5.5.3 Supplements: pPXF in the outskirts of MTGs

As previously mentioned, the star formation status in the outskirts of MTGs may not be entirely uniform, but it is expected to be highly uniform, as only a small percentage of MTGs have a transition radius greater than $1.0 R_e$. This uniformity is sufficient for us to consider the pPXF result on the outskirts as a supplement to better comprehend the formation of MTGs.

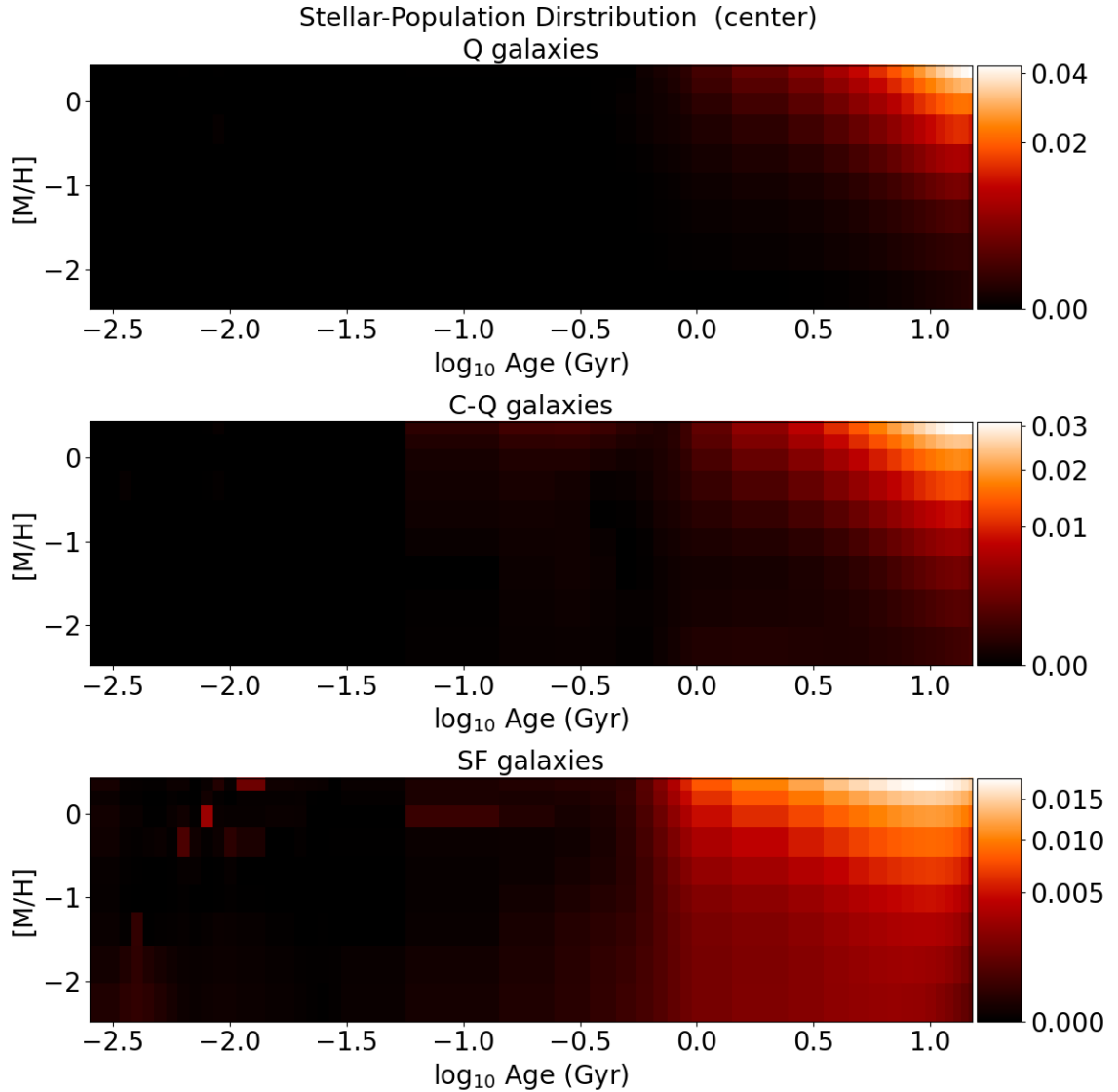


Figure 5.8: This figure displays a comparison of the star formation history between the central regions of central-quiescent galaxies and the same regions of quiescent and star-forming galaxies. The panels are divided into three sections: the top panels are for quiescent galaxies, the middle panels are for C-Q galaxies, and the bottom panel is for star-forming galaxies. Each panel has a set of boxes, where each box represents the weight of the template of a specific age and metallicity. The ages and metallicities are marked on the horizontal (x) and vertical (y) axes, respectively. The value of each box is color-coded, and the color bar is shown on the left side of each panel. Please note that the color bars are not on a linear scale but on a power law scale with a power of 0.5. It is also important to note that the metallicities and ages of the MaSTAR model have non-linear spacing.

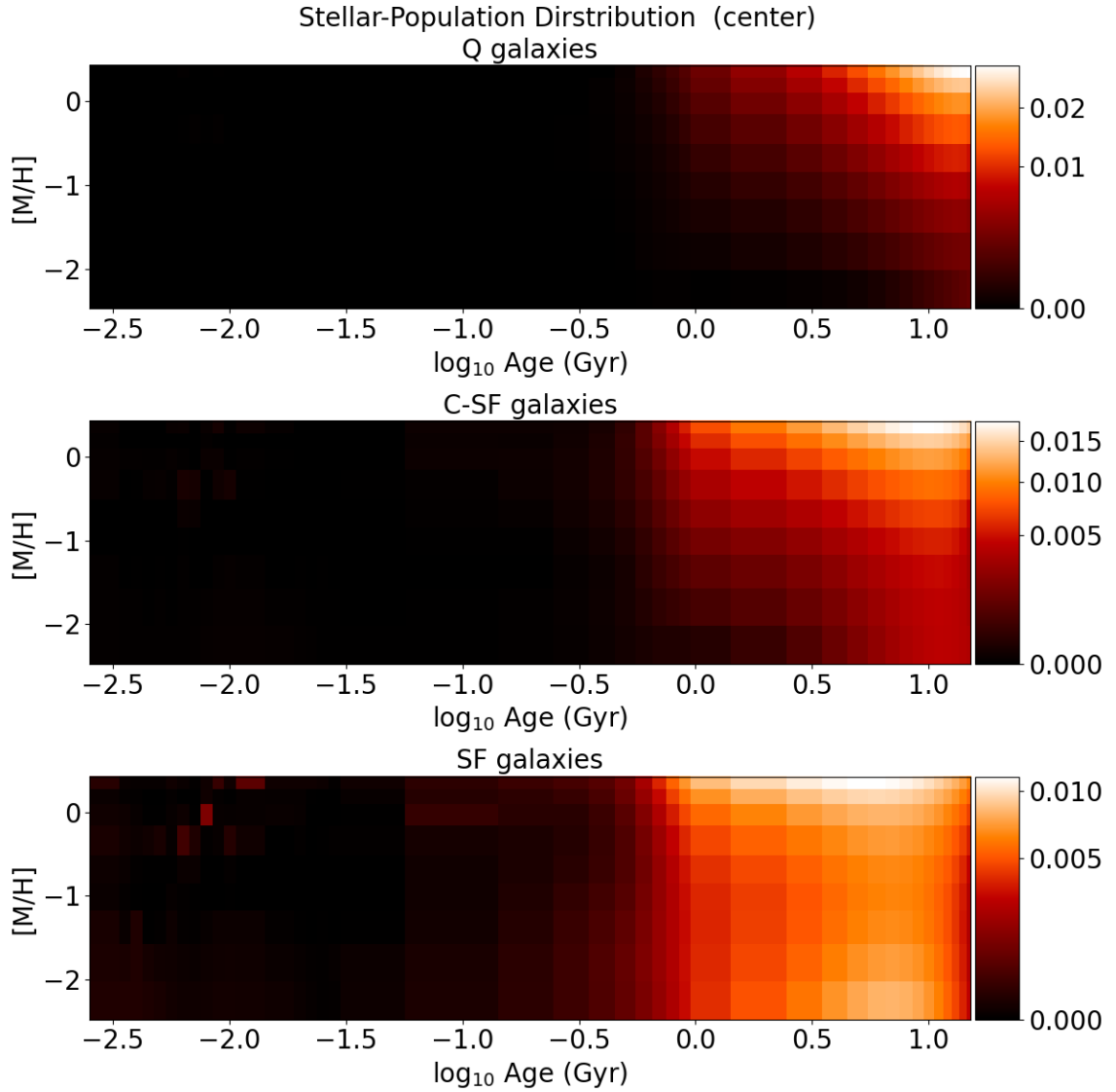


Figure 5.9: This figure displays a comparison of the star formation history of the central regions of C-SF galaxies with the same regions of quiescent and star-forming galaxies. The set up is identical with Figure 5.8

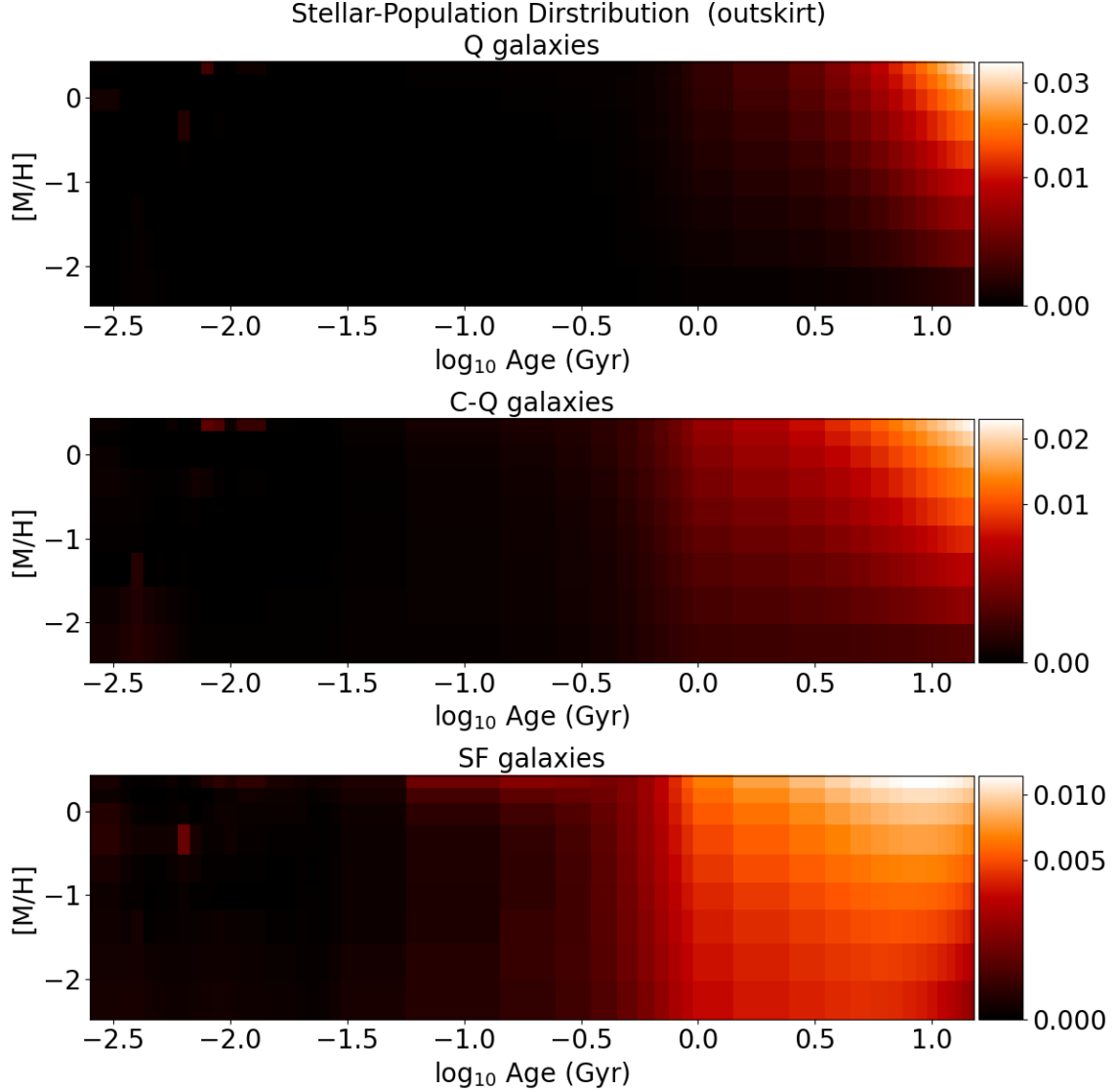


Figure 5.10: This figure shows a comparison of the star formation history of the outer regions of C-Q galaxies with that of quiescent and star-forming galaxies. The set up is identical with Figure 5.8

Outskirts of C-Q galaxies

Figure 5.10 presents the pPXF results for the outer region of C-Q galaxies, compared to the corresponding regions in star-forming and quiescent galaxies. Since C-Q galaxies are defined to have star formation on their outskirts, we can use this figure to better understand their star formation history. The layout of this figure is identical to the previous ones. From the results, we can see that although there is indeed some star formation on the outskirts of C-Q galaxies, their star formation history is more similar to quiescent galaxies than star-forming galaxies. Specifically, the oldest population on the outskirts of C-Q galaxies has an age of ~ 10 Gyrs, which is similar to

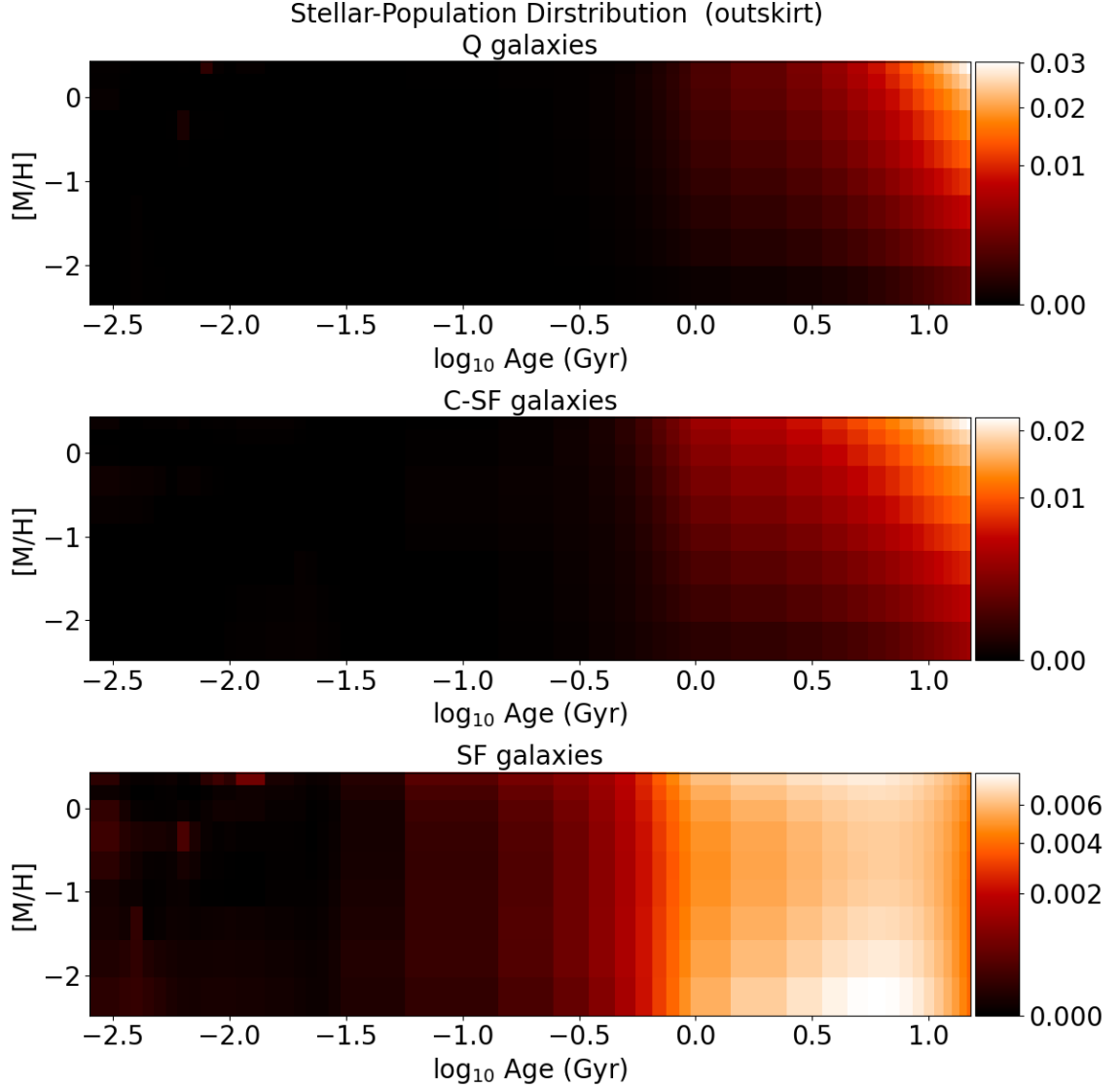


Figure 5.11: This figure displays a comparison of the star formation histories of the outer regions of C-SF galaxies to those of quiescent and star-forming galaxies. The set up is identical with Figure 5.8

that of quiescent galaxies. In contrast, the oldest population of star-forming galaxies is younger (~ 7 Gyrs). This finding suggests that the long-term star formation history of C-Q galaxies is more similar to quiescent galaxies, meaning that when the current star formation stops, their outskirts will resemble those of quiescent galaxies.

Outskirts of C-SF galaxies

Figure 5.11 presents the comparison of the star formation history in the outskirts of C-SF galaxies with Q and SF galaxies. We observe that the outskirts of C-SF galaxies

is highly similar to quiescent galaxies, except for a small population of stars with an age of 1 Gyr present in the outskirts of C-SF galaxies.

Chapter 6 Possibilities of AGN influence on quenching

6.1 AGN statistics

In Section 4.4, we observed distinct differences between the statistical distributions of weak-AGN and typical galaxies. This phenomenon prompted further investigation, leading us to delve deeper into our data set to determine what additional insights could be gleaned.

We propose to scrutinize the statistics of AGN within our sample. It is important to note that weak-AGN and AGN will be discussed separately, given the distinct definitions we have assigned to each category.

6.1.1 Statistics of weak-AGN

For galaxies classified as weak-AGN, the innermost bin contains AGN spaxels ranging from 5% to 20% of the total. Due to their relatively low fraction of AGN spaxels, we have decided to mask them off. This is effectively assuming the star-forming probability among these spaxels is the same as that among non-AGN spaxels in the same ring. Consequently, we can categorize these galaxies using the same procedure as for normal galaxies.

By this approach, we can assign a galaxy type to these weak-AGN galaxies. The statistical results are presented in Table 4.2. Notably, a significant difference between the non-AGN and weak-AGN samples is observed. The fraction of quiescent (Q) galaxies decreases significantly, while the fraction of central-star-forming (C-SF) galaxies increases significantly. This finding suggests the potential coexistence of central star formation activity and AGN activity, providing evidence for a correlation between AGN and star formation.

Furthermore, we observe a significant increase in the fraction of central-quiescent (C-Q) galaxies. This indicates that weak-AGN can coexist with quiescent regions in the central part. This relationship may be linked to the outskirts of these galaxies since C-Q galaxies exhibit star formation in their outskirts, while C-SF galaxies exhibit quiescence in their outskirts.

Based on these findings, we propose a bold hypothesis that the correlation between AGN and the presence of star formation depends on whether the AGN occurs in a star-forming galaxy or a quiescent galaxy. If the host galaxy of the AGN is star-forming, we are likely to observe a correlation between the AGN and central quiescence. On the other hand, if the host galaxy of the AGN is quiescent, we are more likely to observe a correlation between the AGN and star formation in the central region.

6.1.2 Statistics of AGN

The statistical analysis for AGN galaxies differs significantly from that of weak-AGN galaxies due to a higher fraction of AGN spaxels. Masking off these spaxels, as done with weak-AGN galaxies, is neither feasible nor accurate. Additionally, the star

formation status of AGN galaxies remains ambiguous, preventing hasty classification as either star-forming or quiescent.

To address this challenge, our approach involves considering both quiescent (Q assumption) and star-forming (SF assumption) states, followed by type calculations for each assumption. We record the types under both assumptions, and the results are presented in Table 6.1.

Table 6.1 displays the distribution of AGN types under both the SF and Q assumptions. The horizontal labels represent the calculated types of AGN galaxies under the Q assumption, while the vertical labels correspond to the calculated types under the SF assumption. The numerical values within each cell indicate the percentage of galaxies with the corresponding horizontal and vertical types. The cell color represents the relative frequencies of occurrence.

The table reveals three major AGN types: SF+SF (type from the Q assumption combined with types from the SF assumption), Q+C-SF, and C-Q+SF. These cases correspond to AGN occurring within star-forming galaxies with relatively small AGN regions, AGN with quiescent outskirts, and AGN with star-forming outskirts, respectively. The upper panel of Figure 6.1 gives us a demonstration of how the AGN region, star-forming region, and quiescent region are arranged in these galaxies. These observations suggest that AGN can occur in both star-forming and quiescent galaxies, and the underlying physical mechanisms may vary. This finding aligns with the hypothesis proposed in the previous section.

Other significant types include Q+SF, Q+Q, C-SF+C-SF, C-Q+C-Q, and C-Q+Q-Ring. The middle and lower panels of Figure 6.1 show us how the AGN region, star-forming region, and quiescent region are arranged in these types of AGN galaxies. The Q+Q, C-SF+C-SF, and C-Q+C-Q types indicate no change in type between the Q and SF assumptions, suggesting relatively small central AGN regions. Comparing these cases with the weak-AGN samples reveals a similarity, as these may serve as transition states between AGN and weak-AGN galaxies. The Q+SF case suggests that the AGN region is large enough to cover the entire galaxy within $1.2 R_e$. These galaxies could represent special cases of C-Q+SF or Q+C-SF. Further investigation is required to differentiate between these possibilities.

The last significant type is C-Q+Q-Ring galaxies. These galaxies can be explained by the same hypothesis as C-Q+SF and C-Q+C-Q galaxies, where the central AGN region may be small(C-Q+C-Q), intermediate(C-Q+Q-Ring), or large(C-Q+SF). The outskirts of these three types consist of an intermediate ring of quiescence and an outer ring of star formation. The middle panel of Figure 6.1 shows us the similarities of these galaxies. We hypothesize that these three types of galaxies are essentially the same, differing only in the size of the central AGN region.

6.2 Possible AGN influence on quenching

Based on our comprehensive analysis of weak-AGN and AGN galaxies, we propose a detailed hypothesis that the origin of AGN within star-forming (SF) and quiescent(Q) galaxies is distinct, resulting in different correlations with the star formation status. Specifically, AGNs occurring in SF galaxies are correlated with the

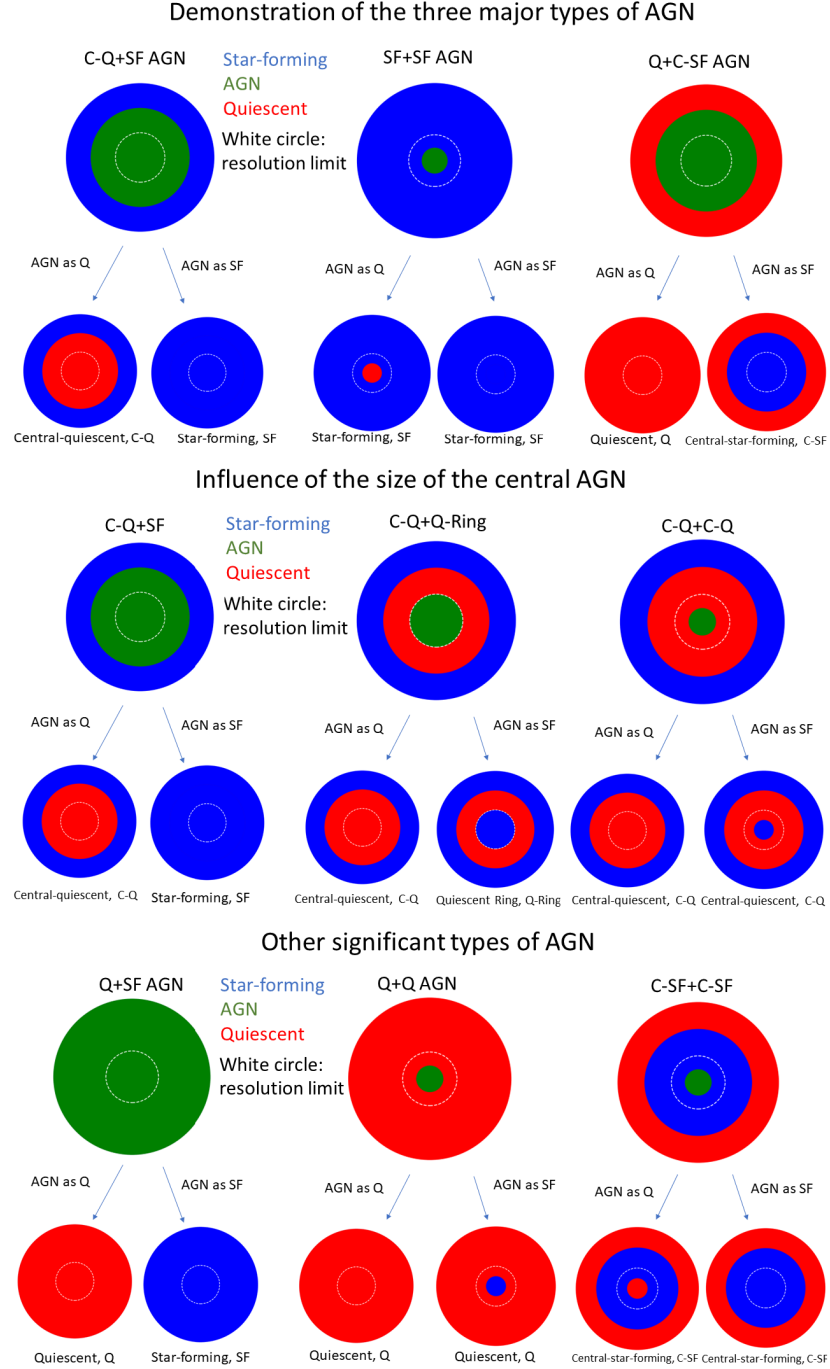


Figure 6.1: This figure illustrates different types of AGN in galaxies, represented by concentric circles and rings with varying colors. The color of each ring or circle indicates the nature of the corresponding region, with blue representing star-forming regions, red indicating quiescent regions, and green representing AGN regions. The larger upper demo within each panel showcases the overall status of the galaxies. The lower two demos within each panel display the hypothetical scenarios where the AGN regions are treated as either quiescent or star-forming, as mentioned in Section 3.2. The white dashed ring indicates the size of the resolution limit. Please note that the circles and rings are used for illustrative purposes and do not represent precise measurements or scales.

Table 6.1: This table presents the frequencies of galaxy types within the AGN sample. The horizontal labels indicate galaxy types when AGN spaxels are treated as completely quiescent, while the vertical labels represent galaxy types when AGN spaxels are treated as completely star-forming. Each cell contains a numerical value indicating the percentage of galaxies with the corresponding horizontal and vertical labels. The color of each cell reflects its relative significance: cells with more than 10% of the sample falling within them are colored red, cells with 3% to 10% are colored yellow, and cells with less than 3% are colored green. The table provides an overview of the distribution of galaxy types within the AGN sample, highlighting the relative prevalence of different categories.

		AGN as Q					
		SF	Q	C-SF	C-Q	SF-Ring	Q-Ring
AGN as SF	SF	14.82	6.83	1.21	26.93	0.90	1.97
	Q	0	3.00	0	0	0	0
	C-SF	0	21.88	5.61	0	1.13	0
	C-Q	0	0.43	0	7.52	0.34	0
	SF-Ring	0	0.01	0	0	0	0
	Q-Ring	0	0.07	0	5.80	1.57	0

cessation of star formation in the central region, while AGNs within quiescent galaxies are associated with the rejuvenation of star formation in the central region. It is important to note that establishing a causal relationship between AGN and star formation is challenging since they may arise from separate physical processes, and a direct causal connection between them is not necessarily present.

To further investigate and test this hypothesis, we intend to examine the $H\alpha$ equivalent width in the central regions of AGN galaxies and compare it with a control sample comprising normal galaxies with similar mass distributions. This analysis will allow us to infer whether the central AGN activity coincides with ongoing star formation or is merely present alongside existing star formation.

6.2.1 $H\alpha$ equivalent width approach

If AGN activity were to enhance star formation, we would expect galaxies with a central AGN and a star-forming periphery to exhibit higher central $H\alpha$ emission compared to galaxies characterized solely by star formation (SF galaxies). Based on this fact, we have divided our comparison into two distinct groups. Firstly, we compare C-Q+SF AGN galaxies with star-forming outskirts to star-forming(SF) galaxies and central-quiescent (C-Q) galaxies, given their shared star formation status in the periphery. Similarly, we compare Q+C-SF AGN galaxies with quiescent outskirts to quiescent (Q) galaxies and central-star-forming (C-SF) galaxies. Our focus is on comparing the $H\alpha$ equivalent width at different locations within these galaxies, specifically at $<0.3 R_e$, $0.6 R_e$ - $0.7 R_e$, and $1.0 R_e$ - $1.2 R_e$.

In Figure 6.3, we illustrate the differences between C-Q+SF AGN, SF galaxies,

and C-Q galaxies. The upper section of the figure reveals that the central regions of C-Q galaxies exhibit significantly lower brightness, as expected due to the absence of an ionization source in their centers. SF and AGN galaxies display similar average values of $H\alpha$ equivalent width, but their distributions show slight deviations: SF galaxies exhibit a wider spread, with central region $H\alpha$ equivalent width values ranging from as large as 40 to as small as 5. On the other hand, AGN galaxies show a more concentrated distribution, with no galaxies having values smaller than 6 or larger than 25. These differences are not significantly pronounced, leading us to conclude that there is no notable difference between the $H\alpha$ equivalent width (EW) histograms of AGN and SF galaxies. This evidence contradicts the notion that AGN activity is associated with the central enhancement of star formation, which aligns with the AGN inside SF galaxy aspect of our hypothesis.

The middle and lower panels of Figure 6.3 provide further insights into these galaxies. We will omit discussing the intermediate region as the star formation status of these galaxies may be inconsistent, with C-Q galaxies potentially being either star-forming or quiescent at this radius. In the outermost bin, AGN consistently exhibits an intermediate $H\alpha$ EW between SF galaxies and C-Q galaxies. While C-Q galaxies maintain some level of star formation in their outskirts, it is not as robust as in SF galaxies. AGN galaxies follow a similar trend but with slightly higher $H\alpha$ EW than C-Q galaxies. This observation suggests that AGN activity may be associated with the suppression of star formation.

In Figure 6.2, we examine the differences in $H\alpha$ equivalent width between Q+C-SF AGN galaxies, quiescent (Q) galaxies, and central-star-forming (C-SF) galaxies. All three types of galaxies have been matched to the same total stellar mass distribution, specifically that of Q+C-SF AGN galaxies. In the upper panel of the plot, which represents the innermost bin, the $H\alpha$ equivalent width of Q+C-SF AGN galaxies is actually slightly higher than that of C-SF galaxies. This finding provides evidence of the coexistence of AGN and star formation within Q+C-SF galaxies, supporting our hypothesis.

This phenomenon is also observed in the two outer bins. The $H\alpha$ equivalent width of Q+C-SF galaxies remains higher than that of C-SF galaxies of the same mass in these regions as well.

The observed $H\alpha$ equivalent width of Q+C-SF and C-Q+SF AGN galaxies aligns with the predictions of our hypothesis, further supporting its validity.

6.2.2 $H\alpha$ surface brightness profile

The $H\alpha$ equivalent width approach provides direct evidence of AGN coexistence with star formation within quiescent galaxies. However, we still lack a direct method to observe AGN coexistence with quiescence within star-forming galaxies. To address this, we investigate the $H\alpha$ surface brightness profile of AGN galaxies.

We focus on the AGN sample consisting of SF+SF, C-Q+SF, C-Q+C-Q, and C-Q+Q-Ring AGNs, all of which exhibit a star-forming outskirt. To ensure optimal performance in capturing the $H\alpha$ surface brightness, we restrict the axis ratio (b/a) to be greater than 0.717, selecting only face-on galaxies.

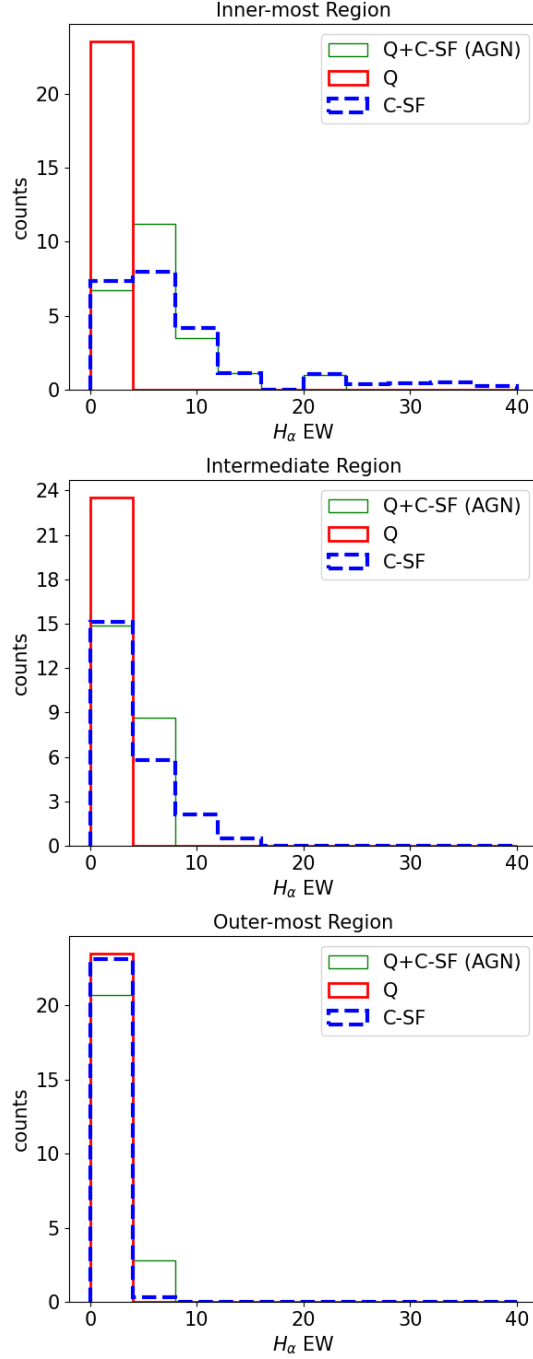


Figure 6.2: This figure compares the H_α equivalent width across AGN with a quiescent outskirts, quiescent galaxies, and C-SF galaxies with a matched mass distribution at different locations within galaxies. The top panel represents the H_α equivalent width comparison for the innermost bin ($r < 0.3 R_e$). The middle panel displays the H_α equivalent width for an intermediate bin ($0.6 R_e < r < 0.7 R_e$), and the bottom panel illustrates the same for the outermost bin ($1.0 R_e < r < 1.2 R_e$). Note that the counts displayed have been adjusted for volume limitation; thus, they represent relative counts and not the actual number of galaxies.

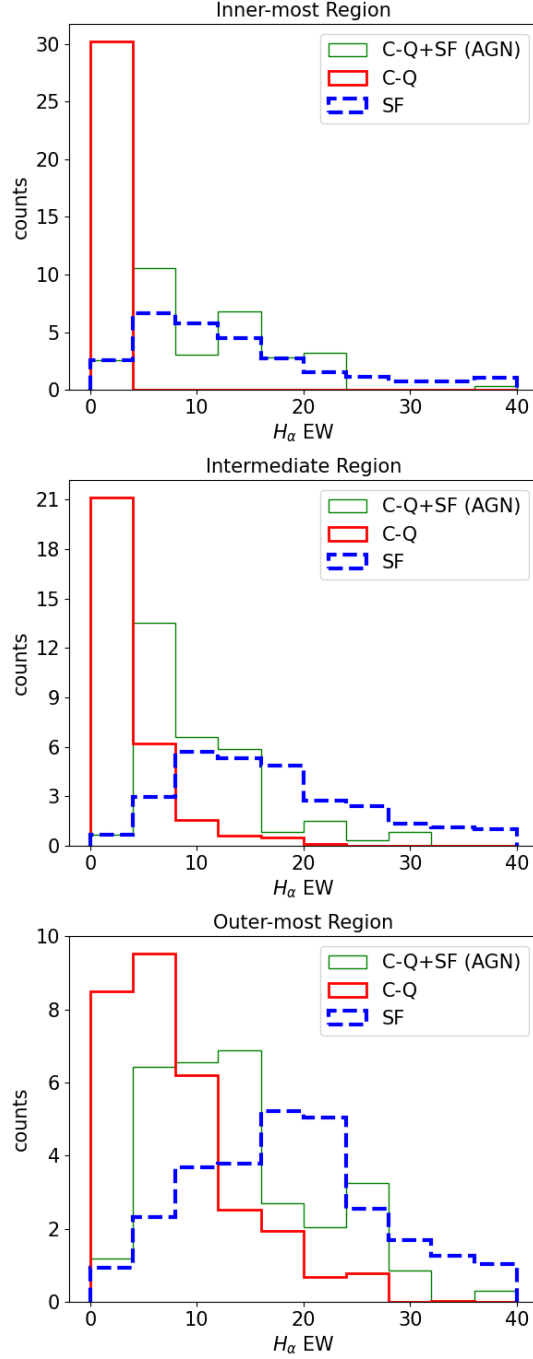


Figure 6.3: This figure compares the H_α equivalent width across AGN with an SF outskirt, SF galaxies, and C-Q galaxies with a matched mass distribution at different locations within galaxies. The top panel represents the H_α equivalent width comparison for the innermost bin ($r < 0.3 R_e$). The middle panel displays the H_α equivalent width for an intermediate bin ($0.6 R_e < r < 0.7 R_e$), and the bottom panel illustrates the same for the outermost bin ($1.0 R_e < r < 1.2 R_e$). Note that the counts displayed have been adjusted for volume limitation; thus, they represent relative counts and not the actual number of galaxies.

Figure 6.4 presents the median-normalized $H\alpha$ surface profile of AGN galaxies that meet our selection criteria. We normalize the $H\alpha$ surface brightness of each individual galaxy by dividing it by the median value of $H\alpha$ surface brightness within that galaxy. This ensures that we compare only the profile's trend, minimizing the dispersion of intrinsic values. We then bin the $H\alpha$ surface brightness values by radius and calculate the median value within each bin, resulting in an individual galaxy's $H\alpha$ surface brightness profile. Taking the median values across all galaxies, we obtain the median-normalized $H\alpha$ surface brightness profile.

From Figure 6.4, we observe that the surface brightness starts at a relatively high value in the center, decreases towards the outskirts, rises again, and then decreases. This bi-peak profile of the $H\alpha$ surface brightness signifies the presence of two peaks: the central peak corresponds to $H\alpha$ emission from the AGN, while the outer peak corresponds to $H\alpha$ emission from star formation. This suggests that star formation is suppressed in the central regions, supporting our hypothesis.

Further examination at the individual galaxy level reveals the presence of this bi-peak feature in almost every galaxy, providing additional confirmation of its existence. Plots depicting the profiles of each individual galaxy will be included in the appendix.

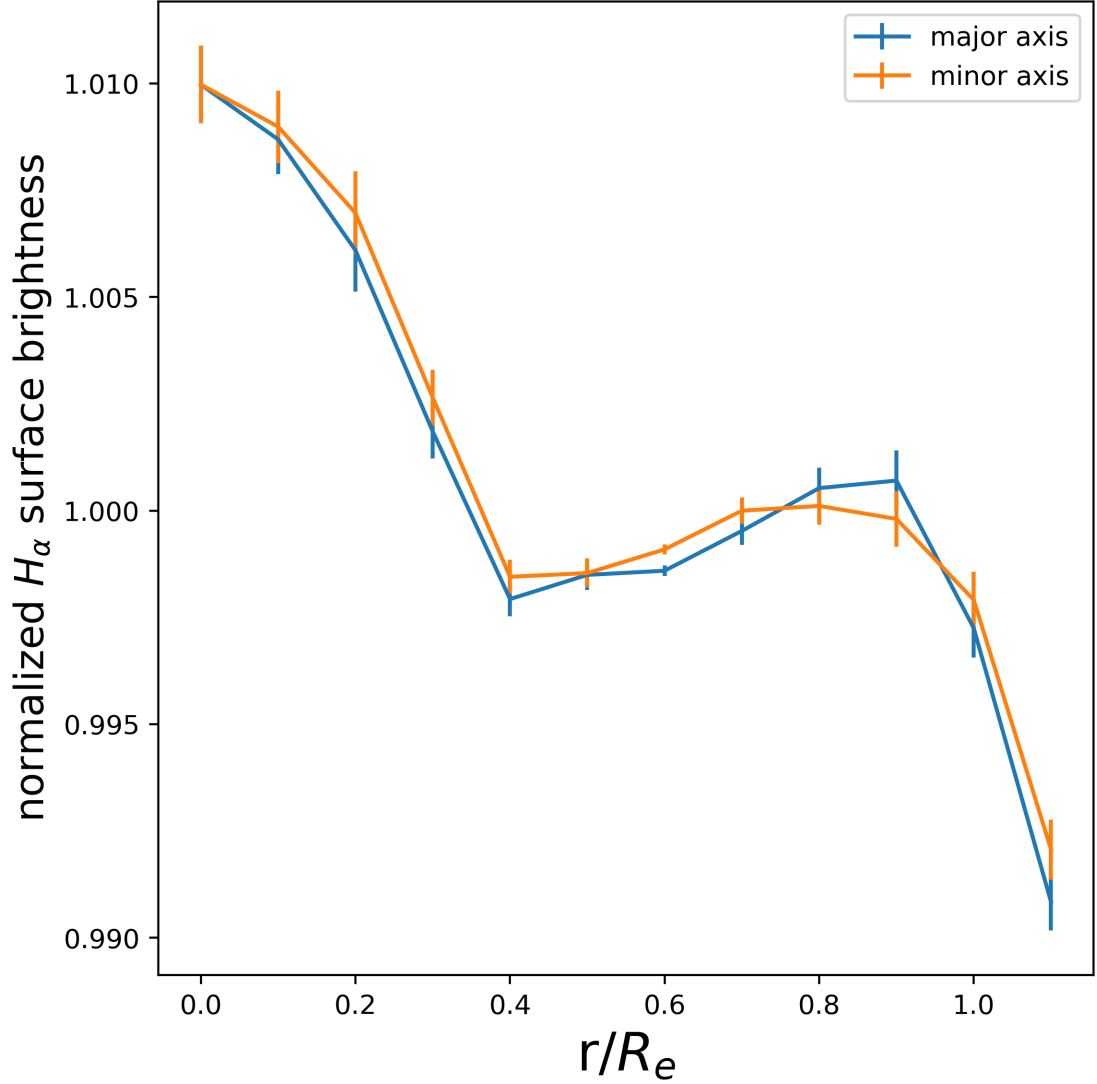


Figure 6.4: This figure illustrates the bi-peak feature observed in the normalized median $H\alpha$ surface brightness profile. The x-axis represents the radius in units of R_e , while the y-axis shows the normalized median $H\alpha$ surface brightness. The profile is obtained by normalizing the $H\alpha$ surface brightness profile of each individual galaxy by its median value and then taking the median value over the entire sample. The plot includes two curves: the blue curve represents spaxels near the major axis of galaxies, defined as any pixel within the two 45-degree sectors centered on the major axis (one for each direction), while the orange curve represents spaxels near the minor axis, defined as any pixel within the two 45-degree sectors centered on the minor axis (one for each direction). The error bars in the plot represent the standard deviation of the $H\alpha$ surface brightness profiles of the individual galaxies.

Chapter 7 Discussion

7.1 Non-AGN galaxies

7.1.1 Short-term features and long-term features

We have examined several features of galaxies in an attempt to understand the formation of the MTGs. These features can be sorted into two types: short-term features and long-term features, which are defined as follows:

- Short-term features: These refer to characteristics that can be significantly altered by recent star formation activity. In our study, we classify emission line flux, emission line equivalent width, and photometry data in a blue band as short-term features. Additionally, if we consider only the star formation history (SFH) within the past 1 Gyr, it can be categorized as a short-term feature.
- Long-term features: These encompass characteristics that remain relatively unchanged, or at least are minimally affected, by recent star formation bursts. In our analysis, total stellar mass and Σ_1 are regarded as long-term features. The SFH spanning over 1 Gyr is also categorized as a long-term feature.

Long-term features are inherent characteristics of galaxies that are determined by their star formation history and environment since their formation. These features are relatively stable and difficult to change significantly in a short period of time. On the other hand, short-term features are more sensitive to recent events, such as star formation bursts or quenching, and can change more easily. For example, $H\alpha$ emission flux is a short-term feature that is directly related to the current star formation activity, while Σ_1 is a long-term feature that is determined by the total stellar mass and spatial distribution of the old stars.

To investigate the evolutionary relationships between different types of galaxies, we need to consider both their long-term and short-term features. We propose that for one type of galaxy to be a potential progenitor or successor of another type, they should share the same set of long-term features. This is because the short-term features can change rapidly due to recent star formation events, but the long-term features are determined by the galaxy's past and are unlikely to change significantly in a short time. Therefore, if two types of galaxies have significantly different long-term features, they cannot be considered as progenitors or successors of each other.

7.1.2 Central-Quiescent galaxies

To determine the most probable progenitor and successor of C-Q galaxies, we investigate their long-term features, including total stellar mass, Σ_1 , and SFH over 1 Gyr from pPXF. Figure 5.6 shows that C-Q galaxies have a large total stellar mass ($\log_{10} M_* \in [10, 11]$), but their Σ_1 value is between those of Q and SF galaxies. This

suggests that C-Q galaxies have a larger overall mass, but their center is not as dense as that of quiescent galaxies. As a result, it is unlikely that C-Q galaxies will become quiescent galaxies once the outskirts of these galaxies has been quenched, as they cannot increase Σ_1 any further. Since there is no further star formation in the inner part of these galaxies, they are unlikely to evolve into star-forming galaxies.

It is also improbable that these galaxies originated from the quenching of SF galaxies. The SFH of the outskirts of C-Q galaxies indicates the presence of an old population that is not present in SF galaxies. This suggests that the long-term SFH of C-Q galaxies and SF galaxies differ significantly to form this population.

We may propose a duty-cycle hypothesis to explain the behavior of C-Q galaxies. These galaxies can only reach a certain value of Σ_1 through star formation, which is about 9.5 in our sample. Once this threshold is reached, the central regions of the galaxies become quenched. While these galaxies cannot increase their Σ_1 through star formation, they may still be able to increase it through mechanisms such as mergers or dynamical processes ([44, 21, 36, 6]). The outskirts of these galaxies may still experience star formation for an extended period, and this star formation may occur in cycles of activity and quiescence.

In conclusion, our analysis reveals that central-quiescent (C-Q) galaxies occupy an intermediate phase between quiescent (Q) and star-forming (SF) galaxies. This suggests that the evolution path from SF to C-Q and from C-Q to Q is not simply a result of a gradual quenching of star formation. Interestingly, the quenched region within C-Q galaxies does not exhibit a monotonically increasing trend towards the center, which challenges the conventional inside-out transition mode. Instead, the outskirts of C-Q galaxies can experience multiple rounds of star formation bursts, and the galaxies may undergo a transition from a quiescent state to a central-quiescent state. Remarkably, C-Q galaxies can remain in this intermediate phase for extended periods of time. These findings imply that the formation of monotonic-transition galaxies (MTGs) involves complex processes and interactions among different physical mechanisms. Further investigations are necessary to fully comprehend the nature of these galaxies and their role in the broader context of galaxy evolution.

7.1.3 Central-Star-Forming galaxies

C-SF galaxies are intriguing in that all their parameters closely resemble those of quiescent galaxies, including Σ_1 , SFH, color, and z -concentration. This evidence suggests that C-SF galaxies are closely related to quiescent galaxies, but it is unclear which one is the progenitor. The formation of C-SF galaxies could be due to either quenching or rejuvenation processes. Further investigation is needed to determine the exact formation mechanism of C-SF galaxies.

We have observed a significant difference in Σ_1 and z -concentration between C-SF and Q galaxies, with C-SF galaxies having lower values than Q galaxies (see Figures 5.4 and 5.7). This suggests that C-SF galaxies are more likely to be the progenitors of Q galaxies. However, the SFH of C-SF galaxies is very similar to that of quiescent galaxies in both the center and the outskirts, with an old population present in the center of C-SF galaxies but not in SF galaxies of the same mass. This evidence

suggests that there is a difference in the SFH of the central regions of C-SF and SF galaxies, indicating that they cannot be evolutionarily related.

We can further explore the central density of central star-forming (C-SF) galaxies as evidence opposing the quenching scenario. As discussed in the previous section (Section 5.3), we examined the formation of central-quiescent (C-Q) galaxies and the Σ_1 threshold for star-forming galaxies. According to this threshold, when the Σ_1 value of an SF galaxy exceeds approximately 9.5, the central region of that galaxy should undergo quenching. However, we observed that many C-SF galaxies in our sample exceed this threshold while still maintaining star-forming centers. This contradicts the Σ_1 threshold hypothesis. It suggests that either these C-SF galaxies did not undergo quenching, or they followed a different mechanism that does not conform to the Σ_1 threshold.

If the latter possibility holds true, it implies the existence of two distinct populations of SF galaxies: one group that experiences quenching in the center once it reaches the Σ_1 threshold, and another group that undergoes quenching primarily in the outskirts without adhering to the Σ_1 threshold. Although this scenario is plausible, we currently lack direct evidence to support it. Therefore, in the absence of compelling evidence, we choose to adopt the simpler explanation that these C-SF galaxies did not originate from the quenching process.

Based on the discussion above, it seems that the rejuvenation scenario is a more likely explanation for the formation of C-SF galaxies. However, one challenge we face is explaining why C-SF galaxies have a lower Σ_1 and z -concentration than quiescent galaxies. We propose that only a subset of quiescent galaxies may be able to undergo rejuvenation, and these galaxies may have lower Σ_1 and z -concentration than the average quiescent galaxy. This hypothesis warrants further investigation and could potentially shed light on the mechanisms that drive the rejuvenation of some galaxies while others remain quiescent.

7.2 AGN impact of star formation in galaxies

The impact of AGN on star formation in galaxies is a complex phenomenon that can manifest in two possible scenarios: AGN enhancement and AGN quenching.

To explain the correlation between AGN and star formation, we have proposed a hypothesis that considers the role of AGN in both star-forming and quiescent galaxies. Specifically, we suggest that AGN occurring in quiescent galaxies leads to an enhancement of star formation, while AGN in star-forming galaxies results in the suppression of star formation. It is important to note that this correlation does not necessarily imply a causal connection between AGN activity and the enhancement or suppression of star formation.

To test our hypothesis, we have conducted statistical analyses and investigated emission lines, specifically focusing on H α emissions. The evidence obtained strongly supports our hypothesis, suggesting that there is indeed a correlation between AGN activity and the enhancement or suppression of star formation. While these findings provide a reasonable basis for our hypothesis, further efforts are required to confirm its validity. One potential avenue for future research involves decomposing the H α

emission to determine the contributions from AGN-related $H\alpha$ emission and star formation-related $H\alpha$ emission. This would provide a direct measurement of the star formation status and offer additional insights into the mechanisms underlying the AGN-star formation relationship.

In conclusion, our investigation into the effects of AGN on star formation highlights the complexity of this interaction. Our proposed hypothesis provides a framework for understanding the correlation between AGN and star formation in different types of galaxies. The supporting evidence from statistical analyses and emission line studies contributes to our understanding of AGN-driven processes in galaxy evolution, although further investigations and refinements are necessary to fully elucidate the underlying mechanisms.

Chapter 8 Summary

In this study, the radial quenching profile of nearby galaxies is investigated using data from the MaNGA survey, a part of SDSS IV. A new method is developed for analyzing the spatial information of these galaxies, which employs an unconventional approach to determining the current star formation status. The $H\alpha$ EW versus [O II] EW plot provides better separation between star-forming and quiescent regions, avoids dealing with internal attenuation, and requires fewer lines compared to conventional methods like BPT.

The data is binned into radial bins to examine the radial profile of quiescent spaxel distribution, revealing six types of galaxies: star-forming (SF), quiescent (Q), central-star-forming (C-SF), central-quiescent (C-Q), star-forming ring (SF-Ring), and quiescent ring (Q-Ring). These subtypes are organized into pairs based on their radial quiescent profiles: uniform galaxies (SF and Q), monotonic-transition galaxies (C-Q and C-SF), and non-monotonic-transition galaxies (SF-Ring and Q-Ring).

The study finds that the distribution of C-Q and C-SF galaxies is particularly interesting. C-Q galaxies occur only in high-mass galaxies, while C-SF galaxies have a similar color-mass distribution to quiescent galaxies. To further investigate the formation of monotonic-transition galaxies, the size of the inner region, or transition radius, is measured. A close relationship between transition radius and central $H\alpha$ emission strength is discovered.

The Σ_1 and star formation history of monotonic-transition galaxies are also examined. C-Q galaxies have a Σ_1 value between those of SF and Q galaxies, and the relatively flat distribution suggests a threshold of Σ_1 for SF galaxies. When the Σ_1 of an SF galaxy reaches this threshold, its center becomes quenched. C-SF galaxies have a similar Σ_1 to Q galaxies, indicating that they may have originated from the rejuvenation of Q galaxies.

The star formation history analysis supports the rejuvenation hypothesis for C-SF galaxies, revealing the presence of old populations in their centers, similar to Q galaxies. Meanwhile, both the centers and outskirts of C-Q galaxies show more similarity to Q galaxies than SF galaxies. This finding contradicts the Σ_1 analysis, as C-Q galaxies should have a similar outskirts to SF galaxies if they originate from SF galaxies.

To resolve this contradiction, we propose a duty cycle hypothesis for C-Q galaxy formation. These galaxies can only achieve a specific Σ_1 value (~ 9.5) through star formation. Once this threshold is reached, their central regions become quiescent, while their outskirts may continue to experience cyclic star formation. For C-SF galaxies, the rejuvenation of a specific population of quiescent galaxies with slightly lower Σ_1 values is the most likely explanation for their formation.

We conducted a statistical analysis comparing the distribution of different galaxy types between the AGN sample and normal galaxies. Specifically, we examined the distribution of weak-AGN and observed significant differences when compared to normal galaxies. We found that the proportion of quiescent galaxies among weak-

AGN was lower compared to normal galaxies, while the proportion of central star-forming (C-SF) galaxies was higher. This suggests that C-SF galaxies may be more commonly associated with weak-AGN.

Furthermore, we investigated the $H\alpha$ emission line in AGN galaxies and observed a decline in star formation towards the central regions. This provides evidence supporting the notion that AGN in star-forming galaxies are associated with the cessation of central star formation. Conversely, AGN in quiescent galaxies appear to be related to the rejuvenation of star formation in the central regions.

These findings contribute to our understanding of the complex interplay between AGN activity and star formation in galaxies. They suggest that the presence of AGN can have different effects depending on the galaxy's star-forming or quiescent nature. We propose a hypothesis regarding the potential correlation between AGN and star formation in galaxies. Our hypothesis suggests that the role of AGN in galaxy evolution depends on the stage of the host galaxy. If the host galaxy is actively star-forming, we would expect to observe a correlation between AGN activity and the cessation of star formation. On the other hand, if the host galaxy is quiescent, we would anticipate a correlation between AGN activity and the enhancement of star formation.

This hypothesis highlights the different roles that AGN may play in shaping the evolution of galaxies, depending on the specific characteristics of the host galaxy. By considering the stage of the galaxy and the presence of AGN, we can gain further insights into the intricate interplay between AGN activity and star formation processes.

Appendices

Appendix A: Calculation of statistical values in a weighted sample.

Let's assume we have a series of physical values a_1, a_2, \dots, a_k , which are already in ascending order and have a total of k values. Each value a_i has a corresponding positive weight n_i . The weights have been normalized such that the sum of all weights is equal to k , i.e., $\sum_{i=1}^k n_i = k$.

To calculate the weighted median, we first check if there exists an integer p such that $\sum_{i=1}^p n_i = k/2$. If such p exists, we set the weighted median as a_p , i.e., $a_{\text{median}} = a_p$. If no such p exists, we find two successive integers j and $j+1$ that satisfy $\sum_{i=1}^j n_i < k/2$ and $\sum_{i=1}^{j+1} n_i > k/2$. In this case, we set the weighted median as the weighted average of a_j and a_{j+1} , i.e., $a_{\text{median}} = \frac{n_j \times a_j + n_{j+1} \times a_{j+1}}{n_j + n_{j+1}}$.

The weighted mean can be calculated as $a_{\text{mean}} = \frac{\sum_{i=1}^k n_i \times a_i}{k}$.

To compute the scatter or standard deviation, we first calculate the weighted mean a_{mean} as mentioned above. Then, the standard deviation is given by $std = \sqrt{\frac{\sum_{i=1}^k n_i \times (a_i - a_{\text{mean}})^2}{k}}$.

The standard error, denoted as err , is equal to the standard deviation divided by the square root of k , i.e., $err = \frac{std}{\sqrt{k}}$.

Appendix B: H α strength in different regions of galaxies

Since the sSFR estimation method is only applicable to star-forming regions, it cannot be directly applied to estimate the sSFR in quiescent regions. However, we can still use this method to estimate the H α strength in these regions. Figure 5.2 illustrates the H α strength in different regions of central-star-forming (C-SF) and central-quiescent (C-Q) galaxies. Surprisingly, in the central region of C-Q galaxies, which is expected to be uniformly quiescent, there is still a correlation between H α strength and the transition radius. This observation is intriguing and suggests that the mechanism responsible for the H α emission is likely related to the quenching process occurring in these regions.

Figure 8 presents the transition radius versus the specific star-forming rate at different relative radii for both C-Q and C-SF galaxies. The different panels correspond to the core region (within $0.3 R_e$), the intermediate ring (between $0.6 R_e$ and $0.7 R_e$), and the outskirts (between $1.0 R_e$ and $1.2 R_e$). Please note that for regions that are not star-forming, the sSFR is used as an estimate of the H α strength. The figure provides valuable insights into the variation of H α strength across different regions of galaxies and confirms the presence of interesting correlations.

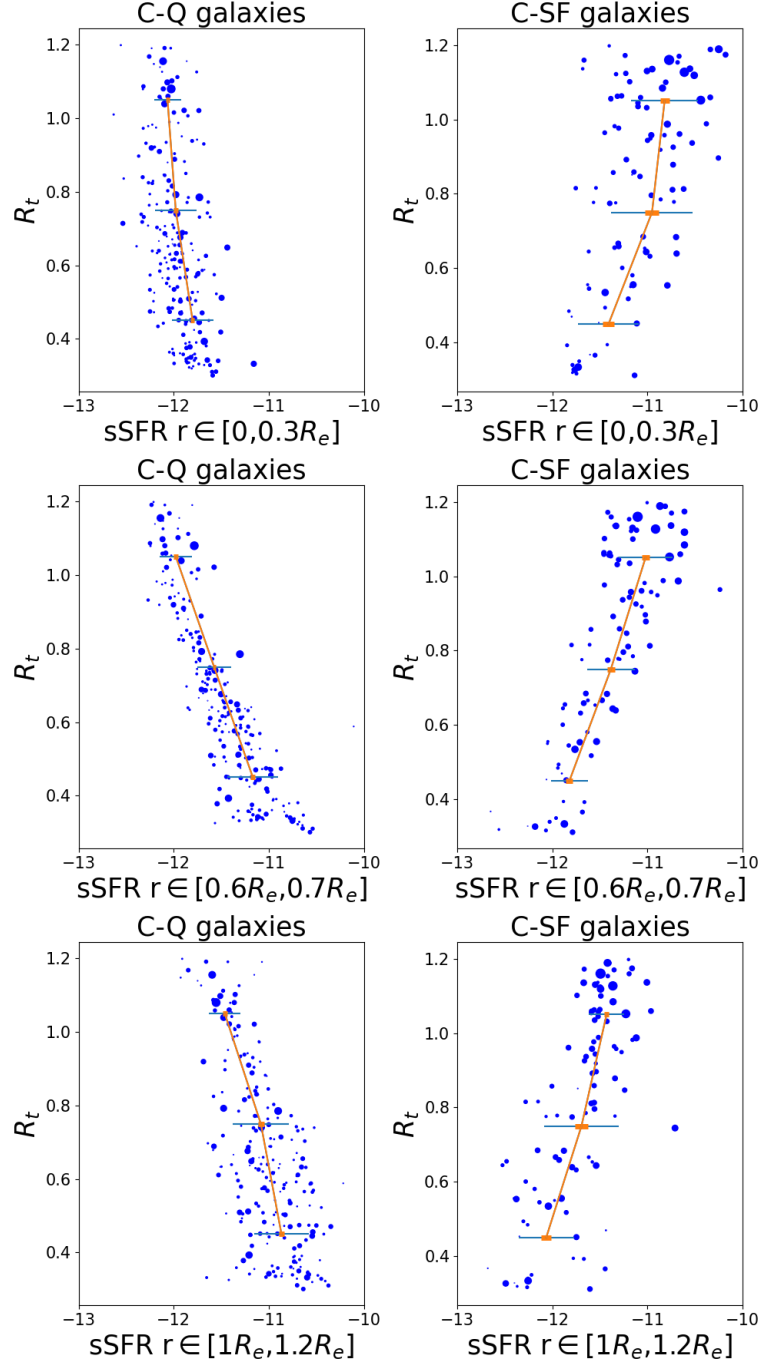


Figure B1: This figure shows the transition radius versus the specific star-forming rate at the different relative radii. The left panels are for central-quiescent galaxies, while the right panels are for central-star-forming galaxies. The upper panels are for the core region(region within $0.3 R_e$), the middle panels are for the intermediate ring(the region between $0.6 R_e$ and $0.7 R_e$), and the bottom panels are for the outskirts(the region between $1.0 R_e$ and $1.2 R_e$). The setting of bins and calculations of median value and error are identical as Figure 5.2. Please note that for regions which are not star-forming, the sSFR is an estimate of the $\text{H}\alpha$ strength.

Appendix C: Beam-smearing effect in Figures 5.5, 5.6

In Section 5, we observed a ‘downturn’ in the plot of Σ_1 versus mass (Figures 5.5 and 5.6). We hypothesized that this downturn is an artificial effect caused by beam-smearing, resulting from the MaNGA PSF’s inability to resolve the 1 kpc scale in galaxies with $\log M_*/M_\odot > 10.7$. By examining the MaNGA selection function, we matched this critical mass of 10.7 to a redshift and found it to be approximately 0.04. At this redshift, 1 kpc corresponds to approximately 1.26 arcsec, which is approximately the size of half of the MaNGA PSF. When the spatial resolution is poor, the central mass density peak becomes diluted by the lower-density surrounding regions, leading to an underestimation of the central density. This finding supports our hypothesis.

To further validate this hypothesis, we utilized SDSS imaging data from the NSA catalog([15]), which offers better spatial resolution with a typical full width at half maximum (FWHM) of approximately 1.3 arcsec. With this improved FWHM, we can resolve the central regions of galaxies more effectively than with MaNGA data alone. To ensure that our galaxies are adequately resolved in the center, free from the effects of beam smearing, we selected galaxies that are both large in size and nearby. Specifically, we imposed criteria of redshift $z < 0.02$ and stellar mass $M_* > 10.5$. While we do not have the Σ_1 measurements for these galaxies, we estimate their central mass by calculating the *i*-band absolute magnitude within a 1 kpc aperture. We then plot this *i*-band magnitude against the mass of the galaxies. If the ‘downturn’ observed in the MaNGA data is genuine and attributed to new physics, we should observe a similar turn in this plot using the higher-resolution imaging data.

Figure 8 displays the *i*-band magnitude (mag1) versus stellar mass (M_*) for the selected sample from the NSA catalog. This figure provides strong evidence that the ‘downturn’ observed in Figures 5.6 and 5.5 is indeed due to beam smearing. Notably, the downturn at $\log_{10} M_*/M_\odot \sim 10.7$ is no longer present. The mag1 continues to increase until accurate statistics cannot be obtained due to a limited number of galaxies.

Figure 8 supports our conclusion that the observed downturn in the Σ_1 versus mass plot is a result of the beam-smearing effect. The utilization of higher-resolution imaging data helps eliminate this artificial feature, providing further insights into the true nature of the galaxies under investigation.

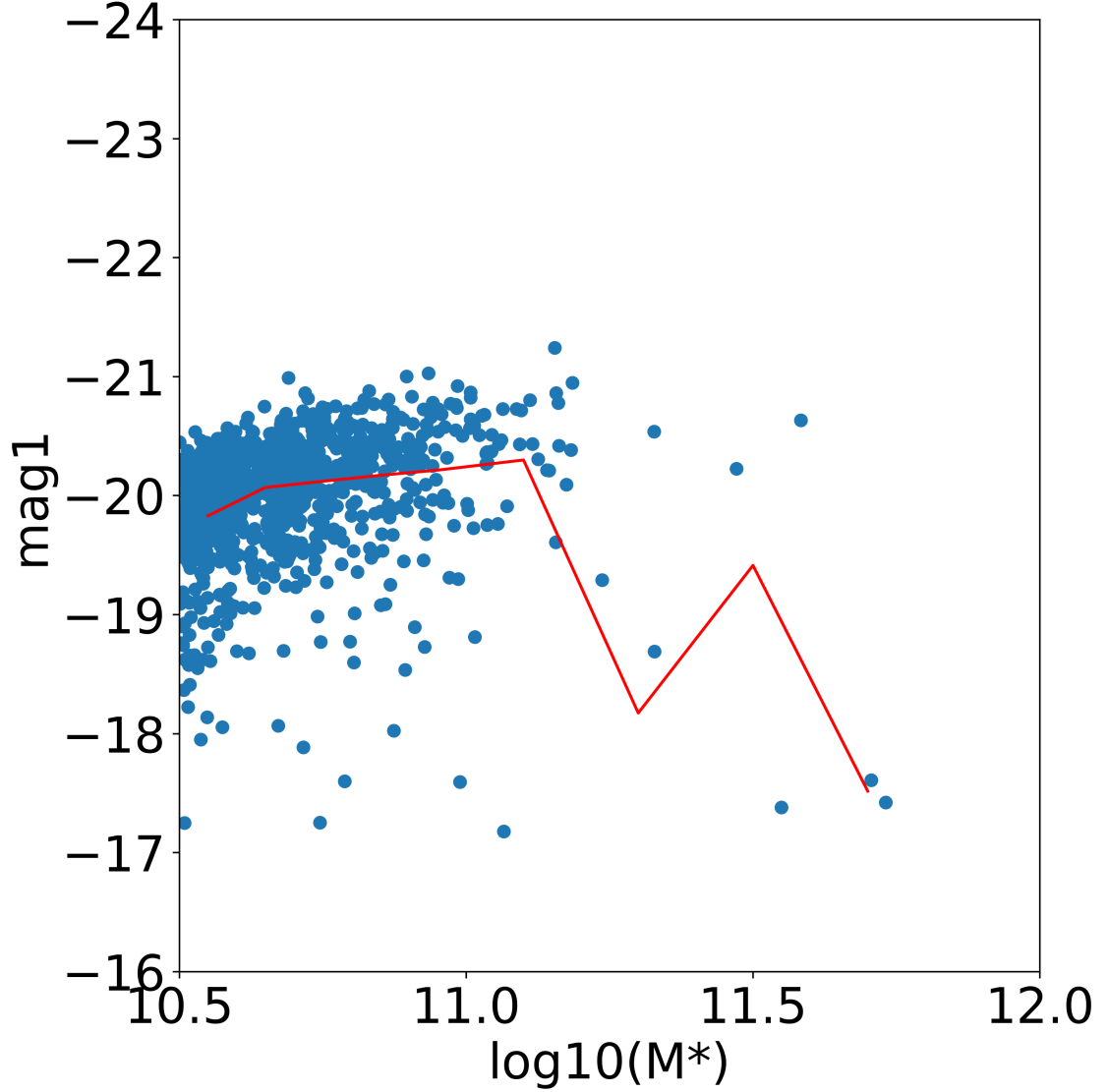


Figure C1: mass-magnitude plot with NSA data. The horizontal axis(x) is the 10-based log of total stellar mass, while the vertical axis(y) is the mag1 , which is the i -band absolute magnitude within 1kpc aperture.

Appendix D: Stellar population results from pPXF for different mass bins

C-SF galaxies

For C-SF galaxies, we examine their properties across different mass bins to gain insights into their characteristics. The mass bins are defined as follows: [8,9], [9,10], [10,11], [11,12]. We analyze the central region and the outskirts of these galaxies within each mass bin and present the corresponding results below.

Center of C-SF galaxies

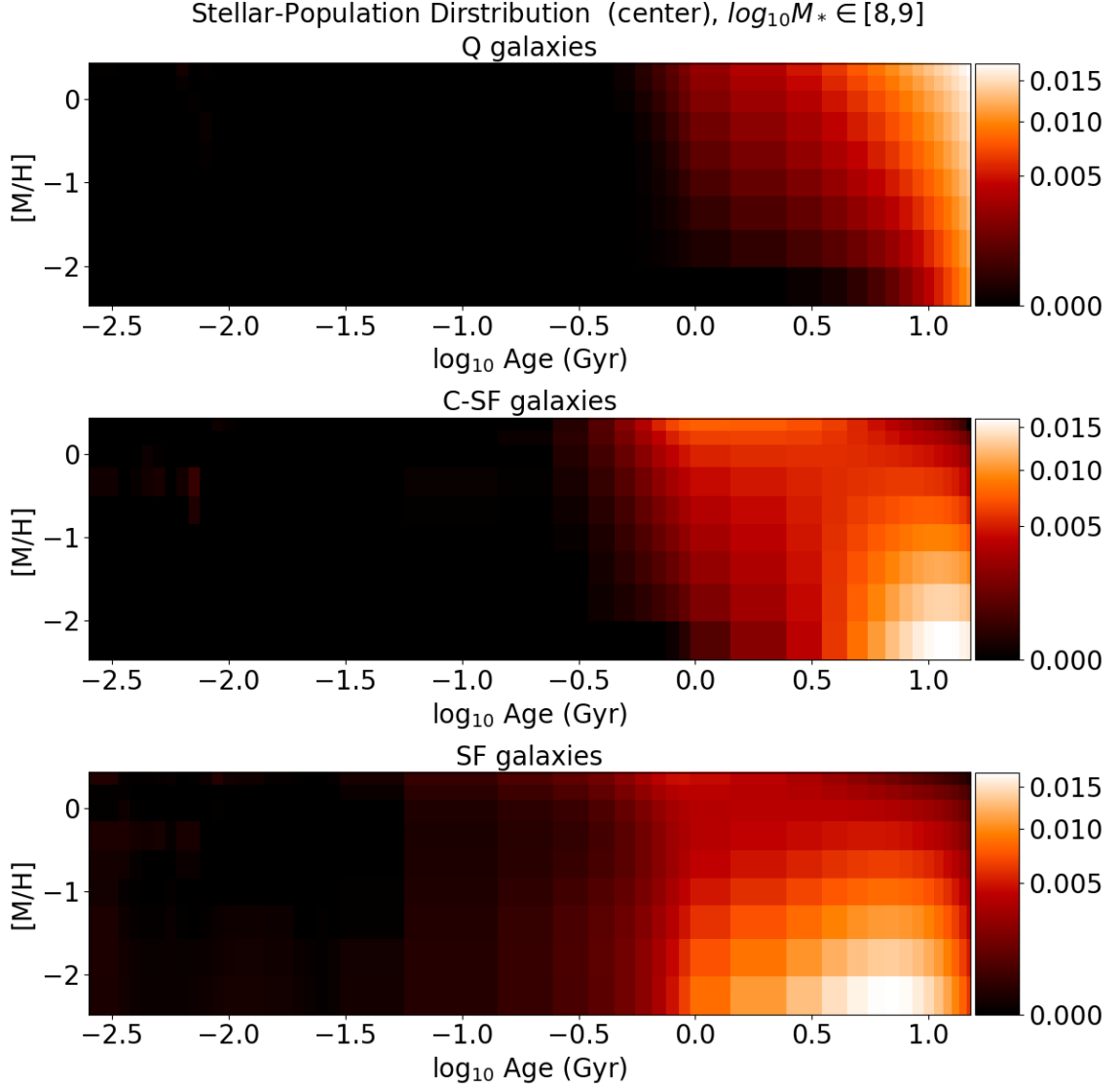


Figure D1: This figure presents the pPXF analysis results for central-star-forming (C-SF) galaxies with stellar mass $\log_{10} M_*$ ranging from 8 to 9. The plot setup and visual representation are identical to Figure 5.9, which provides a comparison and consistent format for ease of interpretation.

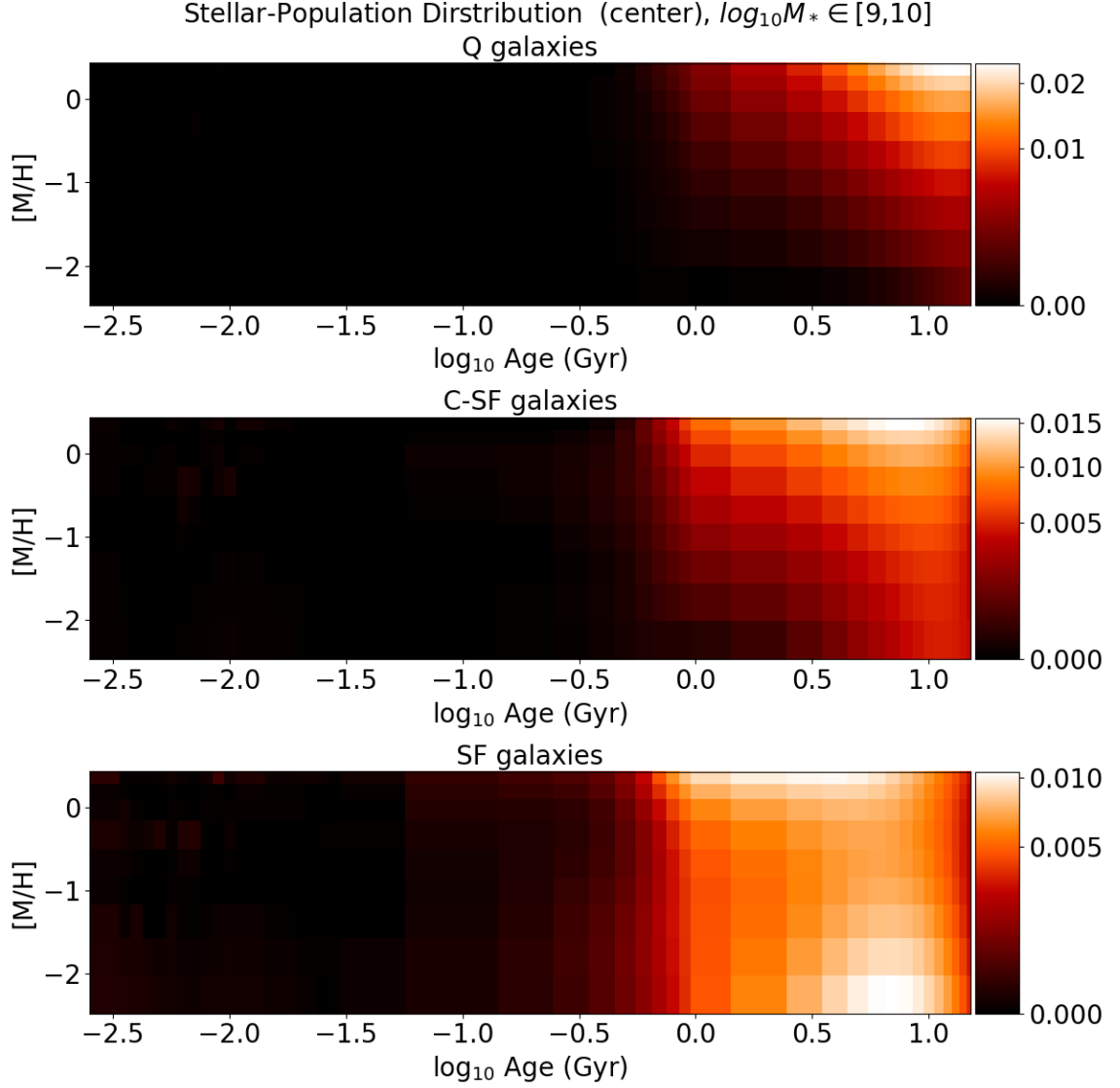


Figure D2: This figure presents the pPXF analysis results for central-star-forming (C-SF) galaxies with stellar mass $\log_{10} M_*$ ranging from 9 to 10. The plot setup and visual representation are identical to Figure 5.9, which provides a comparison and consistent format for ease of interpretation.

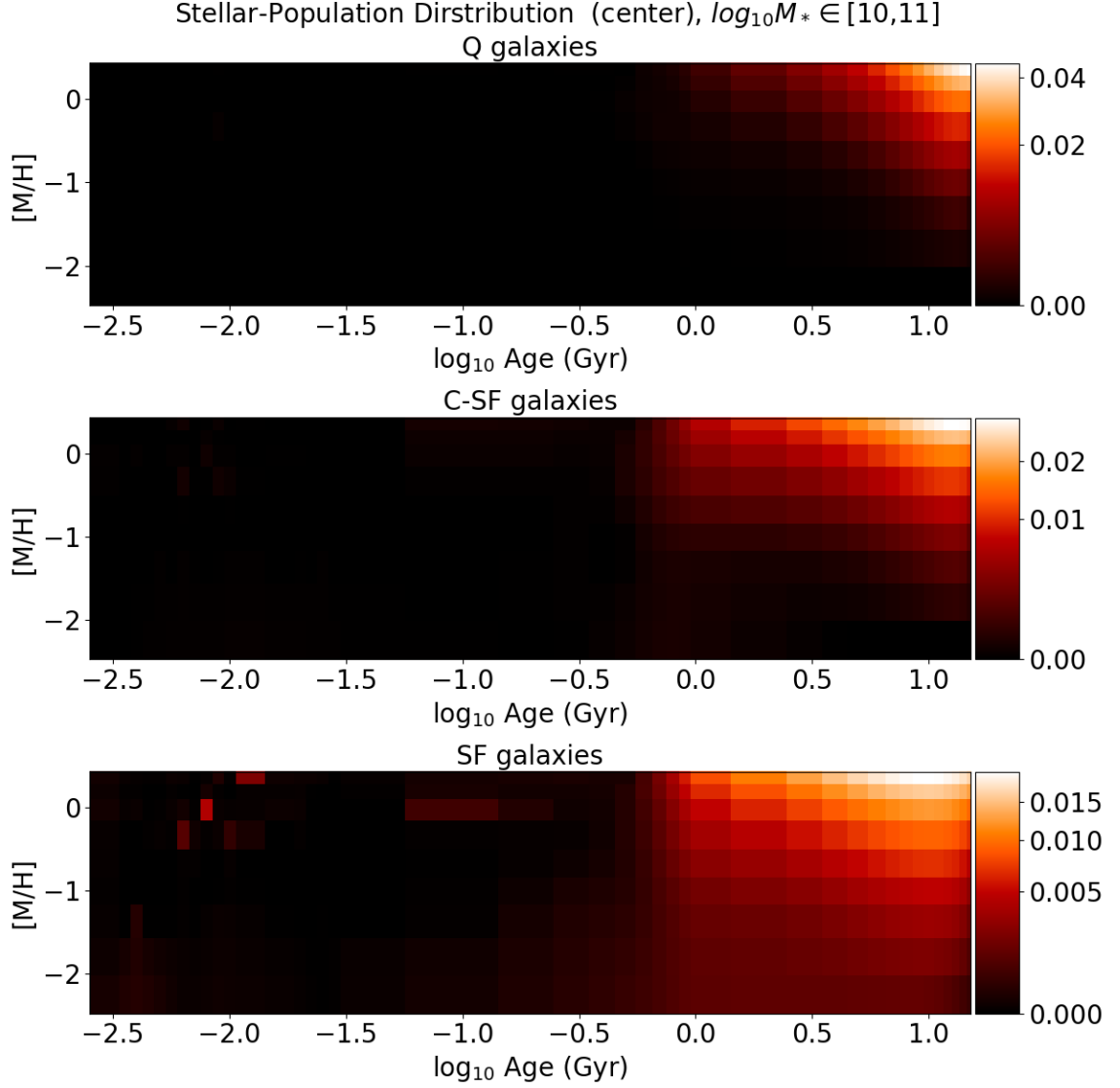


Figure D3: This figure presents the pPXF analysis results for central-star-forming (C-SF) galaxies with stellar mass $\log_{10} M_*$ ranging from 10 to 11. The plot setup and visual representation are identical to Figure 5.9, which provides a comparison and consistent format for ease of interpretation.

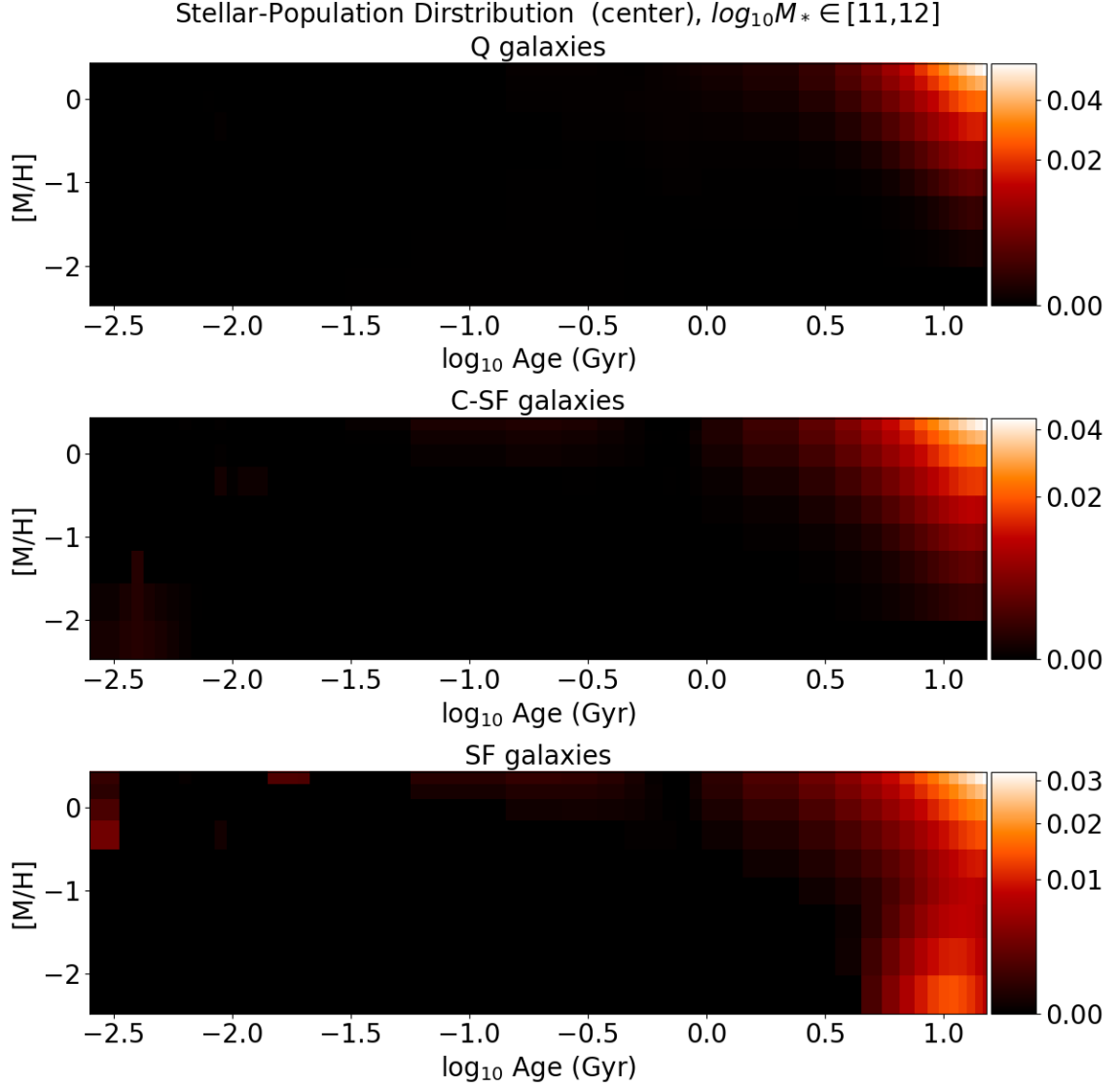


Figure D4: This figure presents the pPXF analysis results for central-star-forming (C-SF) galaxies with stellar mass $\log_{10} M_*$ ranging from 11 to 12. The plot setup and visual representation are identical to Figure 5.9, which provides a comparison and consistent format for ease of interpretation.

Outskirts of C-SF galaxies

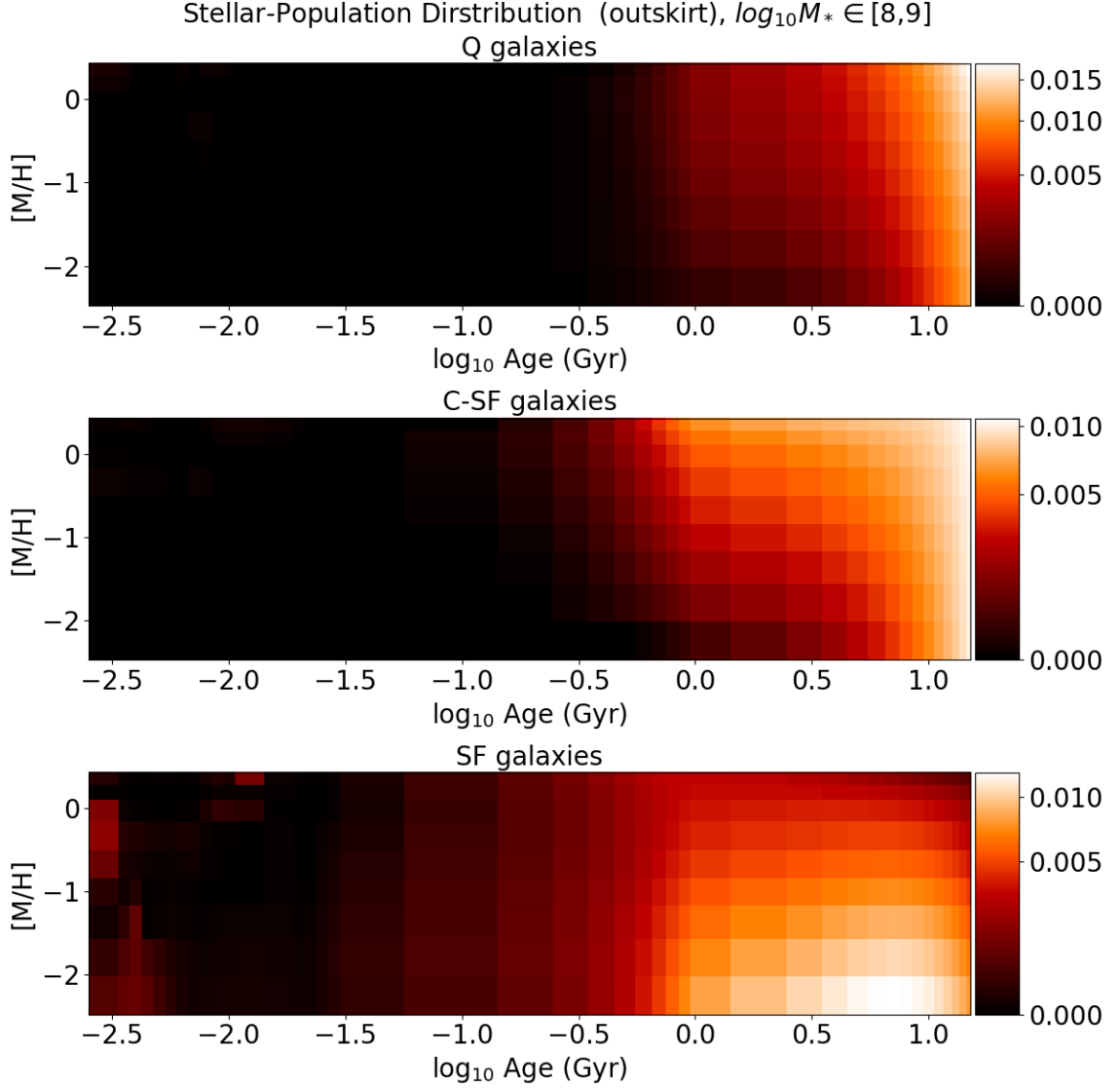


Figure D5: This figure presents the pPXF analysis results for central-star-forming (C-SF) galaxies with stellar mass $\log_{10} M_*$ ranging from 8 to 9. The plot setup and visual representation are identical to Figure 5.11, which provides a comparison and consistent format for ease of interpretation.

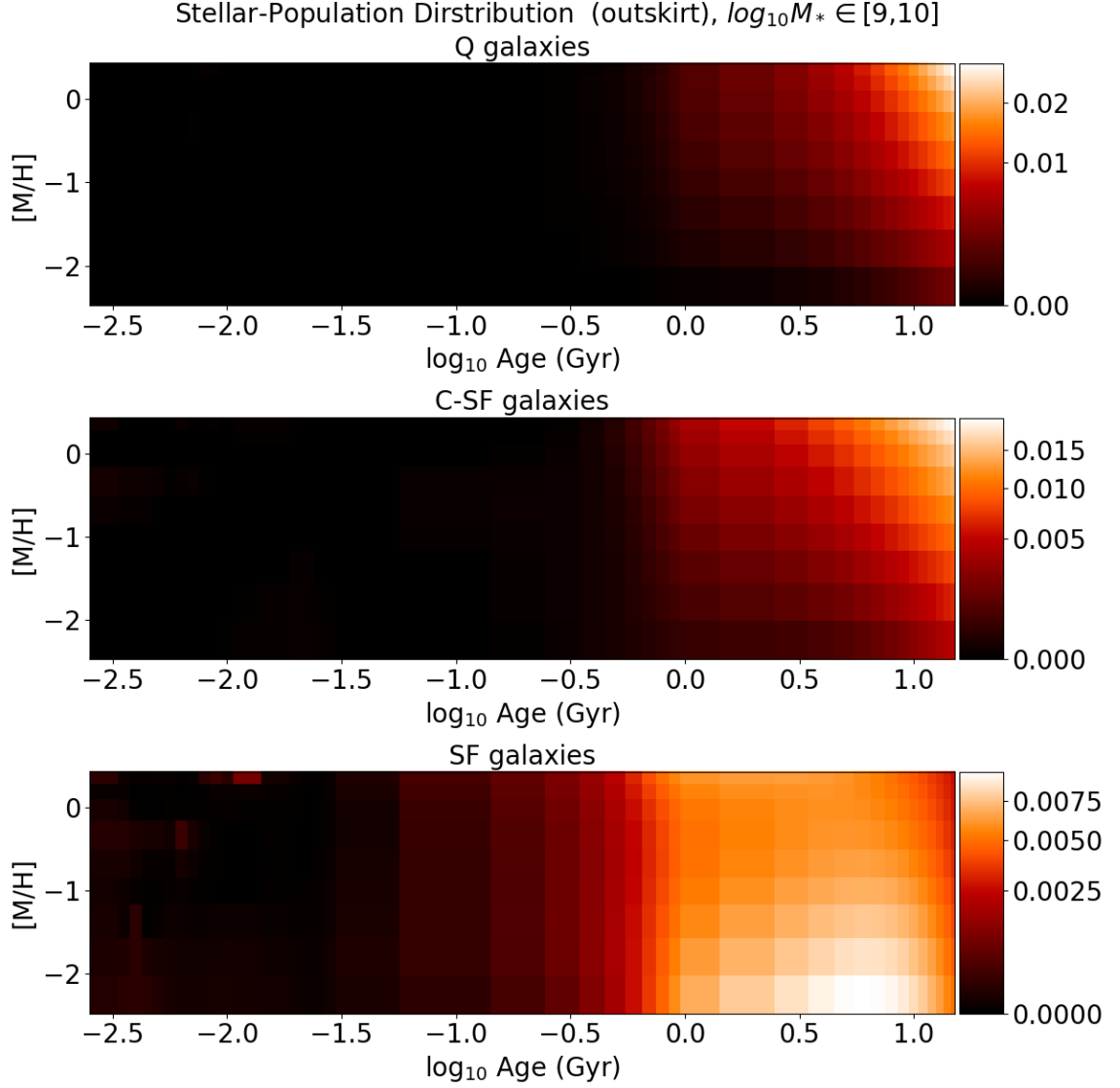


Figure D6: This figure presents the pPXF analysis results for central-star-forming (C-SF) galaxies with stellar mass $\log_{10} M_*$ ranging from 9 to 10. The plot setup and visual representation are identical to Figure 5.11, which provides a comparison and consistent format for ease of interpretation.

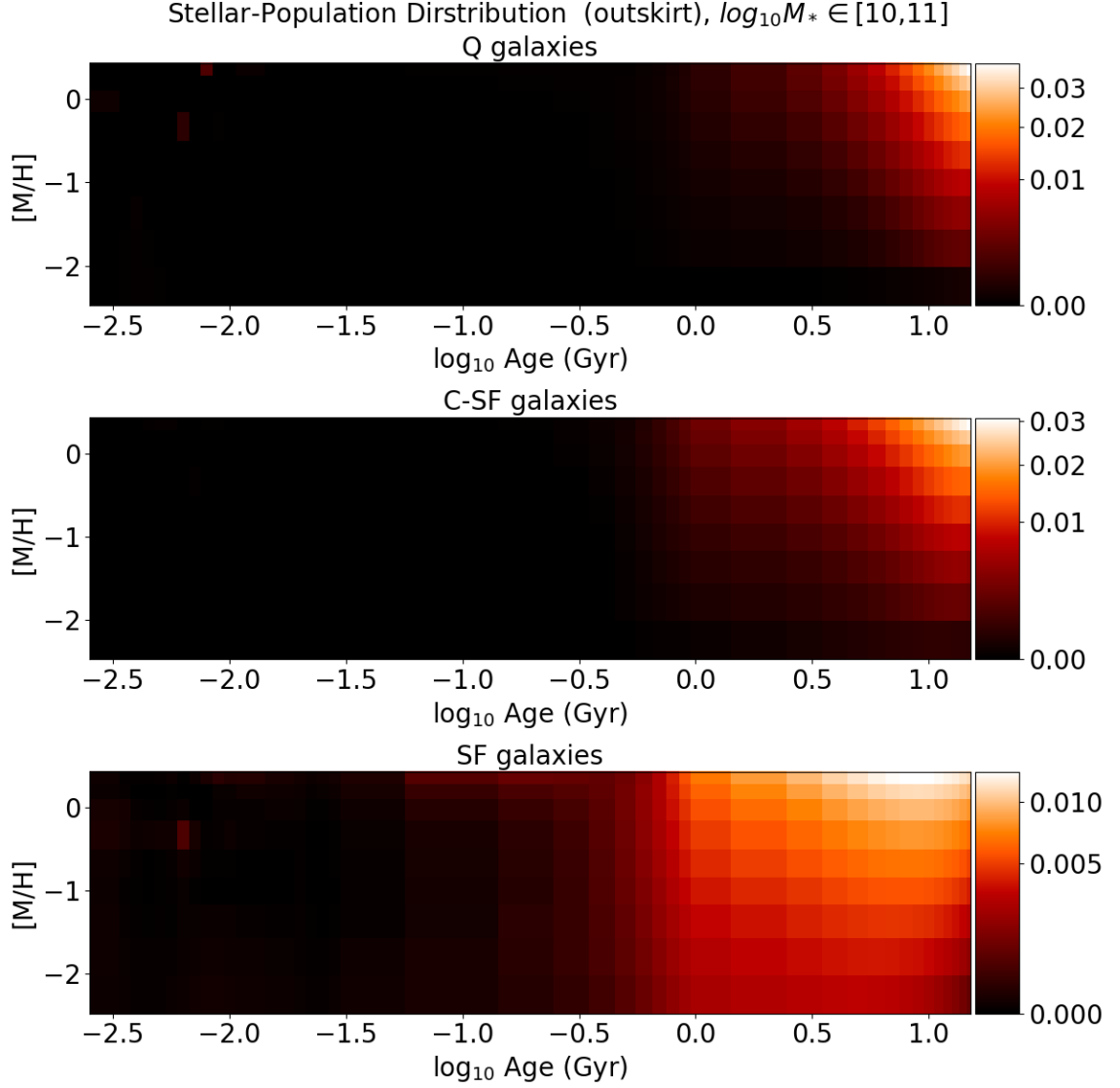


Figure D7: This figure presents the pPXF analysis results for central-star-forming (C-SF) galaxies with stellar mass $\log_{10} M_*$ ranging from 10 to 11. The plot setup and visual representation are identical to Figure 5.11, which provides a comparison and consistent format for ease of interpretation.

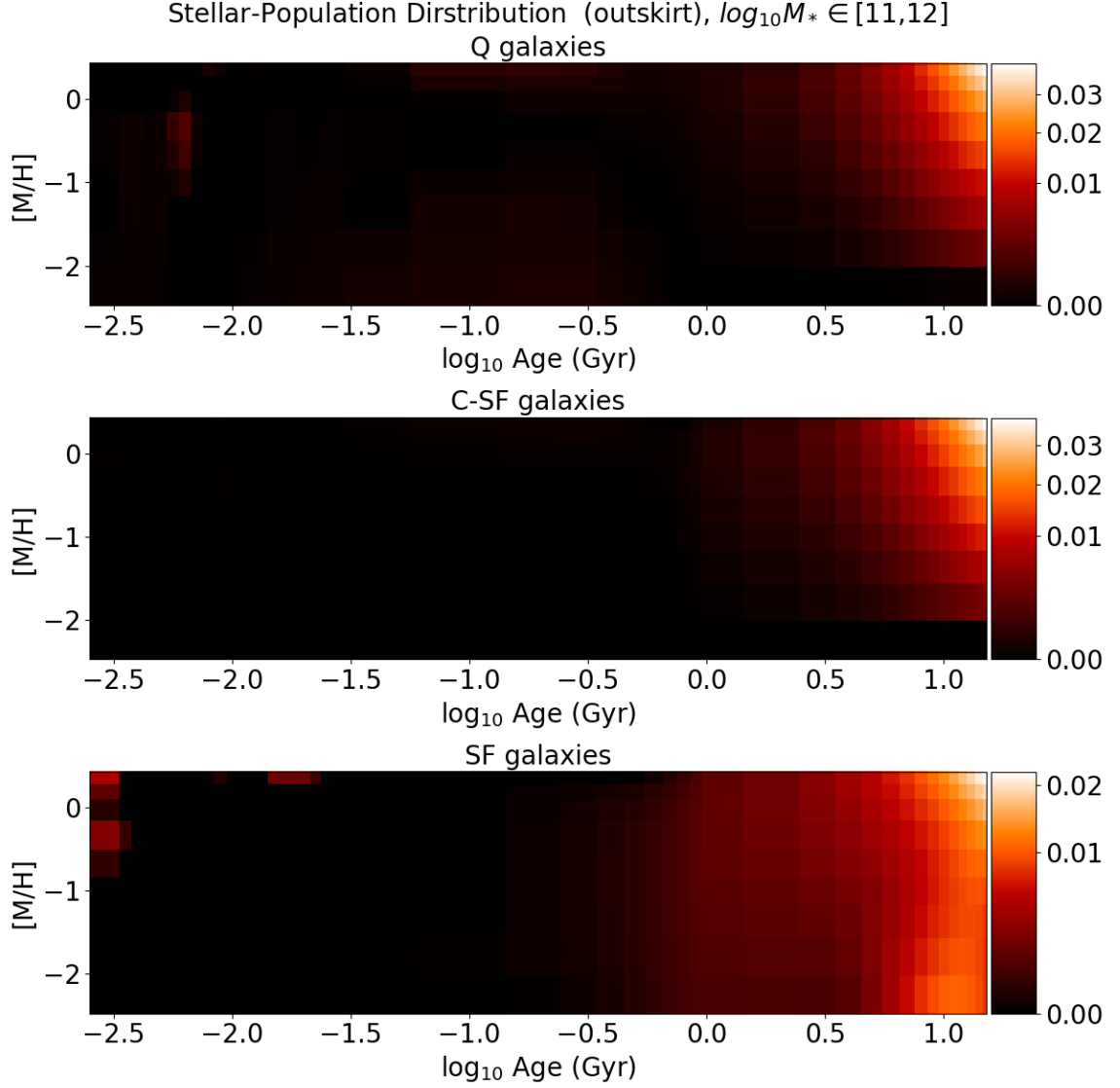


Figure D8: This figure presents the pPXF analysis results for central-star-forming (C-SF) galaxies with stellar mass $\log_{10} M_*$ ranging from 11 to 12. The plot setup and visual representation are identical to Figure 5.11, which provides a comparison and consistent format for ease of interpretation.

C-Q galaxies

For C-Q galaxies, since most of C-Q galaxies have a stellar mass $\log_{10} M_*$ ranging from 10 to 11.5, we defined the mass ranges as follows: $[10, 10.5]$, $[10.5, 11]$, $[11, 11.5]$. We analyze the central region and the outskirts of these galaxies within each mass bin and present the corresponding results below.

Center of C-Q galaxies

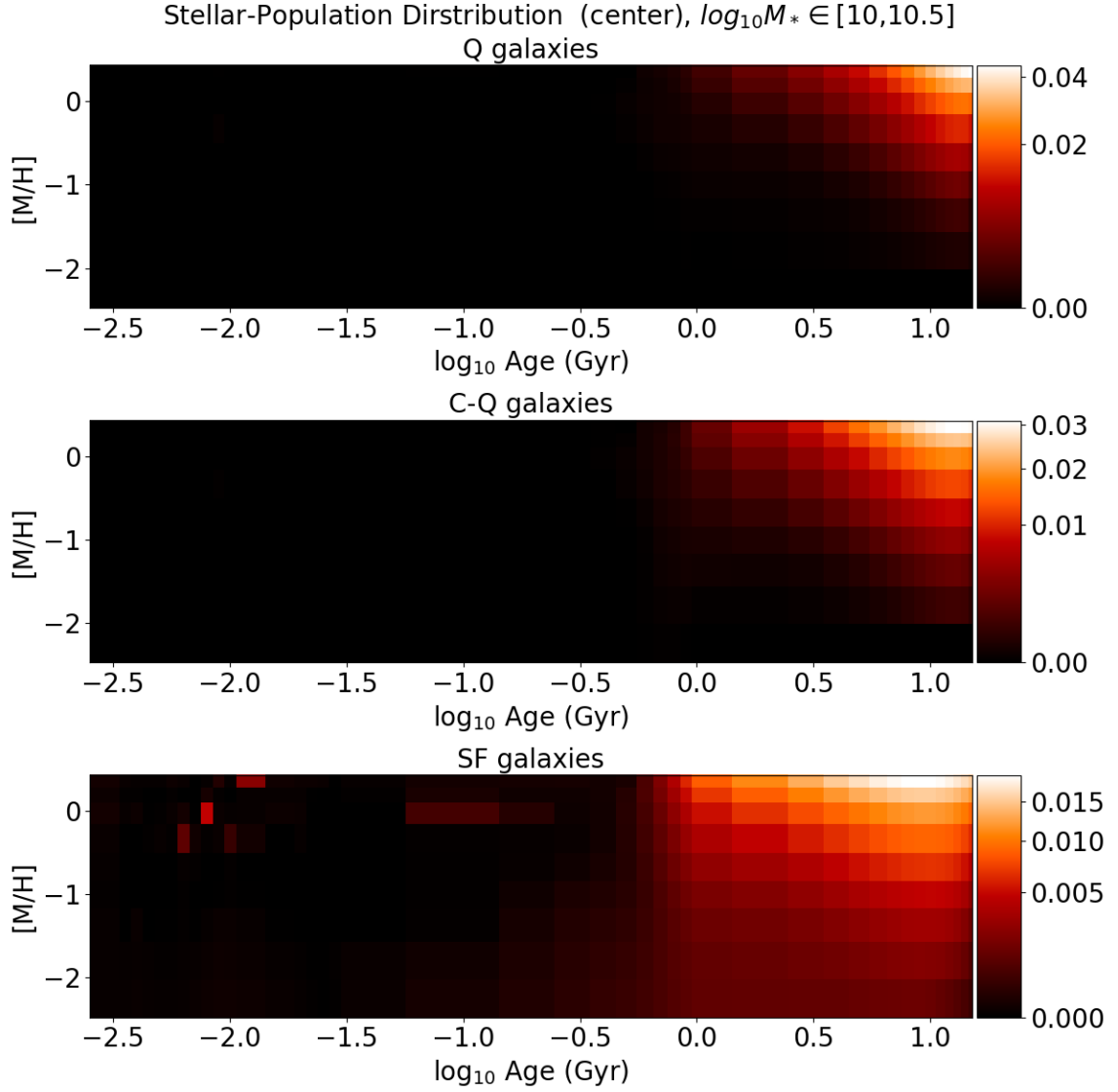


Figure D9: This figure presents the pPXF analysis results for central-quiescent (C-Q) galaxies with stellar mass $\log_{10} M_*$ ranging from 10 to 10.5. The plot setup and visual representation are identical to Figure 5.8, which provides a comparison and consistent format for ease of interpretation.

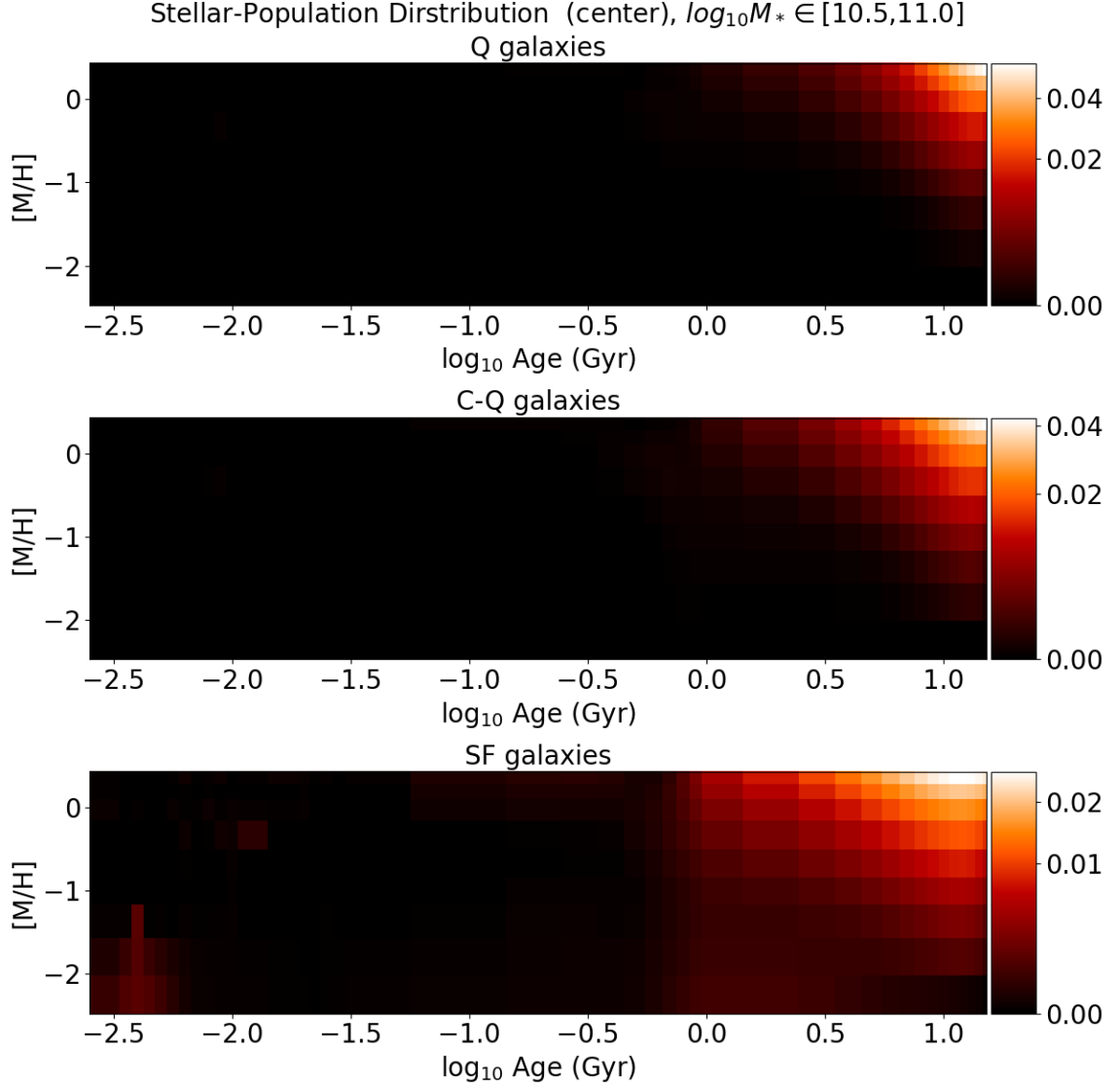


Figure D10: This figure presents the pPXF analysis results for central-quiescent (C-Q) galaxies with stellar mass $\log_{10} M_*$ ranging from 10.5 to 11. The plot setup and visual representation are identical to Figure 5.8, which provides a comparison and consistent format for ease of interpretation.

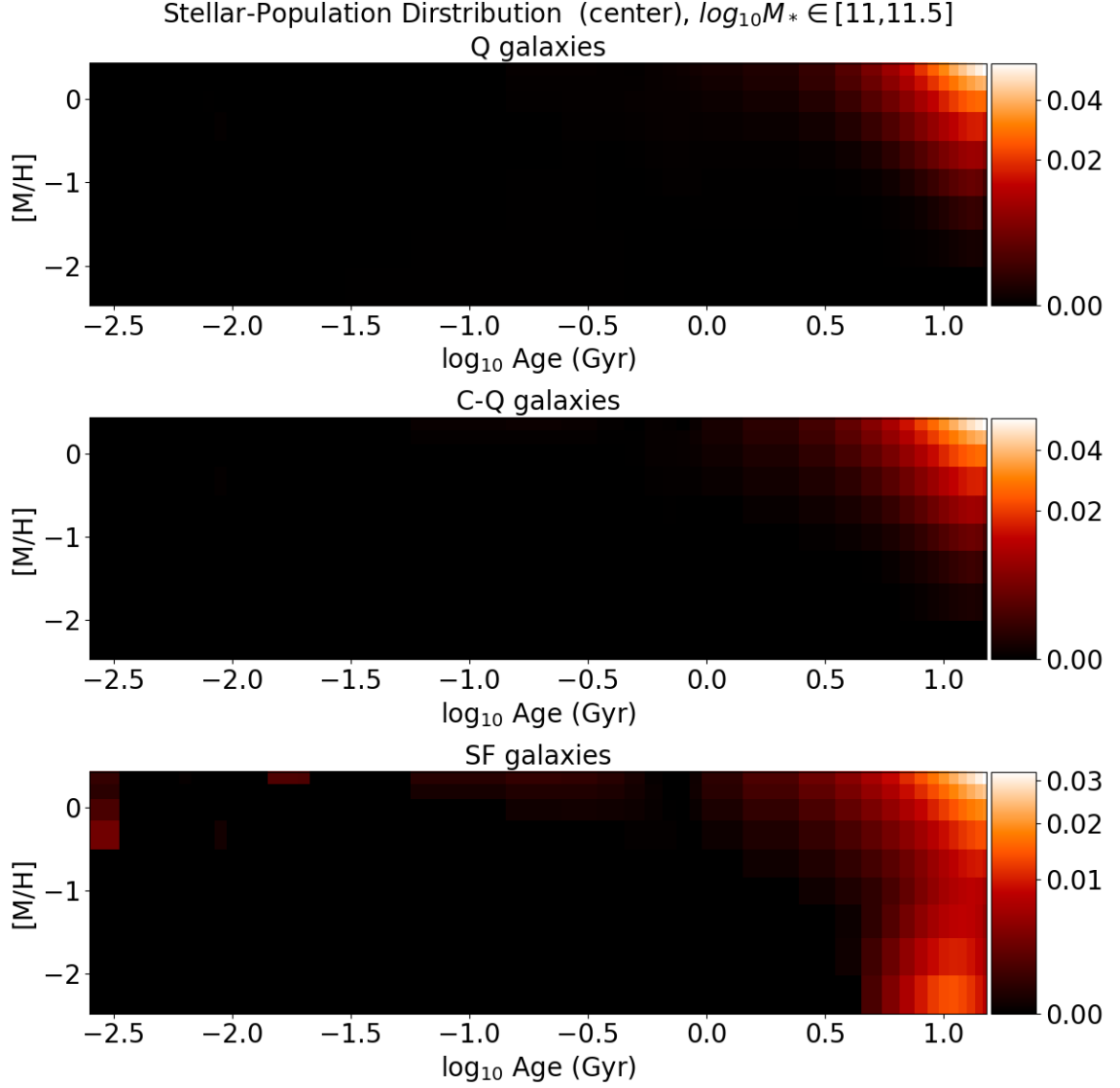


Figure D11: This figure presents the pPXF analysis results for central-quiescent (C-Q) galaxies with stellar mass $\log_{10} M_*$ ranging from 11 to 11.5. The plot setup and visual representation are identical to Figure 5.8, which provides a comparison and consistent format for ease of interpretation.

Center of C-Q galaxies

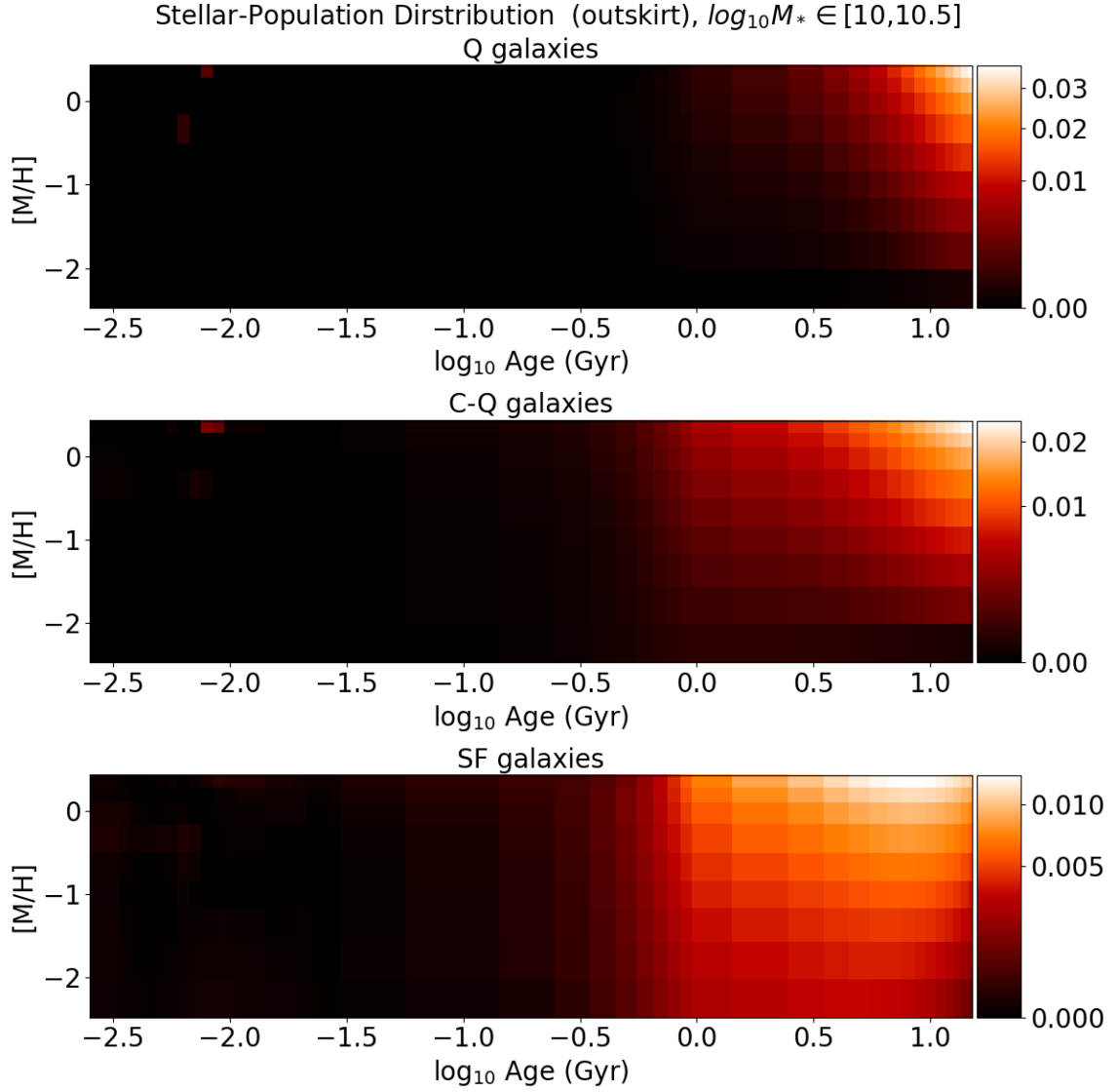


Figure D12: This figure presents the pPXF analysis results for central-quiescent (C-Q) galaxies with stellar mass $\log_{10} M_*$ ranging from 10 to 10.5. The plot setup and visual representation are identical to Figure 5.10, which provides a comparison and consistent format for ease of interpretation.

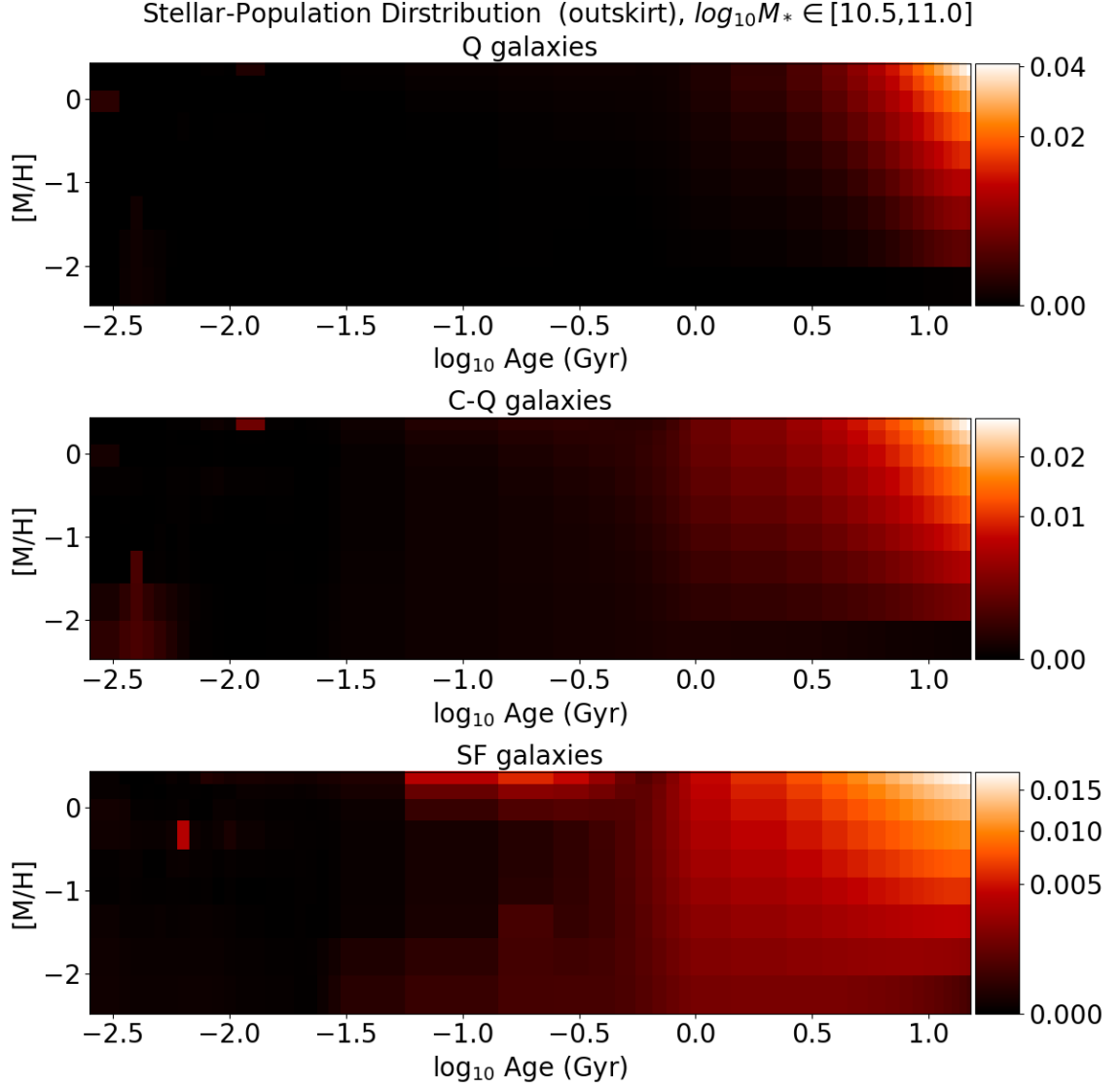


Figure D13: This figure presents the pPXF analysis results for central-quiescent (C-Q) galaxies with stellar mass $\log_{10} M_*$ ranging from 10.5 to 11. The plot setup and visual representation are identical to Figure 5.10, which provides a comparison and consistent format for ease of interpretation.

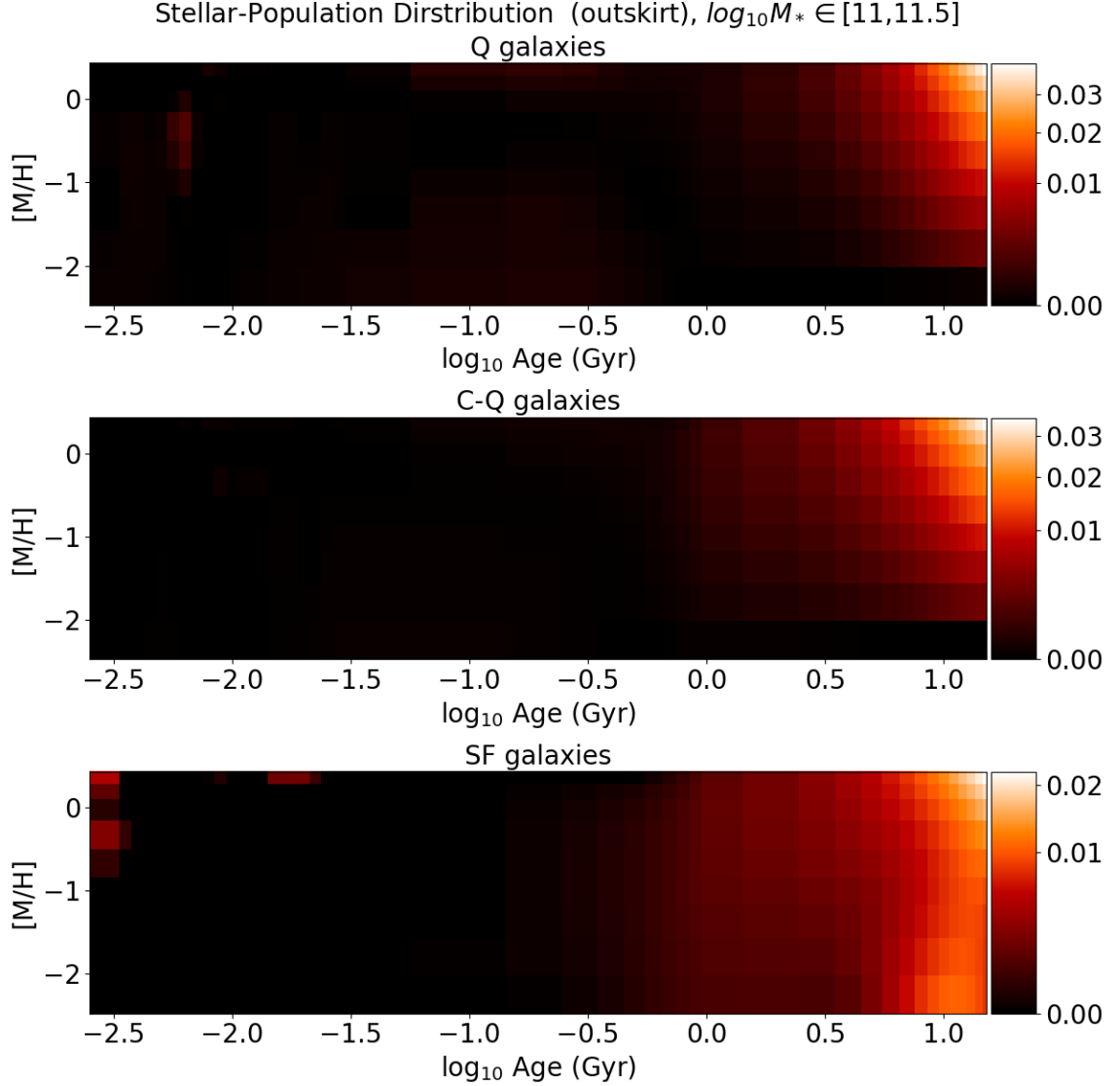


Figure D14: This figure presents the pPXF analysis results for central-quiescent (C-Q) galaxies with stellar mass $\log_{10} M_*$ ranging from 11 to 11.5. The plot setup and visual representation are identical to Figure 5.10, which provides a comparison and consistent format for ease of interpretation.

Appendix E: Demonstration of $H\alpha$ surface brightness

This section presents the $H\alpha$ surface brightness profiles for each individual galaxy that meets our selection criteria. Our selection rules include choosing galaxies from the AGN sample, specifically those classified as SF+SF, C-Q+SF, C-Q+C-Q, and C-Q+Q-Ring AGNs. Additionally, we restrict the selection to galaxies with an axis ratio (b/a) greater than 0.717.

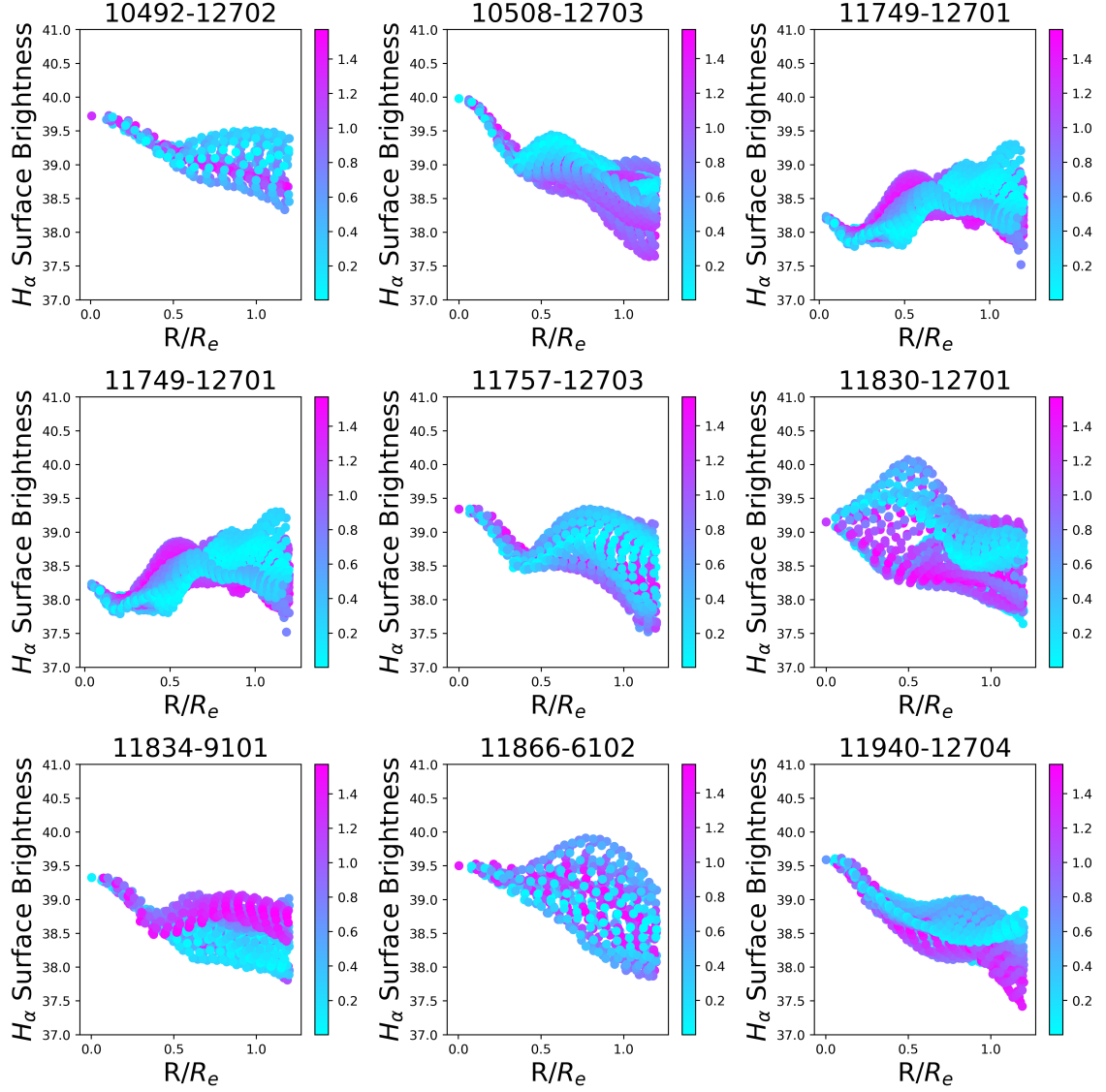


Figure E1: This figure displays the $H\alpha$ surface brightness profile for nine different galaxies, with each panel labeled by the corresponding MaNGA plate-IFU number. The y-axis represents the $H\alpha$ surface brightness, while the x-axis corresponds to the radius normalized by R_e . The color bar indicates the angle away from the major axis, with 0 representing points on the major axis and $\pi/2$ representing points on the minor axis.

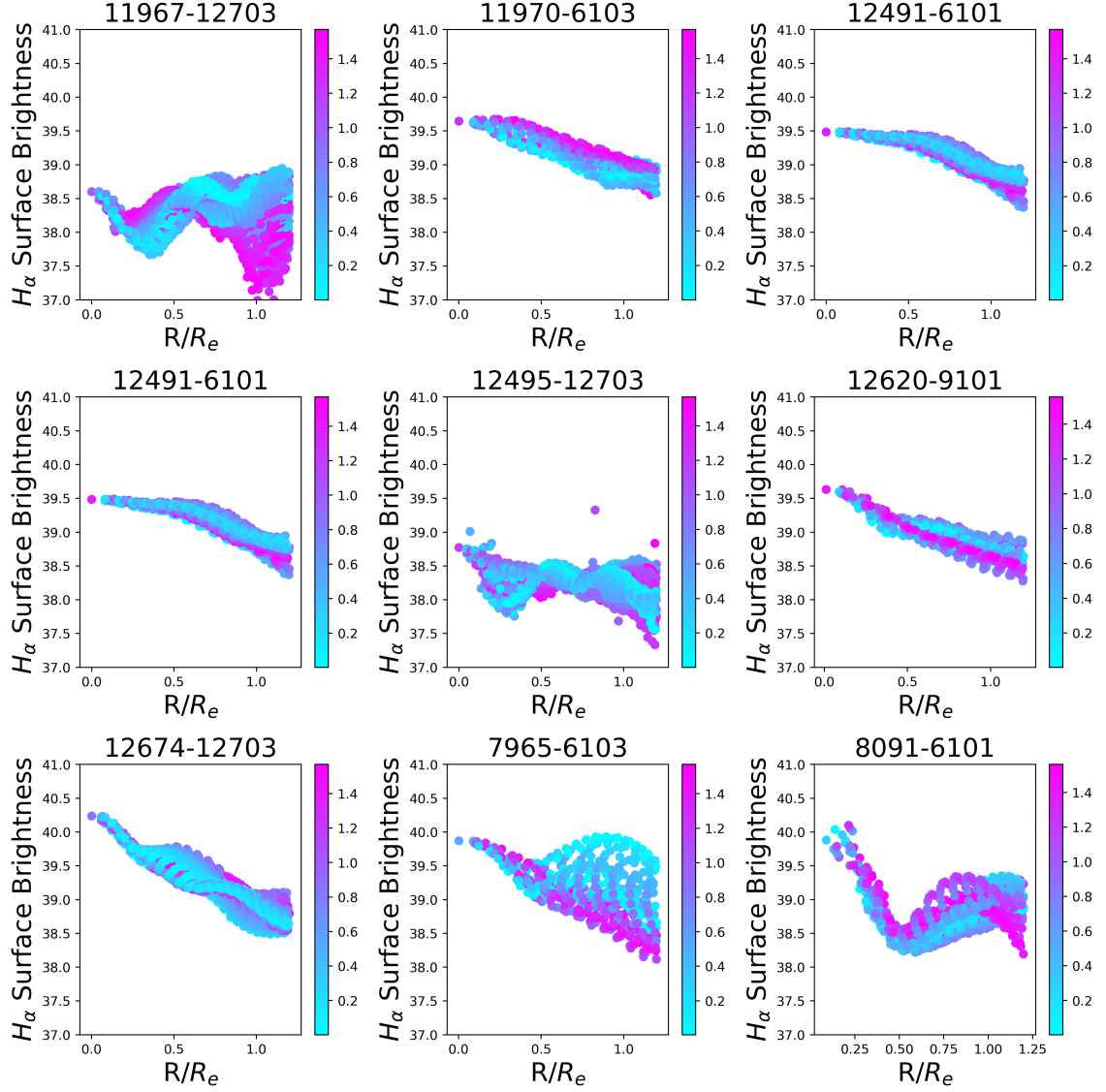


Figure E2: This figure displays the $H\alpha$ surface brightness profile for nine different galaxies, with each panel labeled by the corresponding MaNGA plate-IFU number. The y-axis represents the $H\alpha$ surface brightness, while the x-axis corresponds to the radius normalized by R_e . The color bar indicates the angle away from the major axis, with 0 representing points on the major axis and $\pi/2$ representing points on the minor axis.

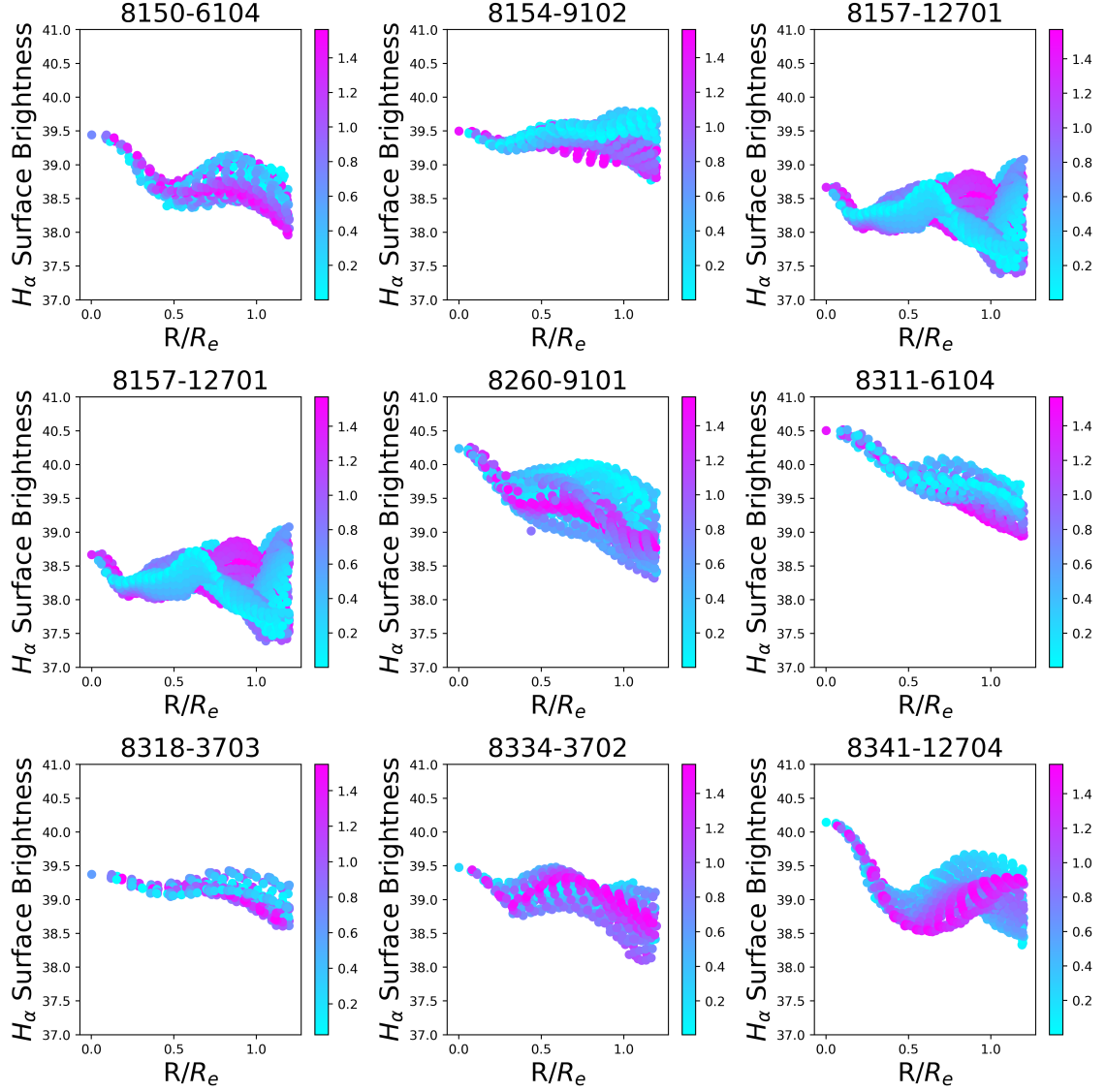


Figure E3: This figure displays the $H\alpha$ surface brightness profile for nine different galaxies, with each panel labeled by the corresponding MaNGA plate-IFU number. The y-axis represents the $H\alpha$ surface brightness, while the x-axis corresponds to the radius normalized by R_e . The color bar indicates the angle away from the major axis, with 0 representing points on the major axis and $\pi/2$ representing points on the minor axis.

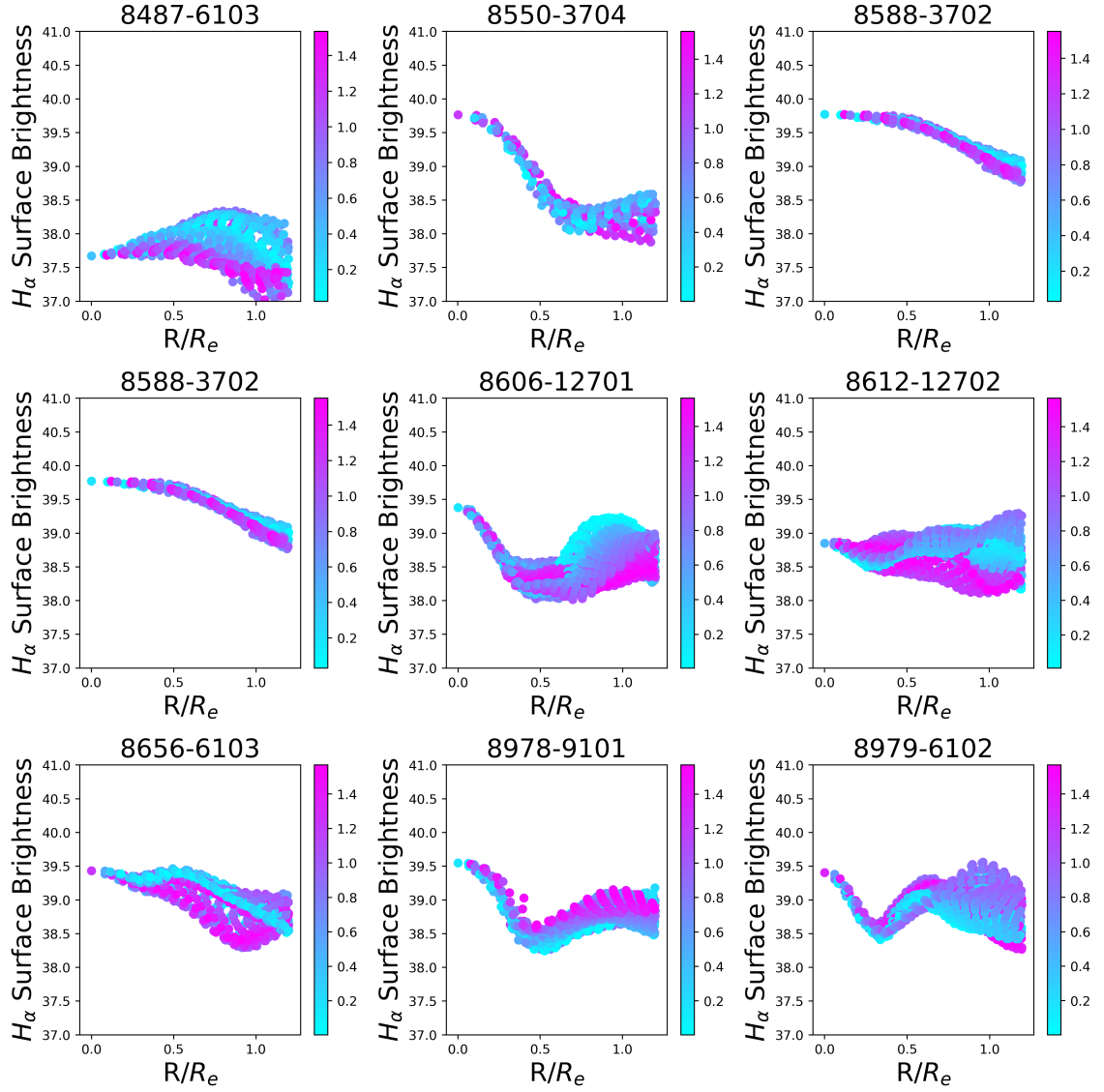


Figure E4: This figure displays the $H\alpha$ surface brightness profile for nine different galaxies, with each panel labeled by the corresponding MaNGA plate-IFU number. The y-axis represents the $H\alpha$ surface brightness, while the x-axis corresponds to the radius normalized by R_e . The color bar indicates the angle away from the major axis, with 0 representing points on the major axis and $\pi/2$ representing points on the minor axis.

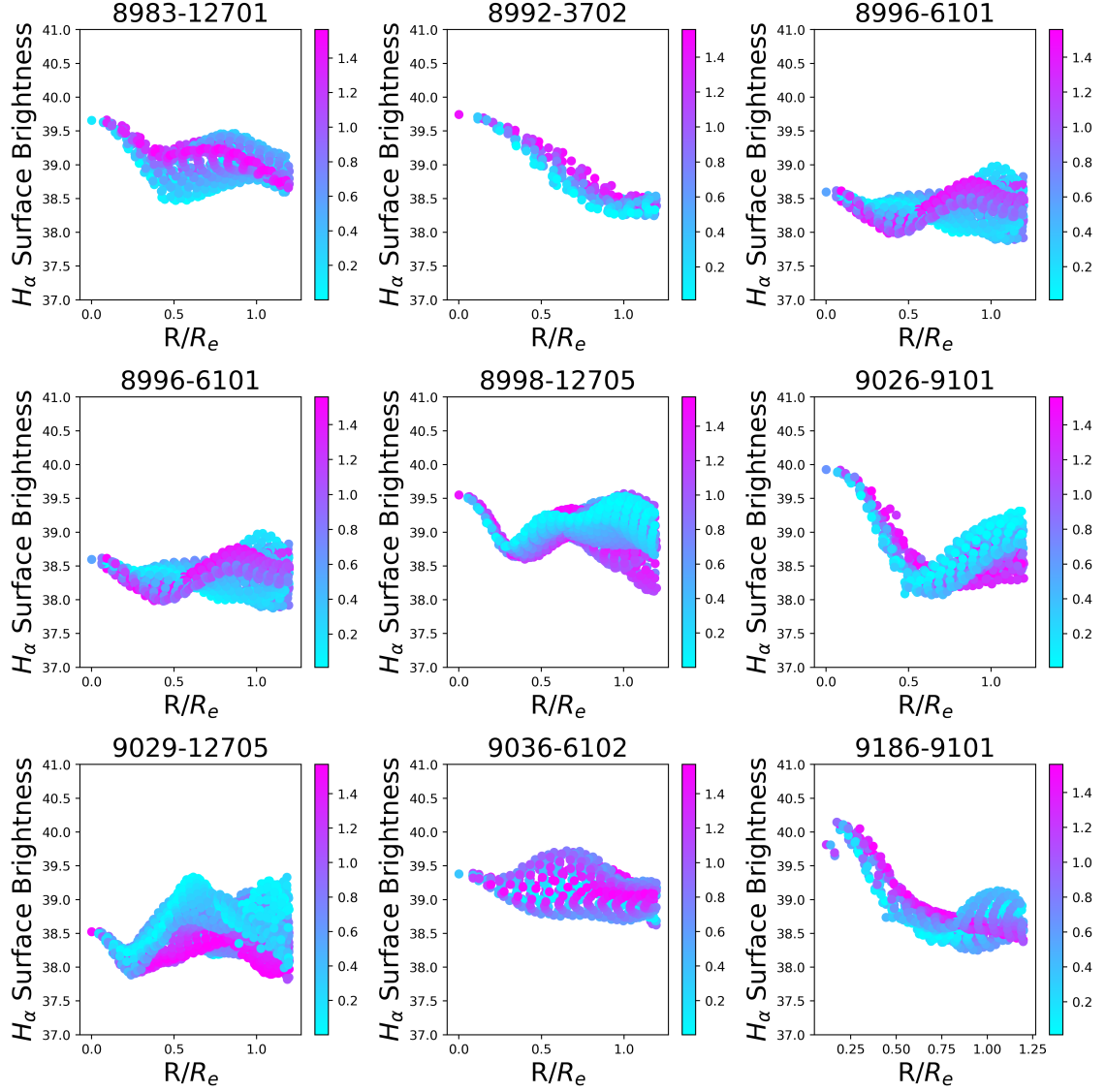


Figure E5: This figure displays the $H\alpha$ surface brightness profile for nine different galaxies, with each panel labeled by the corresponding MaNGA plate-IFU number. The y-axis represents the $H\alpha$ surface brightness, while the x-axis corresponds to the radius normalized by R_e . The color bar indicates the angle away from the major axis, with 0 representing points on the major axis and $\pi/2$ representing points on the minor axis.

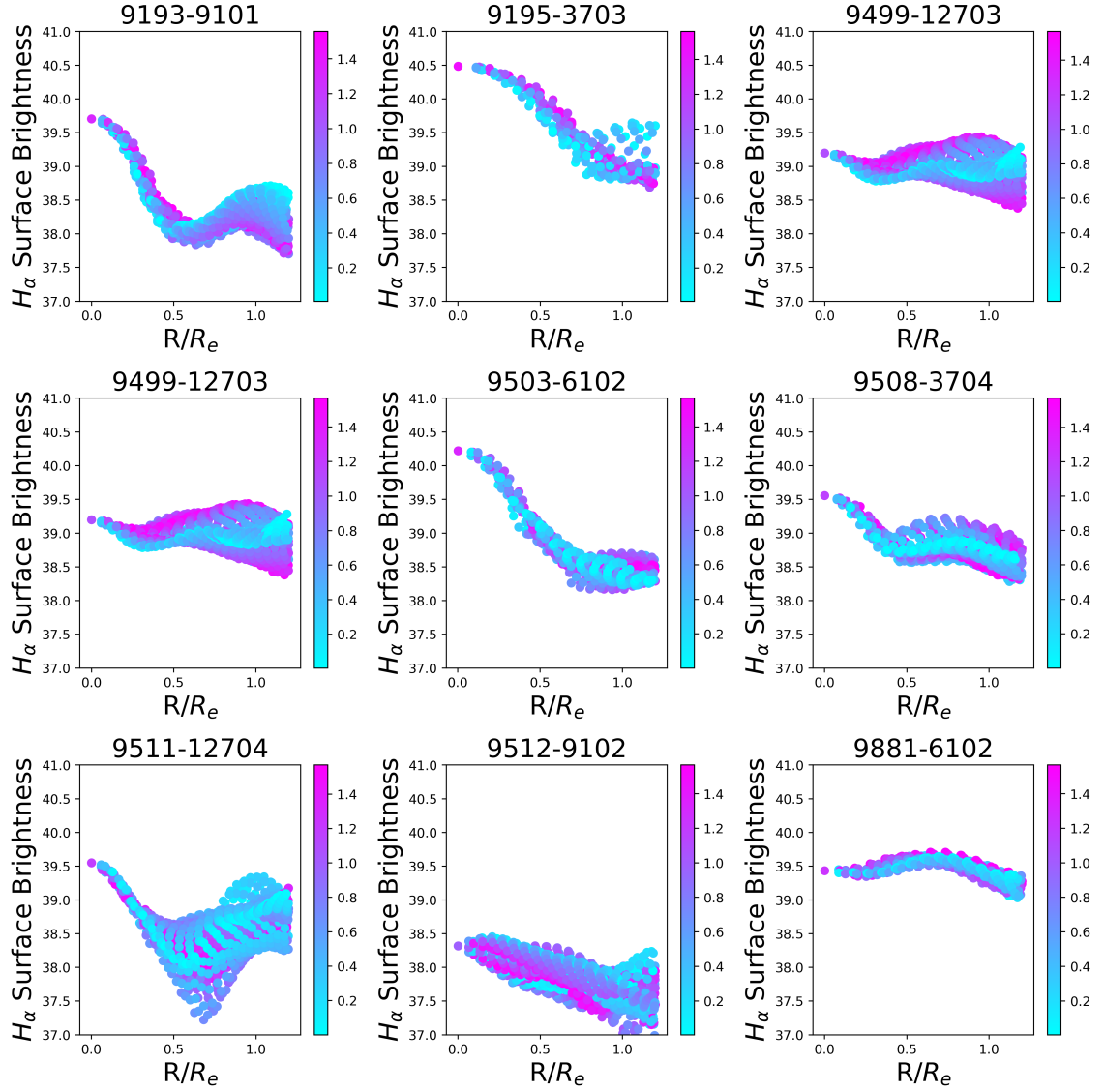


Figure E6: This figure displays the H_α surface brightness profile for nine different galaxies, with each panel labeled by the corresponding MaNGA plate-IFU number. The y-axis represents the H_α surface brightness, while the x-axis corresponds to the radius normalized by R_e . The color bar indicates the angle away from the major axis, with 0 representing points on the major axis and $\pi/2$ representing points on the minor axis.

Bibliography

- [1] Abdurro'uf, K. Accetta, C. Aerts, V. Silva Aguirre, R. Ahumada, N. Ajgaonkar, N. Filiz Ak, S. Alam, C. Allende Prieto, A. Almeida, F. Anders, S. F. Anderson, B. H. Andrews, B. Anguiano, E. Aquino-Ortíz, A. Aragón-Salamanca, M. Argudo-Fernández, M. Ata, M. Aubert, V. Avila-Reese, C. Badenes, R. H. Barbá, K. Barger, J. K. Barrera-Ballesteros, R. L. Beaton, T. C. Beers, F. Belfiore, C. F. Bender, M. Bernardi, M. A. Bershad, F. Beutler, C. M. Bidin, J. C. Bird, D. Bizyaev, G. A. Blanc, M. R. Blanton, N. F. Boardman, A. S. Bolton, M. Boquien, J. Borissova, J. Bovy, W. N. Brandt, J. Brown, J. R. Brownstein, M. Brusa, J. Buchner, K. Bundy, J. N. Burchett, M. Bureau, A. Burgasser, T. K. Cabang, S. Campbell, M. Cappellari, J. K. Carlberg, F. C. Wanderley, R. Carrera, J. Cash, Y.-P. Chen, W.-H. Chen, B. Cherinka, C. Chiappini, P. D. Choi, S. D. Chojnowski, H. Chung, N. Clerc, R. E. Cohen, J. M. Comerford, J. Comparat, L. da Costa, K. Covey, J. D. Crane, I. Cruz-Gonzalez, C. Culhane, K. Cunha, Y. S. Dai, G. Damke, J. Darling, J. Davidson, James W., R. Davies, K. Dawson, N. De Lee, A. M. Diamond-Stanic, M. Cano-Díaz, H. D. Sánchez, J. Donor, C. Duckworth, T. Dwelly, D. J. Eisenstein, Y. P. Elsworth, E. Emsellem, M. Eracleous, S. Escoffier, X. Fan, E. Farr, S. Feng, J. G. Fernández-Trincado, D. Feuillet, A. Filipp, S. P. Fillingham, P. M. Frinchaboy, S. Fromenteau, L. Galbany, R. A. García, D. A. García-Hernández, J. Ge, D. Geisler, J. Gelfand, T. Géron, B. J. Gibson, J. Goddy, D. Godoy-Rivera, K. Grabowski, P. J. Green, M. Greener, C. J. Grier, E. Griffith, H. Guo, J. Guy, M. Hadjara, P. Harding, S. Hasselquist, C. R. Hayes, F. Hearty, J. Hernández, L. Hill, D. W. Hogg, J. A. Holtzman, D. Horta, B.-C. Hsieh, C.-H. Hsu, Y.-H. Hsu, D. Huber, M. Huertas-Company, B. Hutchinson, H. S. Hwang, H. J. Ibarra-Medel, J. I. Chitham, G. S. Ilha, J. Imig, W. Jaekle, T. Jayasinghe, X. Ji, J. A. Johnson, A. Jones, H. Jönsson, I. Katkov, D. Khalatyan, Arman, K. Kinemuchi, S. Kisku, J. H. Knapen, J.-P. Kneib, J. A. Kollmeier, M. Kong, M. Kounkel, K. Kreckel, D. Krishnarao, I. Lacerna, R. R. Lane, R. Langgins, R. Lavender, D. R. Law, D. Lazarz, H. W. Leung, H.-H. Leung, H. M. Lewis, C. Li, R. Li, J. Lian, F.-H. Liang, L. Lin, Y.-T. Lin, S. Lin, C. Lintott, D. Long, P. Longa-Peña, C. López-Cobá, S. Lu, B. F. Lundgren, Y. Luo, J. T. Mackereth, A. de la Macorra, S. Mahadevan, S. R. Majewski, A. Manchado, T. Mandeville, C. Maraston, B. Margalef-Bentabol, T. Masseron, K. L. Masters, S. Mathur, R. M. McDermid, M. McKay, A. Merloni, M. Merrifield, S. Meszaros, A. Miglio, F. Di Mille, D. Minniti, R. Minsley, A. Monachesi, J. Moon, B. Mosser, J. Mulchaey, D. Muna, R. R. Muñoz, A. D. Myers, N. Myers, S. Nadathur, P. Nair, K. Nandra, J. Neumann, J. A. Newman, D. L. Nidever, F. Nikakhtar, C. Nitschelm, J. E. O'Connell, L. Garma-Oehmichen, G. Luan Souza de Oliveira, R. Olney, D. Oravetz, M. Ortigoza-Urdaneta, Y. Osorio, J. Otter, Z. J. Pace, N. Padilla, K. Pan, H.-A. Pan, T. Parikh, J. Parker, S. Peirani, K. Peña Ramírez, S. Penny, W. J. Percival, I. Perez-Fournon, M. Pinsonneault,

- F. Poidevin, V. J. Poovelil, A. M. Price-Whelan, A. Bárbara de Andrade Queiroz, M. J. Raddick, A. Ray, S. B. Rembold, N. Riddle, R. A. Riffel, R. Riffel, H.-W. Rix, A. C. Robin, A. Rodríguez-Puebla, A. Roman-Lopes, C. Román-Zúñiga, B. Rose, A. J. Ross, G. Rossi, K. H. R. Rubin, M. Salvato, S. F. Sánchez, J. R. Sánchez-Gallego, R. Sanderson, F. A. Santana Rojas, E. Sarceno, R. Sarmiento, C. Sayres, E. Sazonova, A. L. Schaefer, R. Schiavon, D. J. Schlegel, D. P. Schneider, M. Schultheis, A. Schwobe, A. Serenelli, J. Serna, Z. Shao, G. Shapiro, A. Sharma, Y. Shen, M. Shetrone, Y. Shu, J. D. Simon, M. F. Skrutskie, R. Smethurst, V. Smith, J. Sobeck, T. Spoo, D. Sprague, D. V. Stark, K. G. Stassun, M. Steinmetz, D. Stello, A. Stone-Martinez, T. Storchi-Bergmann, G. S. Stringfellow, A. Stutz, Y.-C. Su, M. Taghizadeh-Popp, M. S. Talbot, J. Tayar, E. Telles, J. Teske, A. Thakar, C. Theissen, A. Tkachenko, D. Thomas, R. Tojeiro, H. Hernandez Toledo, N. W. Troup, J. R. Trump, J. Trussler, J. Turner, S. Tuttle, E. Unda-Sanzana, J. A. Vázquez-Mata, M. Valentini, O. Valenzuela, J. Vargas-González, M. Vargas-Magaña, P. V. Alfaro, S. Villanova, F. Vincenzo, D. Wake, J. T. Warfield, J. D. Washington, B. A. Weaver, A.-M. Weijmans, D. H. Weinberg, A. Weiss, K. B. Westfall, V. Wild, M. C. Wilde, J. C. Wilson, R. F. Wilson, M. Wilson, J. Wolf, W. M. Wood-Vasey, R. Yan, O. Zamora, G. Zasowski, K. Zhang, C. Zhao, Z. Zheng, Z. Zheng, and K. Zhu. The Seventeenth Data Release of the Sloan Digital Sky Surveys: Complete Release of MaNGA, MaStar, and APOGEE-2 Data. *ApJS*, 259(2):35, Apr. 2022.
- [2] I. K. Baldry, M. L. Balogh, R. G. Bower, K. Glazebrook, R. C. Nichol, S. P. Bamford, and T. Budavari. Galaxy bimodality versus stellar mass and environment. *MNRAS*, 373(2):469–483, Dec. 2006.
 - [3] I. K. Baldry, K. Glazebrook, J. Brinkmann, Ž. Ivezić, R. H. Lupton, R. C. Nichol, and A. S. Szalay. Quantifying the Bimodal Color-Magnitude Distribution of Galaxies. *ApJ*, 600(2):681–694, Jan. 2004.
 - [4] J. A. Baldwin, M. M. Phillips, and R. Terlevich. Classification parameters for the emission-line spectra of extragalactic objects. *PASP*, 93:5–19, Feb. 1981.
 - [5] M. L. Balogh, I. K. Baldry, R. Nichol, C. Miller, R. Bower, and K. Glazebrook. The Bimodal Galaxy Color Distribution: Dependence on Luminosity and Environment. *ApJ*, 615(2):L101–L104, Nov. 2004.
 - [6] J. E. Barnes and L. Hernquist. Dynamics of interacting galaxies. *ARA&A*, 30:705–742, Jan. 1992.
 - [7] M. C. Begelman, M. Volonteri, and M. J. Rees. Formation of supermassive black holes by direct collapse in pre-galactic haloes. *MNRAS*, 370(1):289–298, July 2006.
 - [8] F. Belfiore, R. Maiolino, K. Bundy, K. Masters, M. Bershadsky, G. A. Oyarzún, L. Lin, M. Cano-Diaz, D. Wake, A. Spindler, D. Thomas, J. R. Brownstein, N. Drory, and R. Yan. SDSS IV MaNGA - sSFR profiles and the slow quenching of discs in green valley galaxies. *MNRAS*, 477(3):3014–3029, July 2018.

- [9] F. Belfiore, R. Maiolino, C. Maraston, E. Emsellem, M. A. Bershadsky, K. L. Masters, R. Yan, D. Bizyaev, M. Boquien, J. R. Brownstein, K. Bundy, N. Drory, T. M. Heckman, D. R. Law, A. Roman-Lopes, K. Pan, L. Stanghellini, D. Thomas, A.-M. Weijmans, and K. B. Westfall. SDSS IV MaNGA - spatially resolved diagnostic diagrams: a proof that many galaxies are LIERs. *MNRAS*, 461(3):3111–3134, Sept. 2016.
- [10] F. Belfiore, K. B. Westfall, A. Schaefer, M. Cappellari, X. Ji, M. A. Bershadsky, C. Tremonti, D. R. Law, R. Yan, K. Bundy, S. Shetty, N. Drory, D. Thomas, E. Emsellem, and S. F. Sánchez. The Data Analysis Pipeline for the SDSS-IV MaNGA IFU Galaxy Survey: Emission-line Modeling. *AJ*, 158(4):160, Oct. 2019.
- [11] E. F. Bell, D. H. McIntosh, N. Katz, and M. D. Weinberg. The Optical and Near-Infrared Properties of Galaxies. I. Luminosity and Stellar Mass Functions. *ApJS*, 149(2):289–312, Dec. 2003.
- [12] E. F. Bell, C. Wolf, K. Meisenheimer, H.-W. Rix, A. Borch, S. Dye, M. Kleinheinrich, L. Wisotzki, and D. H. McIntosh. Nearly 5000 Distant Early-Type Galaxies in COMBO-17: A Red Sequence and Its Evolution since $z \sim 1$. *ApJ*, 608(2):752–767, June 2004.
- [13] M. Blanton. NSA catalog, 2007.
- [14] M. R. Blanton, D. W. Hogg, N. A. Bahcall, I. K. Baldry, J. Brinkmann, I. Csabai, D. Eisenstein, M. Fukugita, J. E. Gunn, Ž. Ivezić, D. Q. Lamb, R. H. Lupton, J. Loveday, J. A. Munn, R. C. Nichol, S. Okamura, D. J. Schlegel, K. Shimasaku, M. A. Strauss, M. S. Vogeley, and D. H. Weinberg. The Broadband Optical Properties of Galaxies with Redshifts $0.02 < z < 0.22$. *ApJ*, 594(1):186–207, Sept. 2003.
- [15] M. R. Blanton, E. Kazin, D. Muna, B. A. Weaver, and A. Price-Whelan. Improved Background Subtraction for the Sloan Digital Sky Survey Images. *AJ*, 142(1):31, July 2011.
- [16] M. J. I. Brown, A. Dey, B. T. Jannuzi, K. Brand, A. J. Benson, M. Brodwin, D. J. Croton, and P. R. Eisenhardt. The Evolving Luminosity Function of Red Galaxies. *ApJ*, 654(2):858–877, Jan. 2007.
- [17] K. Bundy, M. A. Bershadsky, D. R. Law, R. Yan, N. Drory, N. MacDonald, D. A. Wake, B. Cherinka, J. R. Sánchez-Gallego, A.-M. Weijmans, D. Thomas, C. Tremonti, K. Masters, L. Coccato, A. M. Diamond-Stanic, A. Aragón-Salamanca, V. Avila-Reese, C. Badenes, J. Falcón-Barroso, F. Belfiore, D. Bizyaev, G. A. Blanc, J. Bland-Hawthorn, M. R. Blanton, J. R. Brownstein, N. Byler, M. Cappellari, C. Conroy, A. A. Dutton, E. Emsellem, J. Etherington, P. M. Frinchaboy, H. Fu, J. E. Gunn, P. Harding, E. J. Johnston, G. Kauffmann, K. Kinemuchi, M. A. Klaene, J. H. Knapen, A. Leauthaud, C. Li, L. Lin,

- R. Maiolino, V. Malanushenko, E. Malanushenko, S. Mao, C. Maraston, R. M. McDermid, M. R. Merrifield, R. C. Nichol, D. Oravetz, K. Pan, J. K. Parejko, S. F. Sanchez, D. Schlegel, A. Simmons, O. Steele, M. Steinmetz, K. Thanjavur, B. A. Thompson, J. L. Tinker, R. C. E. van den Bosch, K. B. Westfall, D. Wilkinson, S. Wright, T. Xiao, and K. Zhang. Overview of the SDSS-IV MaNGA Survey: Mapping nearby Galaxies at Apache Point Observatory. *ApJ*, 798:7, Jan. 2015.
- [18] M. Cappellari. Improving the full spectrum fitting method: accurate convolution with Gauss-Hermite functions. *MNRAS*, 466(1):798–811, Apr. 2017.
- [19] M. Cappellari and Y. Copin. Adaptive spatial binning of integral-field spectroscopic data using Voronoi tessellations. *MNRAS*, 342(2):345–354, June 2003.
- [20] M. Cappellari and E. Emsellem. Parametric Recovery of Line-of-Sight Velocity Distributions from Absorption-Line Spectra of Galaxies via Penalized Likelihood. *PASP*, 116(816):138–147, Feb. 2004.
- [21] S. Chandrasekhar. Dynamical Friction. I. General Considerations: the Coefficient of Dynamical Friction. *ApJ*, 97:255, Mar. 1943.
- [22] P. Chauke, A. van der Wel, C. Pacifici, R. Bezanson, P.-F. Wu, A. Gallazzi, C. Straatman, M. Franx, I. Barišić, E. F. Bell, J. van Houdt, M. V. Maseda, A. Muzzin, D. Sobral, and J. Spilker. Rejuvenation in $z \sim 0.8$ Quiescent Galaxies in LEGA-C. *ApJ*, 877(1):48, May 2019.
- [23] R. Cid Fernandes, G. Stasińska, A. Mateus, and N. Vale Asari. A comprehensive classification of galaxies in the Sloan Digital Sky Survey: how to tell true from fake AGN? *MNRAS*, 413(3):1687–1699, May 2011.
- [24] W. J. Couch and R. M. Sharples. A spectroscopic study of three rich galaxy clusters at $z=0.31$. *MNRAS*, 229:423–456, Dec. 1987.
- [25] K. S. Dawson, D. J. Schlegel, C. P. Ahn, S. F. Anderson, É. Aubourg, S. Bailey, R. H. Barkhouser, J. E. Bautista, A. Beifiori, A. A. Berlind, V. Bhardwaj, D. Bizyaev, C. H. Blake, M. R. Blanton, M. Blomqvist, A. S. Bolton, A. Borde, J. Bovy, W. N. Brandt, H. Brewington, J. Brinkmann, P. J. Brown, J. R. Brownstein, K. Bundy, N. G. Busca, W. Carithers, A. R. Carnero, M. A. Carr, Y. Chen, J. Comparat, N. Connolly, F. Cope, R. A. C. Croft, A. J. Cuesta, L. N. da Costa, J. R. A. Davenport, T. Delubac, R. de Putter, S. Dhital, A. Ealet, G. L. Ebelke, D. J. Eisenstein, S. Escoffier, X. Fan, N. Filiz Ak, H. Finley, A. Font-Ribera, R. Génova-Santos, J. E. Gunn, H. Guo, D. Haggard, P. B. Hall, J.-C. Hamilton, B. Harris, D. W. Harris, S. Ho, D. W. Hogg, D. Holder, K. Honscheid, J. Huehnerhoff, B. Jordan, W. P. Jordan, G. Kauffmann, E. A. Kazin, D. Kirkby, M. A. Klaene, J.-P. Kneib, J.-M. Le Goff, K.-G. Lee, D. C. Long, C. P. Loomis, B. Lundgren, R. H. Lupton, M. A. G. Maia, M. Makler, E. Malanushenko, V. Malanushenko, R. Mandelbaum, M. Manera, C. Maraston, D. Margala, K. L. Masters, C. K. McBride, P. McDonald, I. D. McGreer,

- R. G. McMahon, O. Mena, J. Miralda-Escudé, A. D. Montero-Dorta, F. Montesano, D. Muna, A. D. Myers, T. Naugle, R. C. Nichol, P. Noterdaeme, S. E. Nuza, M. D. Olmstead, A. Oravetz, D. J. Oravetz, R. Owen, N. Padmanabhan, N. Palanque-Delabrouille, K. Pan, J. K. Parejko, I. Pâris, W. J. Percival, I. Pérez-Fournon, I. Pérez-Ràfols, P. Petitjean, R. Pfaffenberger, J. Pforr, M. M. Pieri, F. Prada, A. M. Price-Whelan, M. J. Raddick, R. Rebolo, J. Rich, G. T. Richards, C. M. Rockosi, N. A. Roe, A. J. Ross, N. P. Ross, G. Rossi, J. A. Rubiño-Martin, L. Samushia, A. G. Sánchez, C. Sayres, S. J. Schmidt, D. P. Schneider, C. G. Scóccola, H.-J. Seo, A. Shelden, E. Sheldon, Y. Shen, Y. Shu, A. Slosar, S. A. Smee, S. A. Snedden, F. Stauffer, O. Steele, M. A. Strauss, A. Streblyanska, N. Suzuki, M. E. C. Swanson, T. Tal, M. Tanaka, D. Thomas, J. L. Tinker, R. Tojeiro, C. A. Tremonti, M. Vargas Magaña, L. Verde, M. Viel, D. A. Wake, M. Watson, B. A. Weaver, D. H. Weinberg, B. J. Weiner, A. A. West, M. White, W. M. Wood-Vasey, C. Yèche, I. Zehavi, G.-B. Zhao, and Z. Zheng. The Baryon Oscillation Spectroscopic Survey of SDSS-III. *AJ*, 145(1):10, Jan. 2013.
- [26] S. P. Driver, P. D. Allen, A. W. Graham, E. Cameron, J. Liske, S. C. Ellis, N. J. G. Cross, R. De Propris, S. Phillipps, and W. J. Couch. The Millennium Galaxy Catalogue: morphological classification and bimodality in the colour-concentration plane. *MNRAS*, 368(1):414–434, May 2006.
- [27] N. Drory, N. MacDonald, M. A. Bershad, K. Bundy, J. Gunn, D. R. Law, M. Smith, R. Stoll, C. A. Tremonti, D. A. Wake, R. Yan, A. M. Weijmans, N. Byler, B. Cherinka, F. Cope, A. Eigenbrot, P. Harding, D. Holder, J. Huehnert, K. Jaehnig, T. C. Jansen, M. Klaene, A. M. Paat, J. Percival, and C. Sayres. The MaNGA Integral Field Unit Fiber Feed System for the Sloan 2.5 m Telescope. *AJ*, 149(2):77, Feb. 2015.
- [28] S. L. Ellison, S. F. Sánchez, H. Ibarra-Medel, B. Antonio, J. T. Mendel, and J. Barrera-Ballesteros. Star formation is boosted (and quenched) from the inside-out: radial star formation profiles from MaNGA. *MNRAS*, 474(2):2039–2054, Feb. 2018.
- [29] Event Horizon Telescope Collaboration, K. Akiyama, A. Alberdi, W. Alef, K. Asada, R. Azulay, A.-K. Baczko, D. Ball, M. Baloković, J. Barrett, D. Bintley, L. Blackburn, W. Boland, K. L. Bouman, G. C. Bower, M. Bremer, C. D. Brinkerink, R. Brissenden, S. Britzen, A. E. Broderick, D. Brogiere, T. Bronzwaer, D.-Y. Byun, J. E. Carlstrom, A. Chael, C.-k. Chan, S. Chatterjee, K. Chatterjee, M.-T. Chen, Y. Chen, I. Cho, P. Christian, J. E. Conway, J. M. Cordes, G. B. Crew, Y. Cui, J. Davelaar, M. De Laurentis, R. Deane, J. Dempsey, G. Desvignes, J. Dexter, S. S. Doleman, R. P. Eatough, H. Falcke, V. L. Fish, E. Fomalont, R. Fraga-Encinas, W. T. Freeman, P. Friberg, C. M. Fromm, J. L. Gómez, P. Galison, C. F. Gammie, R. García, O. Gentaz, B. Georgiev, C. Goddi, R. Gold, M. Gu, M. Gurwell, K. Hada, M. H. Hecht, R. Hesper, L. C. Ho, P. Ho, M. Honma, C.-W. L. Huang, L. Huang, D. H.

Hughes, S. Ikeda, M. Inoue, S. Issaoun, D. J. James, B. T. Jannuzzi, M. Janssen, B. Jeter, W. Jiang, M. D. Johnson, S. Jorstad, T. Jung, M. Karami, R. Karuppusamy, T. Kawashima, G. K. Keating, M. Kettenis, J.-Y. Kim, J. Kim, J. Kim, M. Kino, J. Y. Koay, P. M. Koch, S. Koyama, M. Kramer, C. Kramer, T. P. Krichbaum, C.-Y. Kuo, T. R. Lauer, S.-S. Lee, Y.-R. Li, Z. Li, M. Lindqvist, K. Liu, E. Liuzzo, W.-P. Lo, A. P. Lobanov, L. Loinard, C. Lonsdale, R.-S. Lu, N. R. MacDonald, J. Mao, S. Markoff, D. P. Marrone, A. P. Marscher, I. Martí-Vidal, S. Matsushita, L. D. Matthews, L. Medeiros, K. M. Menten, Y. Mizuno, I. Mizuno, J. M. Moran, K. Moriyama, M. Moscibrodzka, C. Müller, H. Nagai, N. M. Nagar, M. Nakamura, R. Narayan, G. Narayanan, I. Natarajan, R. Neri, C. Ni, A. Noutsos, H. Okino, H. Olivares, G. N. Ortiz-León, T. Oyama, F. Özel, D. C. M. Palumbo, N. Patel, U.-L. Pen, D. W. Pesce, V. Piétu, R. Plambeck, A. PopStefanija, O. Porth, B. Prather, J. A. Preciado-López, D. Psaltis, H.-Y. Pu, V. Ramakrishnan, R. Rao, M. G. Rawlings, A. W. Raymond, L. Rizzolla, B. Ripperda, F. Roelofs, A. Rogers, E. Ros, M. Rose, A. Roshanineshat, H. Rottmann, A. L. Roy, C. Ruszczyk, B. R. Ryan, K. L. J. Rygl, S. Sánchez, D. Sánchez-Arguelles, M. Sasada, T. Savolainen, F. P. Schloerb, K.-F. Schuster, L. Shao, Z. Shen, D. Small, B. W. Sohn, J. SooHoo, F. Tazaki, P. Tiede, R. P. J. Tilanus, M. Titus, K. Toma, P. Torne, T. Trent, S. Trippe, S. Tsuda, I. van Bemmell, H. J. van Langevelde, D. R. van Rossum, J. Wagner, J. Wardle, J. Weintraub, N. Wex, R. Wharton, M. Wielgus, G. N. Wong, Q. Wu, K. Young, A. Young, Z. Younsi, F. Yuan, Y.-F. Yuan, J. A. Zensus, G. Zhao, S.-S. Zhao, Z. Zhu, J.-C. Algaba, A. Allardi, R. Amestica, J. Anczarski, U. Bach, F. K. Baganoff, C. Beaudoin, B. A. Benson, R. Berthold, J. M. Blanchard, R. Blundell, S. Bustamente, R. Cappallo, E. Castillo-Domínguez, C.-C. Chang, S.-H. Chang, S.-C. Chang, C.-C. Chen, R. Chilson, T. C. Chuter, R. Córdova Rosado, I. M. Coulson, T. M. Crawford, J. Crowley, J. David, M. Derome, M. Dexter, S. Dornbusch, K. A. Dudevoir, S. A. Dzib, A. Eckart, C. Eckert, N. R. Erickson, W. B. Everett, A. Faber, J. R. Farah, V. Fath, T. W. Folkers, D. C. Forbes, R. Freund, A. I. Gómez-Ruiz, D. M. Gale, F. Gao, G. Geertsema, D. A. Graham, C. H. Greer, R. Grosslein, F. Gueth, D. Haggard, N. W. Halverson, C.-C. Han, K.-C. Han, J. Hao, Y. Hasegawa, J. W. Henning, A. Hernández-Gómez, R. Herrero-Illana, S. Heyminck, A. Hirota, J. Hoge, Y.-D. Huang, C. M. V. Impellizzeri, H. Jiang, A. Kamble, R. Keisler, K. Kimura, Y. Kono, D. Kubo, J. Kuroda, R. Lacasse, R. A. Laing, E. M. Leitch, C.-T. Li, L. C. C. Lin, C.-T. Liu, K.-Y. Liu, L.-M. Lu, R. G. Marson, P. L. Martin-Cocher, K. D. Massingill, C. Matulonis, M. P. McColl, S. R. McWhirter, H. Messias, Z. Meyer-Zhao, D. Michalik, A. Montaña, W. Montgomerie, M. Mora-Klein, D. Muders, A. Nadolski, S. Navarro, J. Neilsen, C. H. Nguyen, H. Nishioka, T. Norton, M. A. Nowak, G. Nystrom, H. Ogawa, P. Oshiro, T. Oyama, H. Parsons, S. N. Paine, J. Peñalver, N. M. Phillips, M. Poirier, N. Pradel, R. A. Primiani, P. A. Raffin, A. S. Rahlin, G. Reiland, C. Risacher, I. Ruiz, A. F. Sáez-Madaín, R. Sassella, P. Schellart, P. Shaw, K. M. Silva, H. Shiokawa, D. R. Smith, W. Snow, K. Soucar, D. Sousa, T. K. Sridharan, R. Srinivasan, W. Stahm, A. A. Stark, K. Story, S. T. Timmer, L. Vertatschitsch, C. Walther, T.-S. Wei, N. Whitehorn, A. R.

- Whitney, D. P. Woody, J. G. A. Wouterloot, M. Wright, P. Yamaguchi, C.-Y. Yu, M. Zeballos, S. Zhang, and L. Ziurys. First M87 Event Horizon Telescope Results. I. The Shadow of the Supermassive Black Hole. *ApJ*, 875(1):L1, Apr. 2019.
- [30] S. M. Faber, C. N. A. Willmer, C. Wolf, D. C. Koo, B. J. Weiner, J. A. Newman, M. Im, A. L. Coil, C. Conroy, M. C. Cooper, M. Davis, D. P. Finkbeiner, B. F. Gerke, K. Gebhardt, E. J. Groth, P. Guhathakurta, J. Harker, N. Kaiser, S. Kassin, M. Kleinheinrich, N. P. Konidakis, R. G. Kron, L. Lin, G. Luppino, D. S. Madgwick, K. Meisenheimer, K. G. Noeske, A. C. Phillips, V. L. Sarajedini, R. P. Schiavon, L. Simard, A. S. Szalay, N. P. Vogt, and R. Yan. Galaxy Luminosity Functions to $z \sim 1$ from DEEP2 and COMBO-17: Implications for Red Galaxy Formation. *ApJ*, 665(1):265–294, Aug. 2007.
- [31] J. J. Fang, S. M. Faber, S. Salim, G. J. Graves, and R. M. Rich. The Slow Death (Or Rebirth?) of Extended Star Formation in $z \sim 0.1$ Green Valley Early-type Galaxies. *ApJ*, 761(1):23, Dec. 2012.
- [32] R. A. Finn, M. L. Balogh, D. Zaritsky, C. J. Miller, and R. C. Nichol. Mass and Redshift Dependence of Star Formation in Relaxed Galaxy Clusters. *ApJ*, 679(1):279–292, May 2008.
- [33] A. M. Ghez, B. L. Klein, M. Morris, and E. E. Becklin. High Proper-Motion Stars in the Vicinity of Sagittarius A*: Evidence for a Supermassive Black Hole at the Center of Our Galaxy. *ApJ*, 509(2):678–686, Dec. 1998.
- [34] J. E. Gunn and I. Gott, J. Richard. On the Infall of Matter Into Clusters of Galaxies and Some Effects on Their Evolution. *ApJ*, 176:1, Aug. 1972.
- [35] J. E. Gunn, W. A. Siegmund, E. J. Mannery, R. E. Owen, C. L. Hull, R. F. Leger, L. N. Carey, G. R. Knapp, D. G. York, W. N. Boroski, S. M. Kent, R. H. Lupton, C. M. Rockosi, M. L. Evans, P. Waddell, J. E. Anderson, J. Annis, J. C. Barentine, L. M. Bartoszek, S. Bastian, S. B. Bracker, H. J. Brewington, C. I. Briegel, J. Brinkmann, Y. J. Brown, M. A. Carr, P. C. Czarapata, C. C. Drennan, T. Dombeck, G. R. Federwitz, B. A. Gillespie, C. Gonzales, S. U. Hansen, M. Harvanek, J. Hayes, W. Jordan, E. Kinney, M. Klaene, S. J. Kleinman, R. G. Kron, J. Kresinski, G. Lee, S. Limmongkol, C. W. Lindenmeyer, D. C. Long, C. L. Loomis, P. M. McGehee, P. M. Mantsch, J. Neilsen, Eric H., R. M. Neswold, P. R. Newman, A. Nitta, J. Peoples, John, J. R. Pier, P. S. Prieto, A. Prosapio, C. Rivetta, D. P. Schneider, S. Snedden, and S.-i. Wang. The 2.5 m Telescope of the Sloan Digital Sky Survey. *AJ*, 131(4):2332–2359, Apr. 2006.
- [36] T. M. Heckman and P. N. Best. The Coevolution of Galaxies and Supermassive Black Holes: Insights from Surveys of the Contemporary Universe. *ARA&A*, 52:589–660, Aug. 2014.

- [37] D. W. Hogg, M. R. Blanton, D. J. Eisenstein, J. E. Gunn, D. J. Schlegel, I. Zehavi, N. A. Bahcall, J. Brinkmann, I. Csabai, D. P. Schneider, D. H. Weinberg, and D. G. York. The Overdensities of Galaxy Environments as a Function of Luminosity and Color. *ApJ*, 585(1):L5–L9, Mar. 2003.
- [38] P. F. Hopkins, L. Hernquist, T. J. Cox, T. Di Matteo, B. Robertson, and V. Springel. A Unified, Merger-driven Model of the Origin of Starbursts, Quasars, the Cosmic X-Ray Background, Supermassive Black Holes, and Galaxy Spheroids. *ApJS*, 163(1):1–49, Mar. 2006.
- [39] E. P. Hubble. Extragalactic nebulae. *ApJ*, 64:321–369, Dec. 1926.
- [40] E. P. Hubble. *Realm of the Nebulae*. 1936.
- [41] X. Ji and R. Yan. Constraining photoionization models with a reprojected optical diagnostic diagram. *MNRAS*, 499(4):5749–5764, Oct. 2020.
- [42] G. Kauffmann, T. M. Heckman, S. D. M. White, S. Charlot, C. Tremonti, E. W. Peng, M. Seibert, J. Brinkmann, R. C. Nichol, M. SubbaRao, and D. York. The dependence of star formation history and internal structure on stellar mass for 10^5 low-redshift galaxies. *MNRAS*, 341(1):54–69, May 2003.
- [43] J. Kennicutt, Robert C. Star Formation in Galaxies Along the Hubble Sequence. *ARA&A*, 36:189–232, Jan. 1998.
- [44] J. Kormendy and J. Kennicutt, Robert C. Secular Evolution and the Formation of Pseudobulges in Disk Galaxies. *ARA&A*, 42(1):603–683, Sept. 2004.
- [45] J. Kormendy and D. Richstone. Inward Bound—The Search For Supermassive Black Holes In Galactic Nuclei. *ARA&A*, 33:581, Jan. 1995.
- [46] A. Kulier, J. P. Ostriker, P. Natarajan, C. N. Lackner, and R. Cen. Understanding Black Hole Mass Assembly via Accretion and Mergers at Late Times in Cosmological Simulations. *ApJ*, 799(2):178, Feb. 2015.
- [47] D. R. Law, B. Cherinka, and MaNGA Team. SDSS-IV MaNGA: Data Products, Quality, and Initial Public Release. In *American Astronomical Society Meeting Abstracts #227*, volume 227 of *American Astronomical Society Meeting Abstracts*, page 312.13, Jan. 2016.
- [48] D. R. Law, R. Yan, M. A. Bershadsky, K. Bundy, B. Cherinka, N. Drory, N. Macdonald, J. R. Sánchez-Gallego, D. A. Wake, A.-M. Weijmans, M. R. Blanton, M. A. Klaene, S. M. Moran, S. F. Sanchez, and K. Zhang. Observing Strategy for the SDSS-IV/MaNGA IFU Galaxy Survey. *AJ*, 150(1):19, July 2015.
- [49] J. Lian, R. Yan, M. Blanton, and X. Kong. Inside-out growth or inside-out quenching? Clues from colour gradients of local galaxies. *MNRAS*, 472(4):4679–4688, Dec. 2017.

- [50] D. Lynden-Bell. Galactic Nuclei as Collapsed Old Quasars. *Nature*, 223(5207):690–694, Aug. 1969.
- [51] M. Martig, F. Bournaud, R. Teyssier, and A. Dekel. Morphological Quenching of Star Formation: Making Early-Type Galaxies Red. *ApJ*, 707(1):250–267, Dec. 2009.
- [52] R. Minkowski and G. O. Abell. The Galactic Distribution of Planetary Nebulae. *PASP*, 75(447):488, Dec. 1963.
- [53] U. of Iowa. Hubble’s tuning fork, 2023.
- [54] F. Pacucci and A. Loeb. Separating Accretion and Mergers in the Cosmic Growth of Black Holes with X-Ray and Gravitational-wave Observations. *ApJ*, 895(2):95, June 2020.
- [55] Y. Peng, R. Maiolino, and R. Cochrane. Strangulation as the primary mechanism for shutting down star formation in galaxies. *Nature*, 521(7551):192–195, May 2015.
- [56] V. Petrosian. Surface Brightness and Evolution of Galaxies. *ApJ*, 210:L53, Dec. 1976.
- [57] A. Saintonge, K.-V. H. Tran, and B. P. Holden. Spitzer/MIPS 24 μm Observations of Galaxy Clusters: An Increasing Fraction of Obscured Star-forming Members from $z = 0.02$ to $z = 0.83$. *ApJ*, 685(2):L113, Oct. 2008.
- [58] S. F. Sánchez, E. Pérez, P. Sánchez-Blázquez, J. J. González, F. F. Rosáles-Ortega, M. Cano-Díaz, C. López-Cobá, R. A. Marino, A. Gil de Paz, M. Mollá, A. R. López-Sánchez, Y. Ascasibar, and J. Barrera-Ballesteros. Pipe3D, a pipeline to analyze Integral Field Spectroscopy Data: I. New fitting philosophy of FIT3D. *Rev. Mex. Astron. Astrofis.*, 52:21–53, Apr. 2016.
- [59] P. Santini, A. Fontana, M. Castellano, M. Di Criscienzo, E. Merlin, R. Amorin, F. Cullen, E. Daddi, M. Dickinson, J. S. Dunlop, A. Grazian, A. Lamastra, R. J. McLure, M. J. Michałowski, L. Pentericci, and X. Shu. The Star Formation Main Sequence in the Hubble Space Telescope Frontier Fields. *ApJ*, 847(1):76, Sept. 2017.
- [60] M. Sarzi, J. C. Shields, K. Schawinski, H. Jeong, K. Shapiro, R. Bacon, M. Bureau, M. Cappellari, R. L. Davies, P. T. de Zeeuw, E. Emsellem, J. Falcón-Barroso, D. Krajnović, H. Kuntschner, R. M. McDermid, R. F. Peletier, R. C. E. van den Bosch, G. van de Ven, and S. K. Yi. The SAURON project - XVI. On the sources of ionization for the gas in elliptical and lenticular galaxies. *MNRAS*, 402(4):2187–2210, Mar. 2010.
- [61] K. Schawinski, S. Kaviraj, S. Khochfar, S. J. Yoon, S. K. Yi, J. M. Deharveng, A. Boselli, T. Barlow, T. Conrow, K. Forster, P. G. Friedman, D. C. Martin, P. Morrissey, S. Neff, D. Schiminovich, M. Seibert, T. Small, T. Wyder,

- L. Bianchi, J. Donas, T. Heckman, Y. W. Lee, B. Madore, B. Milliard, R. M. Rich, and A. Szalay. The Effect of Environment on the Ultraviolet Color-Magnitude Relation of Early-Type Galaxies. *ApJS*, 173(2):512–523, Dec. 2007.
- [62] K. Schawinski, C. M. Urry, B. D. Simmons, L. Fortson, S. Kaviraj, W. C. Keel, C. J. Lintott, K. L. Masters, R. C. Nichol, M. Sarzi, R. Skibba, E. Treister, K. W. Willett, O. I. Wong, and S. K. Yi. The green valley is a red herring: Galaxy Zoo reveals two evolutionary pathways towards quenching of star formation in early- and late-type galaxies. *MNRAS*, 440(1):889–907, May 2014.
- [63] K. Schawinski, C. M. Urry, S. Virani, P. Coppi, S. P. Bamford, E. Treister, C. J. Lintott, M. Sarzi, W. C. Keel, S. Kaviraj, C. N. Cardamone, K. L. Masters, N. P. Ross, D. Andreescu, P. Murray, R. C. Nichol, M. J. Raddick, A. Slosar, A. S. Szalay, D. Thomas, and J. Vandenberg. Galaxy Zoo: The Fundamentally Different Co-Evolution of Supermassive Black Holes and Their Early- and Late-Type Host Galaxies. *ApJ*, 711(1):284–302, Mar. 2010.
- [64] G. A. Shields. A Brief History of Active Galactic Nuclei. *PASP*, 111(760):661–678, June 1999.
- [65] R. Singh, G. van de Ven, K. Jahnke, M. Lyubenova, J. Falcón-Barroso, J. Alves, R. Cid Fernandes, L. Galbany, R. García-Benito, B. Husemann, R. C. Kennicutt, R. A. Marino, I. Márquez, J. Masegosa, D. Mast, A. Pasquali, S. F. Sánchez, J. Walcher, V. Wild, L. Wisotzki, and B. Ziegler. The nature of LINER galaxies: Ubiquitous hot old stars and rare accreting black holes. *A&A*, 558:A43, Oct. 2013.
- [66] V. Springel, T. Di Matteo, and L. Hernquist. Black Holes in Galaxy Mergers: The Formation of Red Elliptical Galaxies. *ApJ*, 620(2):L79–L82, Feb. 2005.
- [67] I. Strateva, Ž. Ivezić, G. R. Knapp, V. K. Narayanan, M. A. Strauss, J. E. Gunn, R. H. Lupton, D. Schlegel, N. A. Bahcall, J. Brinkmann, R. J. Brunner, T. Budavári, I. Csabai, F. J. Castander, M. Doi, M. Fukugita, Z. Györy, M. Hamabe, G. Hennessy, T. Ichikawa, P. Z. Kunszt, D. Q. Lamb, T. A. McKay, S. Okamura, J. Racusin, M. Sekiguchi, D. P. Schneider, K. Shimasaku, and D. York. Color Separation of Galaxy Types in the Sloan Digital Sky Survey Imaging Data. *AJ*, 122(4):1861–1874, Oct. 2001.
- [68] A. R. Tomczak, R. F. Quadri, K.-V. H. Tran, I. Labbé, C. M. S. Straatman, C. Papovich, K. Glazebrook, R. Allen, G. B. Brammer, M. Cowley, M. Dickinson, D. Elbaz, H. Inami, G. G. Kacprzak, G. E. Morrison, T. Nanayakkara, S. E. Persson, G. A. Rees, B. Salmon, C. Schreiber, L. R. Spitler, and K. E. Whitaker. The SFR- M^* Relation and Empirical Star-Formation Histories from ZFOURGE* at $0.5 < z < 4$. *ApJ*, 817(2):118, Feb. 2016.
- [69] D. A. Wake, K. Bundy, A. M. Diamond-Stanic, R. Yan, M. R. Blanton, M. A. Bershadsky, J. R. Sánchez-Gallego, N. Drory, A. Jones, G. Kauffmann, D. R. Law,

- C. Li, N. MacDonald, K. Masters, D. Thomas, J. Tinker, A.-M. Weijmans, and J. R. Brownstein. The SDSS-IV MaNGA Sample: Design, Optimization, and Usage Considerations. *AJ*, 154(3):86, Sept. 2017.
- [70] E. Wang, C. Li, T. Xiao, L. Lin, M. Bershadsky, D. R. Law, M. Merrifield, S. F. Sanchez, R. A. Riffel, R. Riffel, and R. Yan. SDSS-IV MaNGA: Star Formation Cessation in Low-redshift Galaxies. I. Dependence on Stellar Mass and Structural Properties. *ApJ*, 856(2):137, Apr. 2018.
- [71] K. B. Westfall, M. Cappellari, M. A. Bershadsky, K. Bundy, F. Belfiore, X. Ji, D. R. Law, A. Schaefer, S. Shetty, C. A. Tremonti, R. Yan, B. H. Andrews, J. R. Brownstein, B. Cherinka, L. Coccato, N. Drory, C. Maraston, T. Parikh, J. R. Sánchez-Gallego, D. Thomas, A.-M. Weijmans, J. Barrera-Ballesteros, C. Du, D. Goddard, N. Li, K. Masters, H. J. Ibarra Medel, S. F. Sánchez, M. Yang, Z. Zheng, and S. Zhou. The Data Analysis Pipeline for the SDSS-IV MaNGA IFU Galaxy Survey: Overview. *AJ*, 158(6):231, Dec. 2019.
- [72] R. Yan and M. R. Blanton. The Nature of LINER-like Emission in Red Galaxies. *ApJ*, 747(1):61, Mar. 2012.
- [73] R. Yan, K. Bundy, D. R. Law, M. A. Bershadsky, B. Andrews, B. Cherinka, A. M. Diamond-Stanic, N. Drory, N. MacDonald, J. R. Sánchez-Gallego, D. Thomas, D. A. Wake, A.-M. Weijmans, K. B. Westfall, K. Zhang, A. Aragón-Salamanca, F. Belfiore, D. Bizyaev, G. A. Blanc, M. R. Blanton, J. Brownstein, M. Cappellari, R. D’Souza, E. Emsellem, H. Fu, P. Gaulme, M. T. Graham, D. Goddard, J. E. Gunn, P. Harding, A. Jones, K. Kinemuchi, C. Li, H. Li, R. Maiolino, S. Mao, C. Maraston, K. Masters, M. R. Merrifield, D. Oravetz, K. Pan, J. K. Parejko, S. F. Sanchez, D. Schlegel, A. Simmons, K. Thanjavur, J. Tinker, C. Tremonti, R. van den Bosch, and Z. Zheng. SDSS-IV MaNGA IFS Galaxy Survey—Survey Design, Execution, and Initial Data Quality. *AJ*, 152(6):197, Dec 2016.
- [74] R. Yan, Y. Chen, D. Lazarz, D. Bizyaev, C. Maraston, G. S. Stringfellow, K. McCarthy, S. Meneses-Goytia, D. R. Law, D. Thomas, J. Falcon Barroso, J. R. Sánchez-Gallego, E. Schlafly, Z. Zheng, M. Argudo-Fernández, R. L. Beaton, T. C. Beers, M. Bershadsky, M. R. Blanton, J. Brownstein, K. Bundy, K. C. Chambers, B. Cherinka, N. De Lee, N. Drory, L. Galbany, J. Holtzman, J. Imig, N. Kaiser, K. Kinemuchi, C. Liu, A. L. Luo, E. Magnier, S. Majewski, P. Nair, A. Oravetz, D. Oravetz, K. Pan, J. Sobeck, K. Stassun, M. Talbot, C. Tremonti, C. Waters, A.-M. Weijmans, R. Wilhelm, G. Zasowski, G. Zhao, and Y.-H. Zhao. SDSS-IV MaStar: A Large and Comprehensive Empirical Stellar Spectral Library—First Release. *ApJ*, 883(2):175, Oct. 2019.
- [75] R. Yan, J. A. Newman, S. M. Faber, N. Konidaris, D. Koo, and M. Davis. On the Origin of [O II] Emission in Red-Sequence and Poststarburst Galaxies. *ApJ*, 648(1):281–298, Sept. 2006.

- [76] D. G. York, J. Adelman, J. Anderson, John E., S. F. Anderson, J. Annis, N. A. Bahcall, J. A. Bakken, R. Barkhouser, S. Bastian, E. Berman, W. N. Boroski, S. Bracker, C. Briegel, J. W. Briggs, J. Brinkmann, R. Brunner, S. Burles, L. Carey, M. A. Carr, F. J. Castander, B. Chen, P. L. Colestock, A. J. Connolly, J. H. Crocker, I. Csabai, P. C. Czarapata, J. E. Davis, M. Doi, T. Dombeck, D. Eisenstein, N. Ellman, B. R. Elms, M. L. Evans, X. Fan, G. R. Federwitz, L. Fiscelli, S. Friedman, J. A. Frieman, M. Fukugita, B. Gillespie, J. E. Gunn, V. K. Gurbani, E. de Haas, M. Haldeman, F. H. Harris, J. Hayes, T. M. Heckman, G. S. Hennessy, R. B. Hindsley, S. Holm, D. J. Holmgren, C.-h. Huang, C. Hull, D. Husby, S.-I. Ichikawa, T. Ichikawa, Ž. Ivezić, S. Kent, R. S. J. Kim, E. Kinney, M. Klaene, A. N. Kleinman, S. Kleinman, G. R. Knapp, J. Korienek, R. G. Kron, P. Z. Kunszt, D. Q. Lamb, B. Lee, R. F. Leger, S. Limmongkol, C. Lindenmeyer, D. C. Long, C. Loomis, J. Loveday, R. Lucinio, R. H. Lupton, B. MacKinnon, E. J. Mannery, P. M. Mantsch, B. Margon, P. McGehee, T. A. McKay, A. Meiksin, A. Merelli, D. G. Monet, J. A. Munn, V. K. Narayanan, T. Nash, E. Neilsen, R. Neswold, H. J. Newberg, R. C. Nichol, T. Nicinski, M. Nonino, N. Okada, S. Okamura, J. P. Ostriker, R. Owen, A. G. Pauls, J. Peoples, R. L. Peterson, D. Petravick, J. R. Pier, A. Pope, R. Pordes, A. Prosapio, R. Rechenmacher, T. R. Quinn, G. T. Richards, M. W. Richmond, C. H. Rivetta, C. M. Rockosi, K. Ruthmansdorfer, D. Sandford, D. J. Schlegel, D. P. Schneider, M. Sekiguchi, G. Sergey, K. Shimasaku, W. A. Siegmund, S. Smee, J. A. Smith, S. Snedden, R. Stone, C. Stoughton, M. A. Strauss, C. Stubbs, M. SubbaRao, A. S. Szalay, I. Szapudi, G. P. Szokoly, A. R. Thakar, C. Tremonti, D. L. Tucker, A. Uomoto, D. Vanden Berk, M. S. Vogeley, P. Waddell, S.-i. Wang, M. Watanabe, D. H. Weinberg, B. Yanny, N. Yasuda, and SDSS Collaboration. The Sloan Digital Sky Survey: Technical Summary. *AJ*, 120(3):1579–1587, Sept. 2000.

Vita

Chenyu Zhao

Place of Birth:

- Tianjin, China

Education:

- University of Kentucky, Lexington, Kentucky
M.S. in Physics, December 2019
- University of Science and Technology of China, Hefei, Anhui, China
B.S. in Astronomy, July 2017

Professional Positions:

- Graduate Teaching Assistant, University of Kentucky Fall 2017–Spring 2023